Cronfa
Swansea University's Research Repository

Range uncertainty and dose uniformity in proton therapy in the presence of inhomogeneities in tissue and phantom materials.

Prifysgol Abertawe
Swansea University

Sumaira Nazir

School of Medicine

Swansea University

This thesis is submitted in fulfillment of the requirements for the degree of

Doctor of Philosophy

January 7, 2022

Copyright: The author, Sumaira Nazir, 2022.

Abstract

Proton therapy is an emerging modality for providing radiation treatment to cancer patients. The principal advantages of proton therapy are the reduced total dose deposited into the patient as compared to conventional photon therapy and the finite range of the proton beam. It is considered as a more favorable option for optimum treatment outcomes in terms of maximising tumor control probability and minimising normal tissue complications. The depth dose distribution of the proton beam adds an additional degree of freedom to treatment planning. The range in tissue is associated with substantial uncertainties triggered by imaging, patient set-up, beam delivery and dose calculations. Therefore, reduction in uncertainties would allow to minimise the treatment volume and thus allow a better usage of the protons. However, the presence of sub-millimeter sized heterogeneities, such is pronounced in trabecular bone and lung parenchyma, in the path of the proton beam can cause the Bragg peak degradation with a widening to the distal fall-off. Additionally, the restricted resolution of a classic CT scan used in treatment planning cannot fully resolve such fine structures, potentially leading to inaccuracy in determination of the range.

This work aims to investigate the presence of range uncertainties in proton therapy beams when they penetrate through the sub-millimeter sized heterogeneities. The effect of Bragg peak degradation has been demonstrated in bone models with the FLUKA Monte Carlo code and experimental measurements with a 36 MeV proton beam. The bone-substitute material, SAWBONES®, ranging in density from 0.088 to 0.48 g/cc, was used to simulate bone heterogeneities. Micro-CT images were obtained of the SAWBONES® material and used to construct Monte Carlo models of realistic proton radiotherapy treatments and to benchmark experimental studies. Broadening of the Bragg peak and shifts in the range, as defined by the d20% depth-dose parameter were observed both experimentally and in

Monte Carlo models, indicating that such effects are in principle, clinically relevant in certain circumstances.

Furthermore, a FLUKA Monte Carlo model is benchmarked against the Eclipse treatment planning system (TPS) golden data for proton beam therapy. This project is designed to obtain the proton dose distributions from TPS for a 10 $\times$10 $\times$ 10 cm^3 water-filled box. A Monte Carlo analytical model is developed by utilising the information from the TPS to recalculate the dose distribution which are then compared to find any differences (if present) for different phantom materials. Due to the lack of any experimental information to measure the normalized depth dose as a function of energy, considering the general behaviour of a monitor chamber, it has been assumed that the treatment planning system has a built-in relationship between the monitor units (MU) and dose delivered. A mathematical formula is developed to find the relationship between monitor units (MU) and dose (E).

$$MU \; \alpha \; 1/E^{\mathrm{a}}. \tag{1}$$

The value of a is varied from 0 to 1. It has been observed that the beam non-uniformity calculated by using the relationship " MU = $E^{-0.5}$ " is only 0.15 % for water and 0.43 % for graphite. This non-uniformity in graphite is not severe and it is actually clinically acceptable. This modeling has suggested that the planned dose distributions for water can also be replaced by graphite to a reasonably acceptable standard.

Declaration

I hereby declare that except where specific reference is made to the work of others, the contents of this thesis are original and have not been submitted in whole or in part for consideration for any other degree or qualification in this, or any other university. This thesis is my own work and contains nothing which is the outcome of work done in collaboration with others, except as specified in the text and Acknowledgements. I give consent for the thesis, if accepted, to be available for photocopying and for inter-library loans, and for the title and summary/abstract to be made available to outside organisations.

Sumaira Nazir

07.01.2022

Acknowledgements

Foremost, I would like to express my sincere gratitude to my supervisor **Dr Richard Hugtenburg** for the continuous support of my PhD study and research, providing excellent advice and support during difficult times, for his patience, motivation, enthusiasm and extensive knowledge. His guidance helped me in all the time of research and writing of this thesis. Without his support, this research would not have been possible.

Besides my supervisor, I would like to thank **Dr Tony Price** from Birmingham University. His massive support for performing this experiment at the proton beam of Birmingham University was really substantial.

I would also like to thank **Jordan Pritchard** and **Sarah Aldridge** from the Materials Science and Engineering department at Swansea University for providing the micro-CT scans of the foam samples, and **Jordan** for identifying and purchasing the phantom materials.

I would like to acknowledge the people who mean a lot to me, my parents, **Ammi Jaan** and **Abu Jaan** for showing faith in me and giving me liberty to choose what I desired. I salute you both for the selfless love, care, pain and sacrifices you did to shape my life.

Last but by no means least, I owe thanks to a very special person, my husband, **Shahid** for his continued and unfailing love, support and understanding during my pursuit of my PhD degree that made the completion of thesis possible. You were always around at times I thought that it is impossible to continue. I greatly value his contribution and hugely appreciate his belief in me. I appreciate my lovely kids, **Ifraheem**, **Maryum** and **Manha** for abiding my ignorance and the patience they showed during my thesis writing. I consider myself the luckiest person in the world to have such a lovely and caring family, standing beside me with their love and unconditional support.

Contents

List of Figures

List of Tables

Listings

Chapter 1

Introduction

1.1 Overview

Since Robert Wilson first suggested the use of protons for treatment in 1946, there has been an increased interest in the use of protons for cancer therapy. The unique depth-dose characteristics of protons offers a substantial clinical advantage over conventional X-ray photon therapy. The main benefit of using protons is that they have a finite penetration range in a particular medium and deposite most of their energy near the end of this range. For a monoenergetic proton beam travelling through homogeneous material the dose distribution is specified by a low entrance dose followed by the Bragg peak, with a dose fall-off along the distal edge. This typical dose profile has the advantage of delivering a much lower integral dose to the patient as compared to photon therapy. However, the presence of sub-millimeter sized density heterogeneities, such as trabecular bone, in the path of the proton beam can cause a potential shift to the sharp distal dose fall-off due to increased beam straggling. Further, the highest resolution of a classic CT scan used in treatment planning cannot fully determine such fine structures, potentially leads to a change in the range and dose to the tumor. Therefore, in order to take the full advantage, the range of proton beams in patients need to be predicted as precisely as possible in the treatment planning as well as the delivery process.

This thesis reprsents research into the measurement of the range uncertainties in proton therapy in the presence of sub-millimeter size inhomogeneities. Conventionally, it is a

common practice to treat the brain tumors through the flat skull bone, as there has not been reported any issue of range uncertainties for proton dose delivery through the thin part of the bone. This work demonstrates for the first time that there is no major problem for proton beam therapy in terms of scattering in the flat skull bone and supports the normal proton therapy practice for treating brain tumors through the thin flat bone. Successful results obtained for flat female skull bone motivate the need for a Monte Carlo benchmark to analyse the proton range uncertainties through the thick part of the bone. For that purpose, SAWBONES® plastic material (used in normal surgical practice) with different densities have been employed as a bone substitute to simulate the proton beams through a comparatively thick bone model, designed in FLUKA (a Monte Carlo code). Experimental validation of the effect of sub-CT inhomogeneities in bone substitute material, observed in Monte Carlo models, has been achieved, with experiments performed at the Birmingham University proton beam line.

The characteristics of FLUKA are benchmarked against the Eclipse TPS golden data for proton therapy. This project has been designed to access the dose distributions in a $10 \times 10 \times 10$ cm^3 water-filled phantom. These dose distributions are benchmarked against the dose delivered with very good quality Monte Carlo simulations. Treatment plans acquired from TPS are compared with plans obtained from FLUKA using the gamma analysis method.The same procedure is repeated for graphite as a phantom material, to estimate any variations in the results.

Chapter 2 of this thesis summarises the theoretical knowledge required to understand the basics of proton beam therapy, including a history of proton therapy (section 2.2), information about the interactions of proton with matter (section 2.3), proton therapy accelerators (section 2.6) and a detailed description about the proton beam delivery system and its techniques (section 2.3 and section 2.8).

Chapter 3 details the up to date literature about issues of range uncertainties related to proton beam therapy. The literature in this field has been reviewed (section 2.3) and included into the relevant sections. A detailed explanation of human bone structural formation has been given in section 3.3. A female flat skull bone is modeled in FLUKA to simulate the proton beam in order to estimate the range uncertainties associated with sub-CT resolution

heterogeneities in the path of the beam. Section 3.6 of chapter 3 in this thesis gives in-depth information about all procedures carried out to perform this analysis.

Chapter 4 clarifies the Monte Carlo and experimental outcomes as a benchmark of the effect of sub-CT resolution inhomogeneities in proton radiotherapy. Using Birmingham University's proton accelerator, an experiment has been performed with five SAWBONES® foam block phantoms of different densities to ascertain the effect of heterogeneous structures on the range of a proton beam. Section 4.3.2 and 4.4 briefly describe the whole procedure for this experiment. An analytical model of the experiment is developed in Monte Carlo simulator and the experimental results are affirmed by running simulations, details are given in section 4.6.

The main purpose of the work described in Chapter 5 is to benchmark the characteristics of FLUKA (a Monte Carlo code) against the Eclipse golden data for proton therapy. An introduction into radiation dosimetry and the concept of absorbed dose is given in section 5.2 and the concept of calorimetry is stated in section 5.3. Gamma analysis is a standard method of analysing the dose distribution in a detector system against the dose distribution assumed by the commercial treatment planning system. Section 5.4 explains the working principle of gamma analysis.

During the study period, I have also guided and provided support to two MSc students in the completion of their research projects. The first thesis is entitled "Modelling the range uncertainty of protons in lung tissue with FLUKA" by Charles Nathan Kimball-Smith (January 2018). He successfully run FLUKA Monte Carlo simulations to replicate the experiment performed at Birmingham University (proton beam line) to find changes in the spread of the Bragg peak as a function of foam density. The second thesis is entitled "The use of fine-structure spectroscopy techniques in determining proton range uncertainties" by Owen Thomas Williams (December 2018). The main focus of Owen's project was on determination of shifts in Bragg peak width and position for a range of pore sizes, bone lengths and densities. I plan to prepare sections of chapter 3, 4 and 5 for publication in the international scientific literature. The work is novel and will be of interest to proton radiotherapy physicists and researchers, due to the information it provides on the consideration of bone and other porous materials on range uncertainty. I have presented my work at various conferences and meetings

such as the Proton Physics Research and Implementation Group (PPRIG) workshop 2016 (London), Monte Carlo User Group Meeting (MCNEG) 2016, (Manchester) and Medical Physics and Engineering Conference (MPEC) 2018,(Yorkshire).

Chapter 2

Proton Beam Therapy Theory

This chapter primarily describes the fundamental physical interactions of protons and ions in matter within the energy range of the interest to radiotherapy and also explains how these interactions contribute to the absorbed dose in a medium. The classical dose distribution of ions is compared to that of conventional X-rays, which are commonly used in radiotherapy, and the benefits of using ions are also discussed. A short section follows characterising the traditional methods of acceleration and describes the conventional proton treatment delivery techniques in radiotherapy.

2.1 Radiation Therapy

Radiation therapy is one of the most commonly recommended treatments for cancer which is second only to surgery in its effectiveness. According to the National Radiotherapy Dataset (RTDS) and Cancer Research UK reports approximately 50% of all cancer patients currently receive radiotherapy at some point as a part of their treatment. Radiotherapy involves the use of high energy X-rays to destroy the cancer cells which can be either for a curative (cure the disease) or palliative (symptom relieving) purpose. The major focus of any type of radiation therapy is to achieve good tumor control with minimal normal tissue complications. This balance between the tumor control and normal tissue complications is acknowledged as the therapeutic ratio [20].

High-tech developments in the field of radiation therapy such as intensity-modulated

radiotherapy (IMRT), image-guided radiotherapy (IGRT) and 3D conformal radiotherapy (3DCRT) have enhanced the therapeutic ratio of such treatments by conforming the high dose regions more precisely to the target volume [21, 22]. However, due to the interaction behaviour of the X-ray, the dose delivered to the tumor is constrained by the amount of dose that can be delivered to the surrounded healthy tissues. Usually, the amount of the dose required to achieve essential tumor control, can not completely avoid causing damage to normal tissue [21]. Contemporary research on long-term cancer survivors has revealed a critically high amount of late toxicity effects related to the radiotherapy such as secondary cancer, cardiac defects and fertility complications [2, 23]. According to recent research, there are approximately 3.05 million cancer survivors who have been given radiotherapy as part of their cancer treatment. This number is suspected to reach 4.17 million cancer survivors by 2030 [24]. Therefore, much attention is paid on technical developments in radiation therapy to minimise the integral dose to the patients as well as late toxicity effects [2].

2.2 History and Principle of Proton Beam Therapy

Proton beam therapy is a globally emerging cancer treatment modality which utilises highly energetic positively charged particles to kill the cancer cells [25]. About fifty years after the discovery of X-rays, Robert Wilson, a physicist and the first director of Fermilab, proposed the use of protons for cancer treatment in 1946. The first treatments were performed in 1954 on approximately 30 patients with pituitary tumors at the Lawrence Berkeley National Laboratory, California [26]. The clinical use of the proton beam therapy has proliferated since 1946 and the first ever hospital-based proton therapy clinic was opened at Loma Linda University in 1990 [27]. The major obstruction facing proton therapy is that it is more expensive compared to using x-rays by a factor of about 2.4 [28]. Therefore, it is taking longer to have widely-available proton beam therapy centers. However, it has specifically gained attention of media and patients in the last 8 years [25, 29] and a number of hospital-based proton therapy facilities are now available worldwide. As of July 2017, there were 75 particle therapy centers at international level, with 41 others under construction [30].

Protons have the ability to travel a certain depth (based on the energy of the input

beam) before maximum energy deposition at a definite point in the medium, therefore the physical characteristics of proton beams differ remarkably from that of photons. Although, photons offer skin sparing and the dose at the skin surface is lower in general healthy tissues (both proximal and distal to the tumor) will receive a higher dose compared to that from the protons. [4, 31, 32]. In contrast, proton beams deposit a maximum dose within the so-called Bragg peak or SOBP and the dose distal to the tumor target falls rapidly as shown in figure 2.1). Consequently, the proton therapy techniques have the advantage of delivering more conformal and less integral dose to the tumor volume as compared to the photon treatment methods which is clinically significant [32, 33].

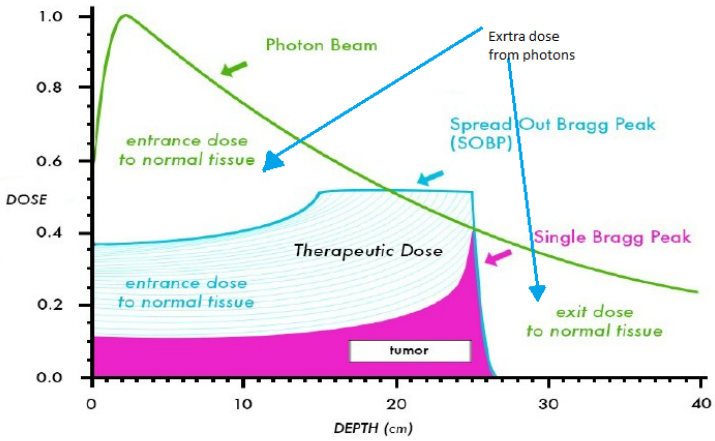

Figure 2.1: Differential depth dose distributions of photons versus protons. It can be seen that photons offer skin sparing and the dose at the skin surface is lower compared to that from the protons. Photons consistently deposit dose through the path in the medium and distal to the tumor the dose continues to decrease exponentially. In contrast for protons, the maximum dose deposition takes place at a definite depth within the so-called Bragg peak or SOBP (Spread Out Bragg Peak) and dose distal to the tumor falls rapidly (almost zero exit dose). This rapid fall-off of dose near the end of range helps to spare normal tissues. Therefore, a reduced volume of healthy tissues is exposed to intermediate and low doses of proton radiotherapy which results in a reduced co-irradiation of dose limiting organs at risk (OAR) [1]

.

Proton beams of energies varying from 200-250 MeV are required to achieve the range

of the order of 20-30 cm in tissue for treating deep-seated tumors. The size of a typical tumor is normally larger than the magnitude of a single Bragg peak. Therefore, the beam is modulated to confirm the dose as close as possible to the tumor volume. The combination of multiple modulated Bragg peaks is termed a Spread out Bragg Peak (SOBP), exemplified in figure 2.1. It is worth noting that with the production of SOBP, the tissue distal to the tumor receives a lower dose. The two most commonly used techniques for proton treatment are; i) passive scattering, where scattering foils are used to produce a large uniform radiation field, and ii) pencil beam scanning; to appropriately 'paint' the dose onto the tumor volume. The working principles are briefly explained in section 2.8 .

2.3 Interaction of Protons

In order to completely employ the clinical benefits of protons, it is essential to understand their interaction mechanism with matter. A proton's behavior is entirely different as compared to that of a photon when it comes into contact with a medium. The X-ray photons experience a number of interactions before imparting their energy or exiting the patient body. Photons lose their energy in the large steps and attenuate exponentially without having a pronounced or precise range inside the medium that they pass through. On the other hand, charged particles have a well-defined range inside the medium and undergo a large number of small interaction steps before depositing all of their energy. These steps are too small so that the energy loss seems to be continuous [26].

Protons having kinetic energy E will interact with atoms and molecules of the medium, that they go through. The various types of interaction are Coulomb interactions with atomic electrons and atomic nucleus, nuclear reactions and Bremsstrahlung. A proton on interaction with an atomic nucleus will transfer some of its energy to the nucleus with a change in its direction. As a proton is much lighter than most of the nuclei, its collision with the nucleus results in a small amount of energy loss. However, upon such interactions the proton completely deviates from its original path and in some cases it bounces back. Interactions with nuclei result in the emissions of some other charged particles such as alpha particles and gamma rays [34].

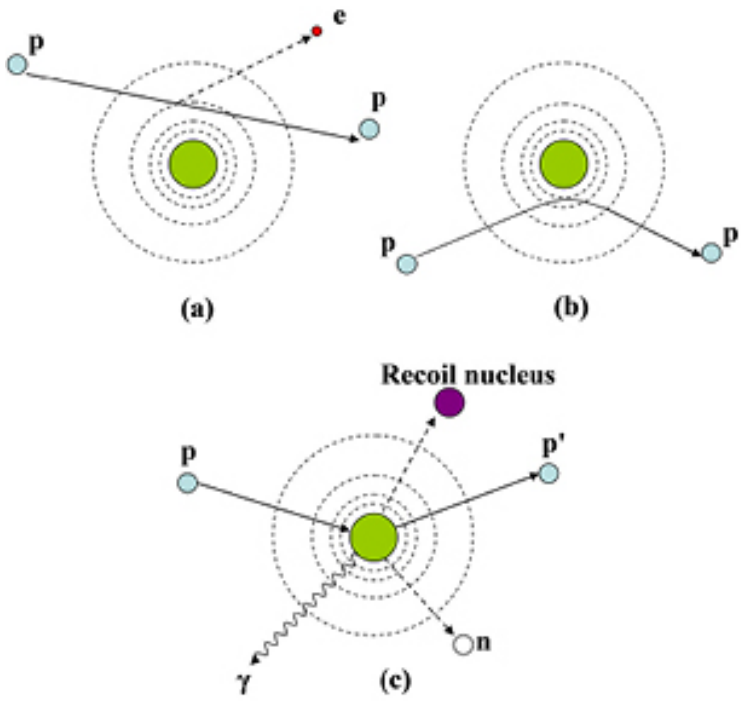

Figure 2.2: Schematic description of proton interaction processes (a) energy loss due to inelastic Coulombic interactions with orbiting electrons, (b) deflection of proton from its original path due to repulsive Coulomb elastic scattering with nucleus, (c) production of secondary particles due to non-elastic nuclear interaction [2]

.

Non-elastic nuclear reactions between a proton and an atomic nucleus result in the emission of protons, deuterons, tritons, heavier ions or one or more neutrons. Neutron emission as a result of nuclear reactions requires more attention for radiation shielding.

2.3.1 Coulomb Scatterings and Deposited Dose

Protons interact with matter mainly through Coulomb interactions with atomic electrons. Protons are positively charged particles with a rest mass of 1.67 x 10^{-27} kg (about 1800 times larger than the mass of electron) and a half life of 10^{35} years. As primary protons enter a medium, they undergo a Coulombic encounter with the orbiting electrons of the atoms in the medium causing ionisation or excitation. This interaction at the entrance results in a small proton energy loss. The energy loss per interaction is very small due to the mass difference

of the proton and electron, and the proton does not show any significant deflection with this interaction. The range of secondary electrons is negligible (less than 1 mm) and all the energy is considered to be deposited locally. However, this interaction process of protons with electrons passing close to the nucleus is not linear and independent of the density of the material they penetrate. Therefore, as long as the particle traverses the medium, the energy of protons is lowered which leads to a rapid increase in the number of ionisation events and the formation of a Bragg peak. Right after the Bragg peak, the number of ionisations is reduced to zero. Protons may undergo interactions with thousands or millions of electrons

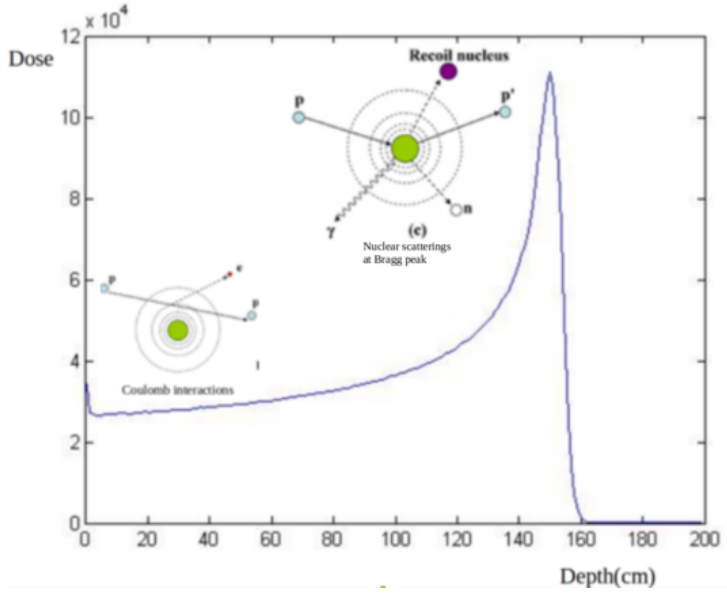

Figure 2.3: Proton Coulomb Scattering. Due to Coulomb interactions, the velocity of the proton slows down before the Bragg peak which results in an increase in the stopping power versus a decrease in proton energy at the Bragg peak. The proton also interacts with the nucleus and emits secondary neutrons and γ-rays [2]

.

per centimeter of the medium. This process is non-linear and the rate of change of the energy as a function of the transmittance of the material ($\frac{dE}{dX}$) can be calculated using the following Bethe-Bloch formula:

$$-\frac{1}{\rho}\frac{dE}{dX} = K\frac{Z}{A}\left(\frac{z}{\beta}\right)^2\left[ln\left(\frac{2m_e c^2\beta^2\gamma^2}{I}\right) - \beta^2 - \frac{\delta}{2} - \frac{C}{Z}\right] \tag{2.1}$$

with $K = 4\pi N_A r_e^2 m_e c^2$

N is Avogadro number, e is the electric charge of the electron, m_e is the mass of electron, Z and A are the atomic number and atomic weight of the absorbing material, c is the speed of light, $\beta = v/c$ while v is the velocity of the projectile, I is the mean excitation potential of the absorber, $\gamma = (1-\beta^2)^{-}\frac{1}{2}$, δ is the density correction factor and C is the shell correction item which is only important for low energies when the particle velocity is nearly equal to the velocity of the atomic electrons.

2.4 Stopping Power

High energy particles interact with electrons more frequently by losing energy continuously along their path length. Depending on interaction extent, the charged particles transport their energy either by excitation (where electrons are raised to higher energy levels) or the ionisation, which results in the production of ion pairs in the surrounding matter. This creation of ion pairs as a result of ionisation is based on the energy gained from the charged particles. This loss of kinetic energy causes a deceleration in the charged particles which is known as the stopping power, S:

$$S(E) = -\frac{d(E)}{d(x)} = n_{ion}\bar{I}, \tag{2.2}$$

where E is the kinetic energy of the charged particles, n_{ion} is the number of electron-ion pairs formed per unit path length and $\bar{I}$ is the mean energy required to ionise an atom in the medium. The value of S increases with a decrease in velocity of charged particles. The stopping power depends on both the type and initial energy of the charged particles. High density materials usually have greater stopping power due to frequent interactions between the atomic electrons. The measurements for the stopping power of protons as well as their range through different materials can be found from the National Institute of Standards and Technology (NIST) database 124 [3]. This database calculates the values according to methods explained in ICRU reports 37 and 49. An example of the stopping power of protons in water and cortical bone is shown in figure 2.4 and 2.5respectively.

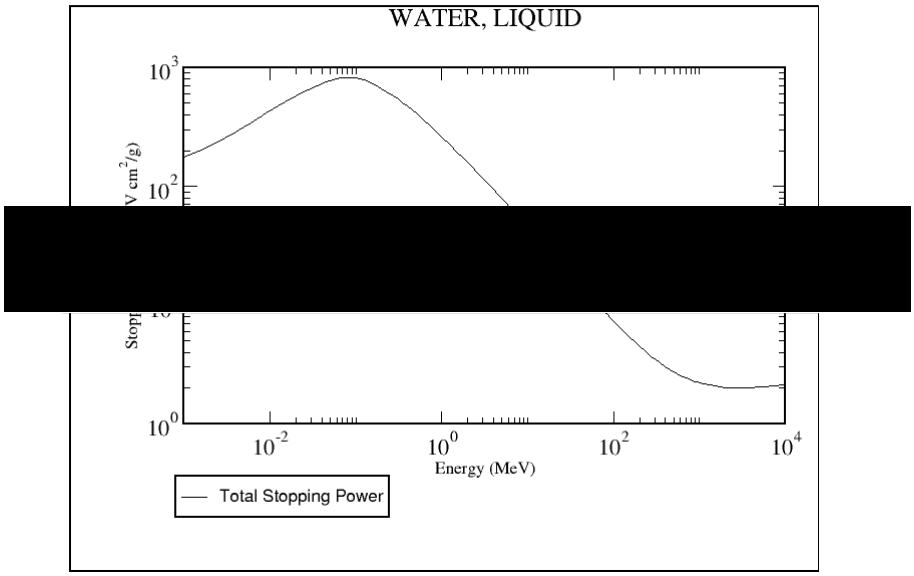

Figure 2.4: Mass collision stopping power of proton in liquid water (taken from [3])

.

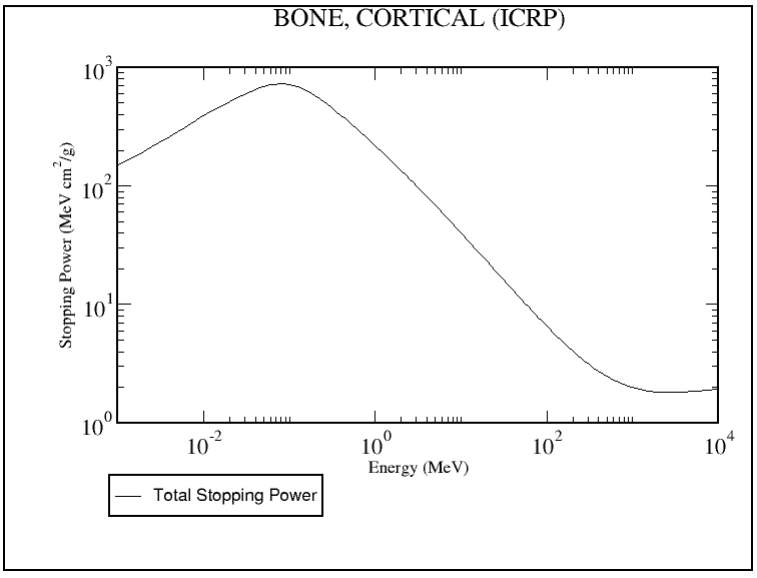

Figure 2.5: Stopping power of proton in cortical bone (adopted from NIST [3])

.

2.5 Range and Range Straggling

2.5.1 Range

The range of protons is defined as the mean distance it travels through the material before it comes to rest. It usually depends on the initial energy of the particle, the composition of the medium that it passes through and type of the particles. Conventionally, the stopping power expression has been used for estimation of the range of the particles. This determined range is named as continuous slowing down approximation (CSDA) range. For example, for a charged particle with initial kinetic energy, E_0, the CSDA range in terms of mass stopping power can be calculated as:

$$R_{CSDA} = \int_0^{E0} \left(\frac{1}{\rho}\frac{dE}{dX}\right) \mathrm{dX} \tag{2.3}$$

R_{CSDA} is given in $\mathrm{g/cm^2}$ [35].

The depth for the formation of the Bragg peak inside any medium is directly related to the initial energy of the proton beam. Therefore, the higher the energy of the beam the deeper the Bragg peak in the medium. In clinical practice, the proton beams with initial energies between 70 to 250 MeV have been used for cancer treatment which employ maximum Bragg peak ranges of 30 cm to 32 cm in water, while, a monoenergetic proton beam having initial energy of less than 70 MeV has been used for treatment of eye cancer [36]. Figure 2.6 demonstrates the relationship between energy and range for monoenergetic proton beams in water. It can be clearly seen that a beam with a higher value of initial energy will penetrate to a greater depth in water.

2.5.2 Range straggling

As all protons travelling through the same medium with the same initial kinetic energy do not stop at a same depth. It is because all traversing particles would not have the same amount of energy loss due to collisions along their path. Actually, the energy loss process is statistical in nature which gradually brings the particle to rest over a range of distances and results in range variance. These variations in the proton range is termed as range straggling

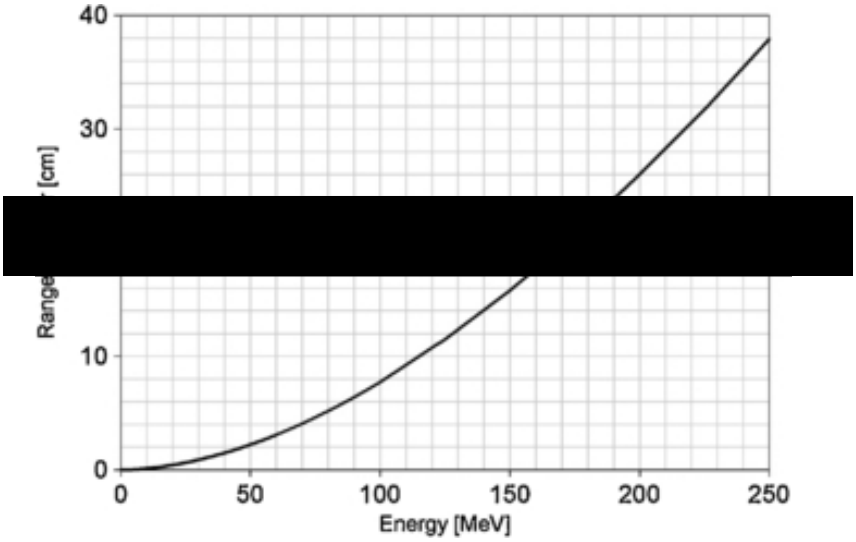

Figure 2.6: Plot for range of protons in water based on continuous slowing down approximation as a function of energy of proton beam (taken from [4]).

and the variation in proton energy at a particular depth is called energy straggling [37].

2.6 Accelerators

Particle accelerators are the scientific instruments that have been used to accelerate and align the stream of elementary particles (such as protons and electrons) up to a required energy level. Three commonly used accelerators are known as linear accelerators, cyclotrons and synchrotrons. The choice of any specific accelerator depends upon its usability and the medical requirements in the field of radiation therapy.

2.6.1 Linear Accelerator

Linear accelerators have a large number of applications, from the production of X-rays for medical purposes, to being an injector for higher-energy accelerators, to the investigation of the properties of subatomic particles. The construction of a linear accelerator depends on the type of particle that is being accelerated: electrons, protons or ions. Linear accelerators are used in external beam radiation therapy to customise high energy x-rays or electrons to conform dose to a tumor's shape and destroy cancer cells while sparing surrounding healthy

tissue. However, the electric field strength in these conventional linear accelerators is not sufficient to accelerate protons or heavier charged particles to the required high energy level. Therefore, synchrotron and cyclotron are two extensively used accelerators for the production of high energy proton beams.

2.6.2 Cyclotron

A cyclotron is a charged particle accelerator which has been specifically used to accelerate positively charged particles such as protons and deuterons. The very first circular accelerators were cyclotrons invented in 1929 by Ernest O. Lawrence at the University of California, Berkeley. In 1950, John Lawrence who was a medical doctor and brother of Earnest Lawrence, used highly energetic charged particle beams extracted from a 60-inch cyclotron for cancer treatment in Berkeley. The same treatment patterns were copied for the treatment of cancer patients at Uppsala (Sweden) in 1957 and in Boston (USA) in 1961. Since that time, the number of treatment facilities has increased worldwide and hospital-based cyclotrons have replaced research cyclotrons. Proton accelerating cyclotrons use electrical power to accelerate the charged particles in a helical path therefore these are able to produce extremely high energy proton beams ($E = 230$MeV). A proton beam of desired energy and intensity is extracted and delivered to the patient's body through a specially designed beam transportation and modulation system (for details see section 2.7.1).

A cyclotron mainly consists of highly evacuated semicircular metal cylinder divided into two halves and powerful electromagnets. The cylindrical sections are named as 'dees' which are placed between two poles of magnets. A schematic diagram of a cyclotron has been shown in the Figure 2.7. Protons are placed at a central position between the two dees and an alternating current is supplied at two terminals of the Dees. These protons are accelerated due to the high frequency alternating voltage. The presence of a magnetic field force the particles to travel in a spiral path. Frequently changing the frequency of the alternating potential helps the particles to travel from one dee to another and thus on each pass the particles gain more energy with an increased radius size. At maximum acceleration, the particles reach the inner edge of the cyclotron and are directed outside the cyclotron by deflector magnets to the beam transport system [6].

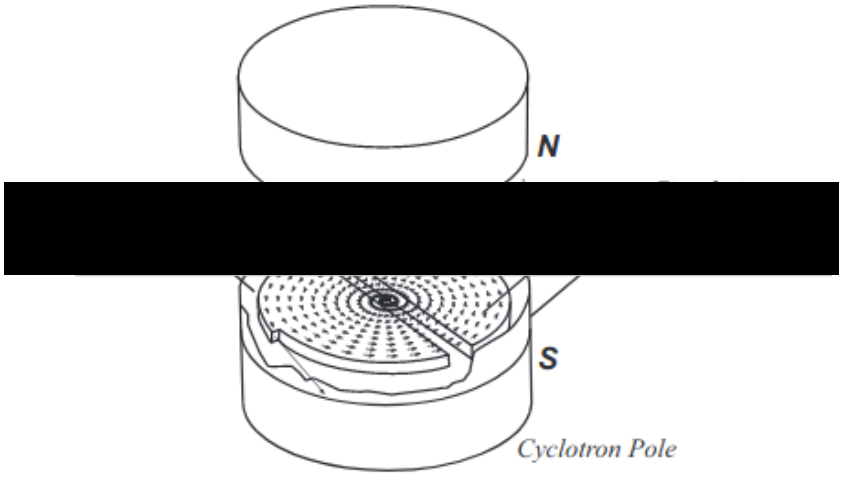

Figure 2.7: A schematic diagram of a cyclotron. An ion source is located at the centre of an evacuated cylindrical chamber, between the poles of an electromagnet that creates a uniform field perpendicular to the flat faces. The source of the voltage is an oscillator that operates at a frequency equal to the frequency of revolution of the particles in the magnetic field. The accelerated particles follow semicircular paths of continually increasing radius [5]

.

2.6.3 Synchrotrons

A synchrotron is a circular-shaped particle accelerator which utilise a series of magnets to accelerate charged particles. Cyclotron accelerate the charge particles in a spiral path up to a maximum energy of 10 MeV energy while keeping the magnetic field constant. On the other hand, a synchrotron regulates the magnetic field to accelerate the charge particles along a circular path with an ability to accelerate protons up to energy of 10 GeV.

A schematic diagram of a proton synchrotron can be seen in figure 2.8. It consists of a vacuum chamber (doughnut) which is decked with a number of electromagnets. Usually, a proton beam of 3 MeV to 7 MeV, steered from a linear accelerator is injected into the chamber where these magnets keep the particles in motion in a circular path. An accelerating radio frequency (RF) accelerates the beam particles more frequently. The strength of the magnetic field and the radio frequency varies with a change in the beam energy, the more the beam energy, the higher will be the strength of the magnetic field and RF. This process continues

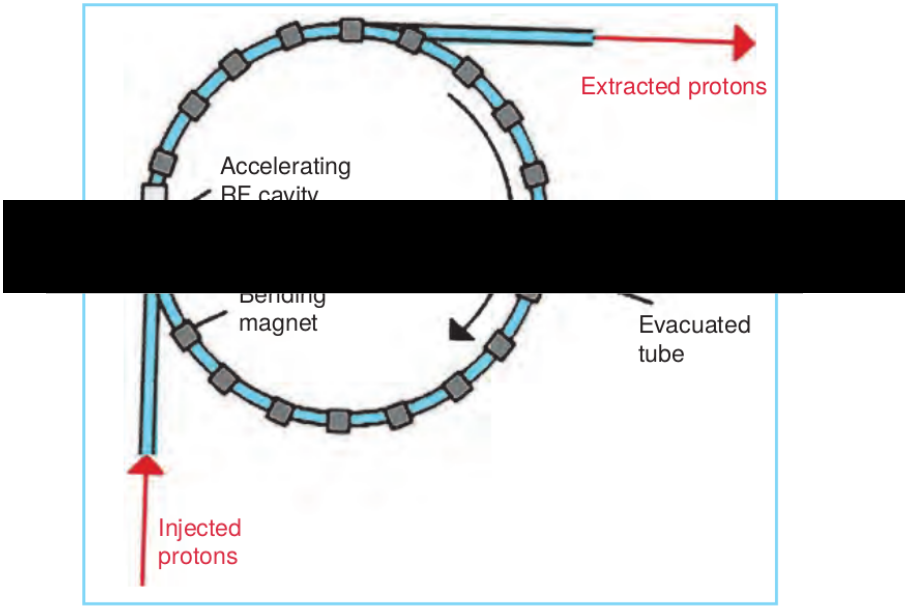

Figure 2.8: Schematic diagram representing the working principle of a proton synchrotron for accelerating protons (image is taken from [6])

.

until the beam reaches the required energy level and extracted for the clinical use [6, 38].

2.7 Proton Beam Delivery System

The proton beam delivery system usually comprises three main components: an accelerator to produce a high energy proton beam, a transport system to extract the beam from the accelerator and direct it to the beam nozzle, and a beam nozzle which has been designed to shape and filter the proton beam for delivering the required dose to the target volume. Beam accelerators have already been discussed in section 2.6. The beam transport system transfers the protons extracted from the accelerator to the beam nozzle; the proton beam is transported horizontally. The beam transport system consists of beam bending magnets, focusing quadrupole magnets, beam switching, shaping and monitoring devices and a single or multiple gantries. The gantry plays an important role to enable the rotation of the beam around the patient's body from any direction instead of changing the patient's position.

2.7.1 Proton Therapy Beam Line

Proton therapy systems are massively large; some are the length of a football field and 3 storeys tall. Most of the equipment hides behind the walls and is invisible to the patient inside the treatment room.

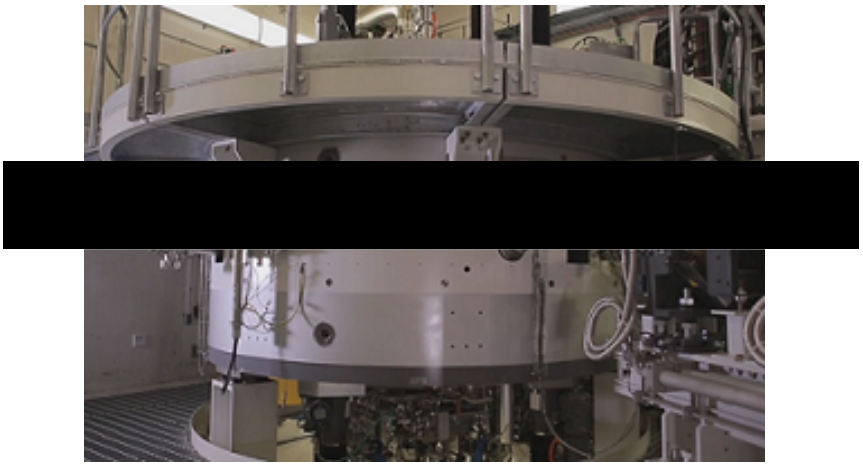

Figure 2.9: VARIAN cyclotron at the NHS' first high-energy proton beam cancer treatment centre in the UK (The Christi Hospital, Manchester [7]).

Positively charged protons are extracted from the hydrogen atom and shot into the cyclotron (particle accelerator) where the presence of static magnets and radio frequency (RF) fields help to accelerate the protons up to 2/3 the speed of light. The direction of acceleration is outwards from the centre of the cyclotron in a circular pattern. As long as the protons move further away from the centre, they gain more speed and become highly energetic (e.g. 230 MeV). The Extraction magnets pull these protons away from the cyclotron and inject them into the beam line. The energy selection system (ESS) helps to alter the extracted beam's energy in order to align with the depth and extent of the tumor within the patient's body. The energy of the clinical beams varies from 70 MeV to 230 MeV depending upon the extent of the tumor. The ESS is made up of mechanical carbon wedges that are driven into the proton beam. The energy selection system enables the highest beam's energy selection (depending upon the depth of the tumor) to treat the deepest layer first. Then the energy of the beam is gradually lowered to paint all layers until the whole tumor volume is covered by the proton dose distribution. The proton beam travels down to the beam line from the

ESS. The beam lines work as a connector between the cyclotron and treatment gantry. It

Figure 2.10: The energy selection system (ESS) at the Proton Beam Therapy centre, the Christie Hospital, Manchester [?].

comprises of multiple magnets used for beam modifications according to the tumor shape etc. The most commonly used types of magnets in the beam line are quadrupole and dipole electromagnets. Quadruaple magnets are used to profile the proton beam into a pencil shape and shield the outward spread of the proton beam. The water cooling system is used to keep the magnets cool, as the hot magnets would easily change the physical beam size and the beam would not be precisely focused at the target in that case. The other set of electromagnets are called dipole magnets which guide the proton beam into each gantry inside the treatment room where protons will encounter the nozzle. The nozzle is designed with certain characteristics for precise dose delivery. It has a potential to deflect the incoming proton beam into two planes to authorise the beam delivery at two different depths. The nozzle has a facility to measure the proton beam and ability for feedback to the treatment system to ensure accurate dose delivery. The nozzle is also equipped with imaging panels which are used to detect the exit dose from the patient to form an image. The VARIAN ProBeam^{TM} systems installed at The Christie Hospital are constructed with 2D kV and 3D Cone Beam

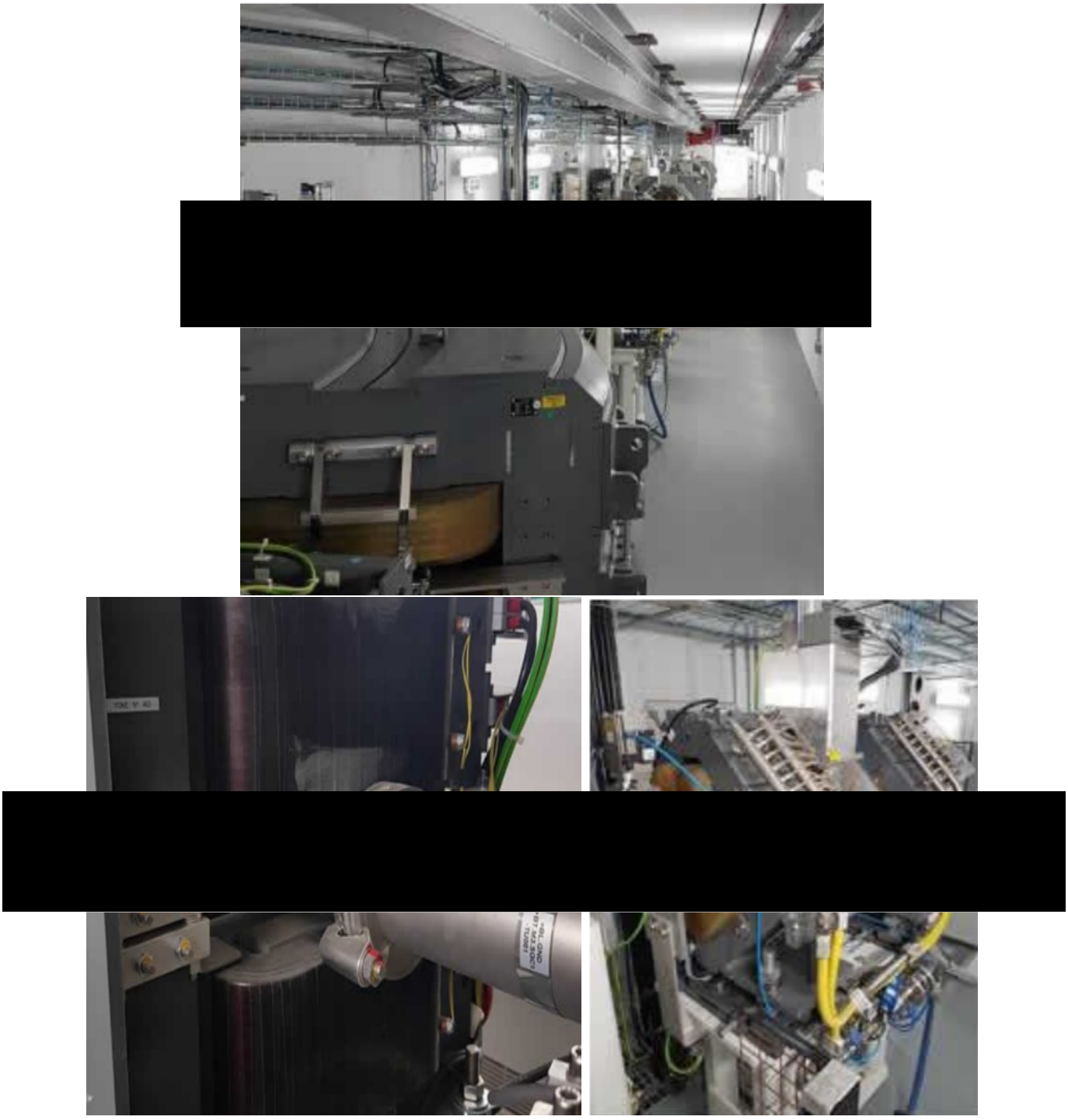

Figure 2.11: Different sctions of Proton beam line at The Christie Hospital, Manchester (top, eye-view of the beamline, bottom right to left 135 dgeree dipole magnet and quadrapole electromagnets) [?].

CT (CBCT) imaging to confirm the patient's position for error-free treatment delivery. The gantry has ability for 360 degrees rotation around the patient to guarantee best treatment angle for accurate dose delivery.

2.8 Proton Beam Delivery Methods

When the proton beam enters the treatment room, its size and divergence is that of a pencil beam (a few millimeters diameter with low divergence) that might not be sufficient to cover the whole treatment volume. So, in order to cover the whole treatment volume, further beam settings are required. For appropriate beam delivery, there are two most commonly used approaches available today which are known as active scanning and passive scattering methods. Passive scattering distributions involve the process of scattering the proton beam and using a sequence of blocks and apertures to attain the dose conformity while active scanning deliveries commonly involve scanning a narrow pencil beam over the targeted tumor volume [26].

2.8.1 Passive Scattering

In passive scattering techniques, a spreading or scattering material is placed in the beam path in order to spread it according to the size of the treatment volume. For small field coverage, even a single scatter is sufficient to broaden the beam in order to cover the tumor volume. However, for larger field sizes, a second scatter is required to ensure a uniform dose profile. For passive scattering an energy modulator, two scattering foils, a collimator and a compensator are used to modulate and contour the beam for uniform dose coverage to the tumor volume. Figure 2.12 describes the basic principle of passive scattering. An energy modulator adjust the beam energy which would be sufficient to reach the target. The double scattering system plays an important role to spread the narrow monoenergetic proton beam to widen it accordingly. Afterwards, the collimator aperture adjust the shape of the proton beam up to the size of the tumor volume. The compensator shapes the proton dose distributions at the distal end of the treatment volume [8, 39].

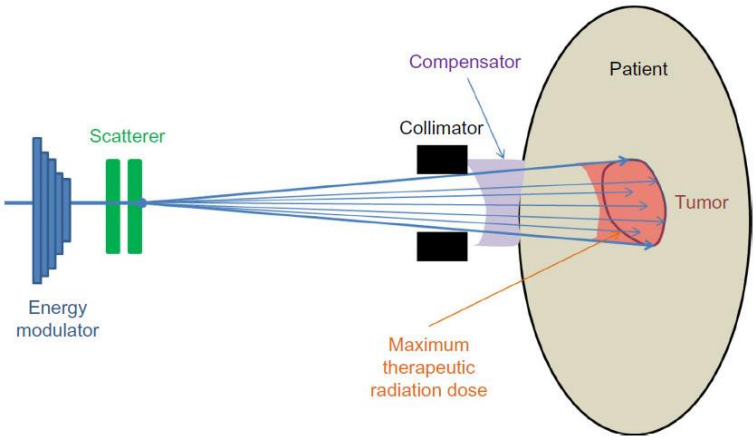

Figure 2.12: A schematic representation of the basic principle of passive scattering. The energy modulator, two scattering foils, collimator and compensator are used to modulate and contour the beam to deliver a uniform dose to the tumor volume [8].

2.8.2 Active Spreading

Another widely used proton beam delivery technique is called active spreading or spot scanning where the radiation dose dispersal is supervised by scanning magnets rather than collimators or scatter foils. This technique is quite simple based on the fact that the protons being charged particles sustain Lorentz forces. Therefore, when protons encounter with the electric field they gain acceleration and get deflected when they are subjected to a magnetic field [40]. Figure 2.13 demonstrates the principle of the spot scanning procedure. The accelerated proton pencil beam coming from cyclotron is interrupted by a pair of orthogonal magnets and diverted in a prudent direction by controlling the magnet's intensity. A small spot, usually of 10 mm diameter at full-width-half-maximum (FWHM) is magnetically scanned across the tumor volume to form different layers of equal energy [41]. These layers do not necessarily lie in the same plane because of different densities in the patient's body. However, the treatment volume can be accurately scanned in three dimensions. The deepest layers are painted first then the incoming beam energy is reduced step-by-step to cover the next layers. This process is continued until all layers inside the planned target volume (PTV) have been irradiated. This technique also makes intensity modulated proton therapy (IMPT) possible. For IMPT the dose distribution is controlled inside each voxel and

by changing either the beam intensity or the scan speed or both, the dose is delivered on a field-by-field basis to achieve a uniform dose around the whole target.

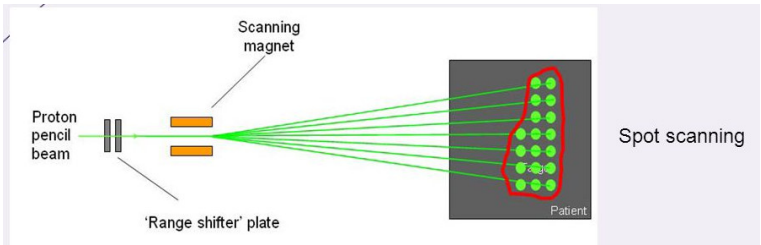

Figure 2.13: A schematic representation of the basic principle of passive scattering. In principle, the energy modulator, scatterer, collimator, and the compensator work together to ensure that the radiation dose to distal and lateral side of the target is highly conformal [9].

The active scanning proton therapy technique has many advantages. The first benefit is reduction in the nuclear contaminated dose outside the PTV, as in this technique the dose distribution can be shaped to the target without using physical compensators in the beam path which cause the production of neutrons. Moreover, the active scanning technique reduces the treatment time and shows the best dosimetric advantages in both the low-dose and high-dose regions of PTV compared to the passive scattering treatment method.

One disadvantage for the spot scanning proton therapy treatment is its sensitivity to organ motion or patient positioning. For example in case of a lung tumor, there are chances to destroy the target volume due to the organ's continuous motion. The best possible way to reduce this risk is the use of an image guidance-technique during spot scanning to help to design effective re-paintings for the missing volume in multiple scans of the volume.

2.9 Summary

The technologies associated with the proton beam therapy have been discussed in this chapter. In next chapter a simple model of flat skull-bone will be considered for treatment of brain tumor.

Chapter 3

Estimation of Range Uncertainties in Brain Proton Therapy due to Heterogeneities in Trabeculae of Skull-plate

This chapter highlights one of the major concerns that still need considration for planning a proton therapy treatment. Proton therapy beams get scattered on traversing through the inhomogeneous material. This scattering of protons through heterogeneous material leads to a broadening of the range along straight ray-paths that is a consequence of the differing paths that the proton can take through media. The literature reviews about this scattering phenomenon are described in this chapter. A short section explains the typical bone structure and its classifications. The bone-substitute material, SAWBONES®, ranging in density from 0.088 g/cc to 0.48 g/cc has been used to simulate bone heterogeneities.

3.1 Contemporary Literature

Proton therapy is one of the most effective techniques in radiation therapy for cancer treatment. The proton beam therapy is not a new technology and has been in use for the last 64 years [42]. From 1989 until 2017, the only facility available in the United Kingdom (UK)

was the National Centre for Eye Proton Therapy at the Clatterbridge Cancer Centre. This site is equipped with a 60 MeV proton beam line which has a maximum range of 31 mm in water and is exceptionally suitable for treating any position within the eye [43]. Proton therapy has arrived in the UK for other cancer treatments and The Rutherford Cancer Centre in South Wales treated their first prostate cancer patient in April 2018 [44]. All three proton therapy gantries at The Christie Hospital NHS Foundation Trust in Manchester and The University College London Hospital (UCLH) NHS Foundation are now operational for treating the patients [42, 45]. The main justification for the choice of proton therapy is the physical behaviour of particles and formation of Bragg peak at a certain depth. A detailed description about proton interaction process is given in Chapter 2.

For precise dose delivery it is essential to have an accurate knowledge of the proton beam in the material. As misinterpretation of proton range may cause the Bragg peak to occur outside of the tumor volume which may cause an under-dose to the treatment site or miss some of the treatment volume and overdose to the surrounding normal tissues and organs. Literature on proton therapy commonly focuses on two major aspects. One of which is related to finding methods for improvement in the accuracy of predicting or measuring the range of protons in different materials. The second one discusses which size tumours would be appropriate for treating with protons rather than conventional x-ray radiotherapy as very large proton beams result in a potentially worse dose distributions on the near side of the tumour [2, 46] .

In 2000, a study by Alfredo Zurlo et al. [47] investigated the potential for proton therapy on large abdominal tumors. At that time available treatment planning software was used to design optimal treatments of 50Gy to the planned treatment volume (PTV) in a series of pancreatic and biliary duct tumors using X-ray photon and also proton planning. It was found that the proton beams were able to deliver 50Gy to the PTV with a 9 beam arrangement without exceeding the dose limits to the tissue structures surrounding the PTVs. None of the photon plans produced were able to remain within the dose constraints. They also found that for proton plans the field within the PTV was more homogeneous than the photon plans.

For proton therapy planning, the intensity modulation radiation therapy (IMRT) tech-

nique has been extensively used and Professor Antony Lomax inquired about the merits of IMRT in proton therapy. Lomax paper was published in 1999 [10] and explains four different approaches for use of intensity modulation in proton therapy. The term intensity modulation in proton therapy means that the proton beam will not be monoenergetic and it allows the protons of different energies to ionise at different lengths along the beam path. Figure 3.1 is taken from this paper to explore the effect of four different IMRT techniques on the Bragg peaks along the proton path lines. Examples A and C show the effect of dose build-up by different energies proximal to PTV for 2D modulations. Only a 3D modulation was presumed to be a promising method for using IMRT on complex tumors. However, a major

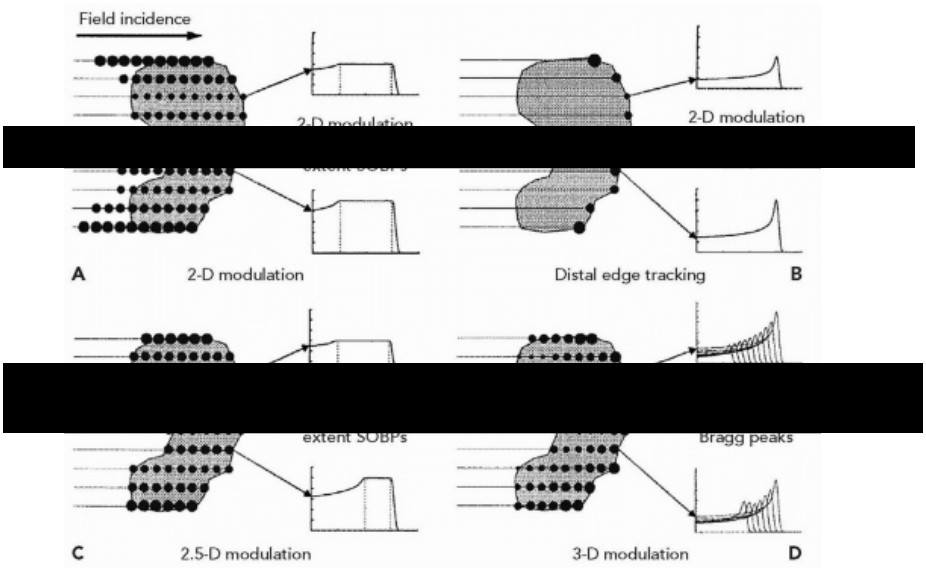

Figure 3.1: Four different IMRT modes used in proton therapy treatments. Images are taken from the reference [10].

drawback of using IMRT in proton therapy is that it increase the chance for recurrence of secondary cancers. This effect was explored by Eric Hall [48] and he reported more particle's leakage due to higher monitor units spotted by the proton beam. It was prescribed that the use of pencil beam proton therapy as a surrogate for x-ray can reduce the risks of secondary cancers. This factor is very age dependent as it has been observed that the risk for secondary cancers may be less relevant to an older person but for children this would make a suitable alternative treatment and it was later on approved by Maryam Moteabbed [49].

Range uncertainties in proton therapy can be caused for many reasons such as movement of organs, medium inhomogeneities, patient set-up and anatomical changes, biological considerations and computational processes. One main problem confronting radiotherapy is organ motion. Various approaches have been introduced to overcome this problem such as the breath holding technique and use of a CT scanner during X-ray radiotherapy treatment to make adjustments based on organ position. For lung cancer patients, it is quite important to have accurate knowledge about the beam range as the Bragg peak broadens due to heterogeneity in the human lungs which can cause under-dose to the target volume and overdose to the healthy tissues lateral to the target [50,51] which could seriously impact the dose distributions in lung cancer patients [52]. A paper by Alejandro Carabe and his

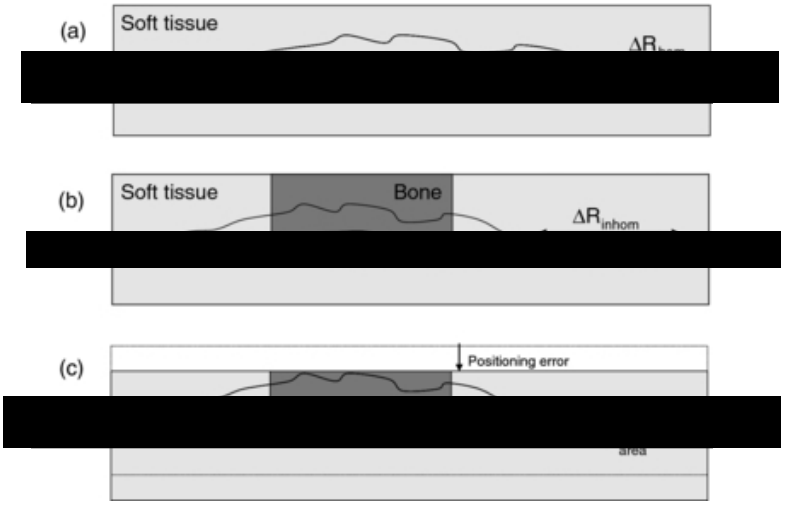

Figure 3.2: The effects of variable path lenghts,heterogenities and total distance travelled on the range of proton beam. Figure taken from the Lomax paper [11]

.

colleagues describes the variations in distal fall-off with changes in the biological effectiveness of protons [53]. By reducing the proton range uncertainties, it is possible to generate highly precise treatment plans for PTVs with a higher dose. The proton range experiences potential effects due to the presence of density heterogeneities in the beam path. In 2008, a study by Lomax [11] investigated the prospective effects of inhomogeneities present in the traversing medium. Figure3.2 show how small deviations can result in streaking or spreading of the Bragg peak required for that energy. Some other papers by Sawakuchi [51] and Urie [54]

shows the smearing of distal fall-off and broadening of the Bragg peak due to heterogenities in the beam path.

3.2 Proton Therapy for Brain Tumour

The treatment of brain and skull base tumors is still considered difficult for many reasons. Some brain tumors such as high-grade gliomas and meningiomas are identified by their hostile morphology. The presence of organs at risk (OAR) adjacent to the tumor volume especially in the skull-based lesions, demands precise treatment planning and delivery to ideally avoid these radiosensitive structures. Comparative to all other cancers, the brain tumor occurence rate is low but mortality rates are high. About 9000 patients are diagnosed with a primary brain tumor each year in the United Kingdom (UK). While, 16,000 patients encounter brain metastasis from other primary cancer sites and 250 children (aged 0 to 14 years) lose their lives to cancer every year [55, 56]. The Central Brain Tumour Registry of the United States (CBTRUS) reported that 16,830 deaths were attributed to primary malignant brain and other CNS tumors in the US in 2018 [57].

Proton beam therapy, for treatment of almost all kinds of cancer is gaining global significance in the clinical environment. The primary reason for this increased interest in proton therapy is the dose deposition characteristics of protons which are entirely different from the conventionally used x-ray photons [58]. The proton beams enter into the medium with a minimal entrance dose and deposit their maximum energy at a well-defined distal fall-off position by forming a peak (known as Pristine Bragg Peak) near the end of the proton range and leaves the medium with a comparatively lower to photons exit dose [59]. The distal fall-off position is considered to be the distance between 80-20% of the dose location [60]. This behaviour of protons allows the maximum precise dose to the target volume and helps to spare the normal tissues around the treatment volume.

Despite these physical dose distribution characteristics, there are still certain issues contingent to sources of uncertainties in proton therapy planning and dose delivery. These uncertainties may be caused for many reasons and few of them include error in targeted volume delineation in 3D imaging, imaging artifacts, tissue heterogeneities, patient set-up

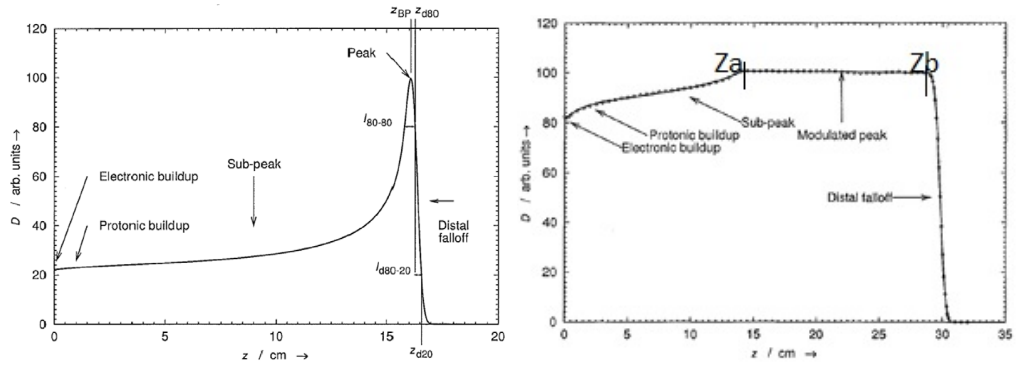

(a) Pristine Bragg Peak *(b) SOBP Depth dose profile.*

Figure 3.3: Specification of proton Pristine Bragg Peak (a) and Spread out Bragg peak (SOBP) (b). We can see the peaks for absorbed dose as a function of depth (cm) in water [2]

.

errors, motion induced uncertainties (e.g. lung and liver), physiological changes in diseased tissues and anatomical changes during the course of treatment and range degradation of proton beams due to different tissue densities in their passage. Proton beams have finite penetration depth through the material which depends upon the energy of the beam and stopping power of the irradiated substance. These penetration depths for different beam energies are controllable as far as the beams penetrate through a homogeneous material of known density. However, in case of patient treatment, the tissue heterogeneities and their intra-fractional variance in path of proton beam cause random uncertainties in the beam range; thus, leading to the range degradation. Therefore, exact knowledge of accurate range is important and special attention is needed for appropriate and precise proton dose delivery. An underestimation of range may cause a lower dose or no dose to a certain part of the tumor and overestimation may cause over-dosage to the volume and healthy tissues in the surrounding healthy tissues that might be lethal for the patient. The literature also indicates that the Bragg peak is broadened and distal fall-off is degraded when a proton beam passes through a heterogeneous medium [52, 59, 61]. Baumann et al. and Titt et al. [60, 62] also showed degradation in the Bragg peak by beam passage through the sub-millimeter-sized heterogeneities present in the lung equivalent materials and mentioned the importance of accounting for this accurate treatment planning. In another work by Sawakuchi et al. [59] a

model with voxelised geometry representing the density heterogeneities has been utilised to determine the range uncertainties in Bragg peak distal fall-off. The MCNPX Monte Carlo source code has been utilised for that project to simulate the effect on a 220 MeV proton beam and complexity of the phantom which included multiple slabs of centimeter widths filled with air and cortical bone densities.

In the present study Monte Carlo modelling with FLUKA code has been used to examine proton scattering in a bone-like tissue substitute. A model of the human flat skull bone has been constructed using layers of cortical bone and trabecular bone and the effect on the range of a 100 MeV proton beam is examined, simulating typical proton therapy of the brain. In particular, the model simulates the practice of using flat skull bone as an entrance surface as opposed to traversing more complex and thick bones (e.g. base of skull) of the skull. The overall thickness of the bone was 7.1 mm and the trabecular layer was 2.3 mm. The voxel dimensions in the micro-CT data were manipulated to simulate variations in trabecular pore size, from approximately 0.4 to 4 mm diameter. The proton beam was square field of 4×4 mm^2 which therefore traversed many pores at one extreme and fewer pores for larger voxel sizes. Random sampling of the region was taken from the bone substitute and employed to obtain the statistical variations in the texture. The range of the proton beam and the spread of the Bragg peak was determined and examined as a function of pore size. The range was found to vary by 0.08 mm, with an $R^2 = 0.07$, suggesting that only a small part of the variation was demonstrated to be systematic. The results therefore confirm that sub CT heterogeneity is unlikely to result in significant uncertainties, given the practice of irradiating through flat bone; however, for a larger thickness of trabecular bone, e.g. greater than 20 mm, range uncertainties of the order of 1 mm may be present.

3.3 Human Skeletal System

An in-depth understanding about human bones was essential to carry out this project. Therefore, a literature review has been conducted to acquire information about bones and their composition. Actually, both the bones and joints together form the human skeletal system which provides support and shape to the whole body. An adult human skeletal system is

composed of 206 bones; however, there is some evidences found about the variation in this number from person to person [63]. Red blood cells are produced in the bone marrow while minerals and fats are stored in the bones. Bones help to protect soft tissues such as those in the brain, various internal organs such as the ribs. Bones also provide protection to the heart etc. and play an important role for body motion.

3.3.1 Classification of Bones

Bones are divided into five main categories based on their shape and size such as long bones, short bones, flat bones, irregular bones and sesamoid bones or round bones. Long bones are

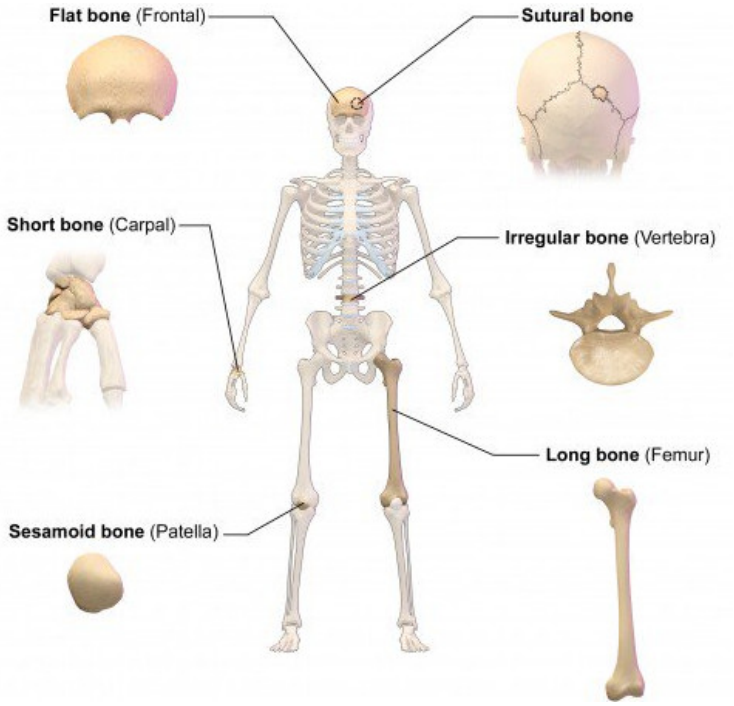

Figure 3.4: Different types of human bones [12].

always hard at ends and play a vital role for movement such as thigh-bone, tibia and the forearm. Short bones have almost similar length and width so they look somehow cubical in shape. These bones help to maintain stability and provide support with very little or no motion. The bones of ankles and the carpals in the hand are examples of short bones. Flat bones look like a plate having a broad surface. Flat bones include the scapulae, ilium,

sternum and some skull bones. The irregular bones in the human body can be seen in different shapes and usually interconnected to different other bones. Irregular bones perform various functions in the human body such as the vertebrae protect the spinal cord, facial bones give shape and the hyoid bone serves for tongue attachment. The fifth group of bones include the sesamoid bones, they are round in shape and comprise of small independent bones and developed in tendons. The kneecap is an example of a large sesamoid bone [14, 63].

3.3.2 Structure of Bone

There are two basic types of bone tissues; classified as compact bones and trabecular bones. Figure 3.5 shows two types of bones. The compact bone is also known as a cortical or hard bone and it forms about 80% of an adult human skeleton while the remaining 20% is composed of cancellous (also known as trabecular or spongy) bone. The cortical bone is harder, thick and surrounds the marrow space. The compact bone forms the structure of the long bones. Spongy bone is mostly found at the ends of long bones and consists of irregular honeycomb-like structures which are called trabeculae and are occupied by bone marrow inside [14]. The bone marrow is classified as red and yellow. At birth, all the bone marrow is found to be red while with ageing its colour turns to be yellow. Homoeostasis is the process of bone reformation taking place by three different types of cells found in bones. These cells are osteoblasts, osteoclasts and osteocytes. Osteoblasts are found in the bone marrow and work in a team to construct the new bone (osteoid) which regulates the amount of bone minerals and calcium. Osteoclasts are large cells and contribute to bone resorption or breakdown. Osteoblasts and osteocytes together maintain bone tissue. Osteocytes are the fully grown cells which can feel any pressure or cracks inside the bone and instruct the osteoclasts where to dissolve the bone.

3.4 Skull Bone

The human skull is made up of 22 bones and provides protection to the brain. The facial skeleton is comprised of fourteen bones while the remaining 8 bones form the cranium. Besides the lower jaw, all other bones are strongly interconnected by synarthrodial joints

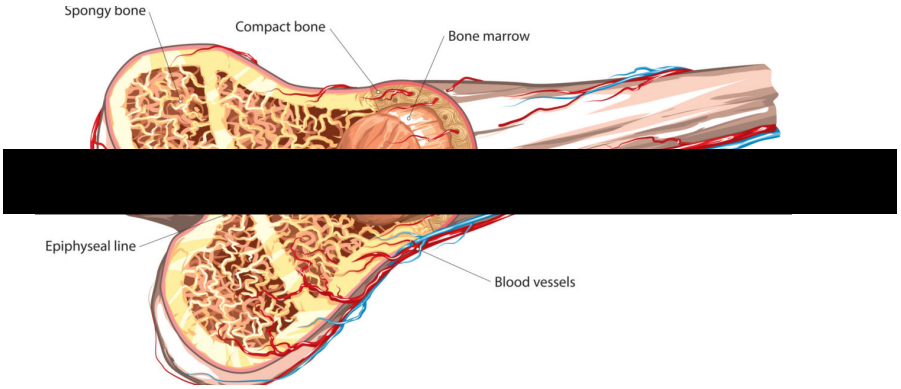

Figure 3.5: Bone anatomy: bone structure consist of many layers which are periosteum, cortical bone, trabecular bone and an inner core of bone marrow (image taken from [13])

.

named sutures. The lower jaw bone or the mandible is a movable bone and is connected to the cranium by flexible fibrous connective tissues, called ligaments. A group of cranial and facial bones together shape the eye orbit [64]. The cranium provides protection to the brain and most of the cranial bones are classified as flat bones. Figure 3.6 below shows that the cranial bones are layered bones where a less dense porous bone is sandwiched in between two relatively dense layers of compact bone. This middle layer is called Diploë while the other two hard bone layers are signified as the inner and outer tables of the skull [14].

3.5 The FLUKA Code

FLUKA is a general purpose fully integrated multi-particle Monte Carlo code for simulating physical particle transport and their interactions with matter. It is a Fortran90-based code which has many applications in high energy experimental and research physics, medical physics, radiobiology, shielding, detector, dosimetry and engineering. The National Institute for Nuclear Physics (INFN) in Italy and European Organisation for Nuclear Research (CERN) in Switzerland are two collaborators who have jointly participated in the development of this code since 1989. FLUKA is designed to precisely simulate the interactions and propagations in matters of about 60 particles, including hadron-hadron (up to 20 TeV), photons and electrons, neutrons and heavy ions. A detailed description about charged particles

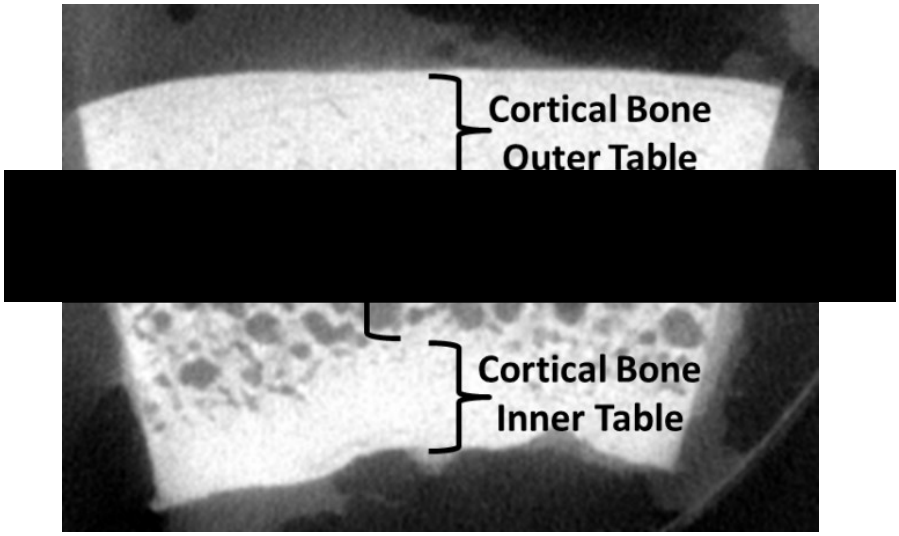

Figure 3.6: Figure elaborates the micro-CT image cross section of the frontal skull bone. Diploë is sandwiched between cortical bone layers [14].

transport and all applicable procedures is described briefly in [65].

The updated improvements in the algorithm for FLUKA nuclear models have increased its utilisation in medical physics, particularly for hadron therapy. FLUKA is the very first Monte Carlo Code which has ability to interpret the DICOM files into voxel geometry coupled with a combinatorial geometry package of the code [66–70]. The electromagnetic physics models have been developed and implemented in FLUKA to account for the continuous energy loss of heavily charged particles, range straggling, Coulomb scattering and delta ray production. The Bethe-Bloch formula with several corrections has been enforced to acquire the most accurate outcomes for requested therapeutic beam transport in FLUKA. For detailed descriptions about all physics models implemented in FLUKA see [66].

3.5.1 FLAIR - FLUKA Interface

FLAIR is an advanced user-friendly graphical interface [65, 66, 71] for the FLUKA Monte Carlo simulation code. It is based purely on Python and Tkinter (a graphical user interface). FLAIR provides a fully Integrated Development Environment (IDE) for FLUKA simulations, creation and checking of error free input files, debugging the geometry, monitoring the status of multiple runs, the execution and post processing of binary files and also a plot generating

interface (gnuplot) [66, 72]. In recent times new design of FLAIR is equipped with the feasibility to import, display, process and convert DICOM imaging files to FLUKA compatible voxel geometries. It also provides a tool for a treatment plan re-simulation and comparisons as well as for automatic PET scanners generation from user-provided parameters. The user can take advantage from series of commercially available templates for PET scanner within the interface. FLAIR permits importing the complete treatment scheme straight from the RT DICOM files such as a radiotherapy structure set (RTSTRUCT), radiotherapy treatment plan (RTPLAN) and radiotherapy dose distribution (RTDOSE). FLAIR integrates the basic characteristics of the beam delivery system and helps the user to put minimal effort to comply with the real irradiation setting.

3.6 Material and Methods

3.6.1 The Skull Bone Model

A plastic bone substitute (SAWBONES®) with structures, similar to that of bone trabeculae has been used to prepare the trabecular bone model for FLUKA simulation. SAWBONES® is a medical technology company famous for the production of bone and soft tissue models for research and clinical practice [73]. Raw micro-CT (µCT) images were taken for specified SAWBONES® sample which contained detailed information comparable to bone architecture. The honeycomb-like structures mimicking the trabecular bone can be seen in the plastic foam sample shown in figure 3.7.

3.6.2 MATLAB for CT-image Handling

For this project, the available CT images were in raw format which is not compatible with FLUKA. Therefore, the first important step was to post-process this raw data to a suitable configuration. Raw (µCT) images were exported into MATLAB where they were converted into a standard medical imaging format DICOM which is compatible with FLUKA-FLAIR. A detailed description of code can be seen in Appendix A. FLAIR is a graphical user interface program used to run the Monte Carlo simulations. The DICOM metadata is recorded in

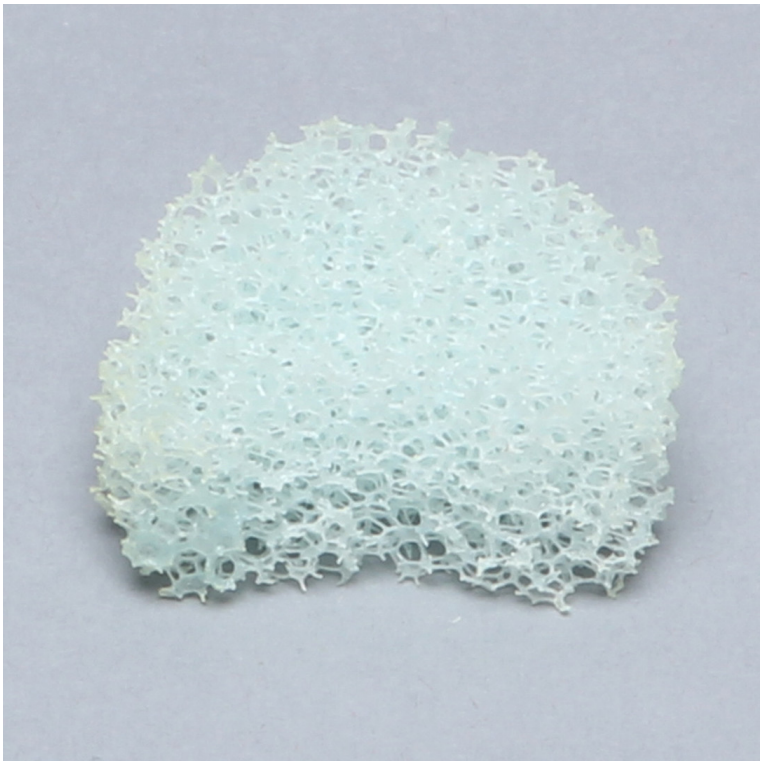

Figure 3.7: Sawbone® plastic bone sample bought from a SAWBONES® medical technology company (based in USA) responsible for production of bone samples for use in medical research and clinical practice is used for this project.

such a manner that it contains all the necessary information about scan set-up, details about the individual images and image as a set. Matadata includes an image series number, rows and columns in each image slice, width and height of each pixel, distance between the slices and slice thickness which are important for calculating the dimensions of the image series when loading them and employing these series as a three-dimensional body. In figure 3.8 (a) the rectangle (not to scale) represents the matrix dimensions (615 $\times$ 615$\times$ 696) which has been excised from the DICOM image series for bone modelling and it contains a uniform region of materials on it.

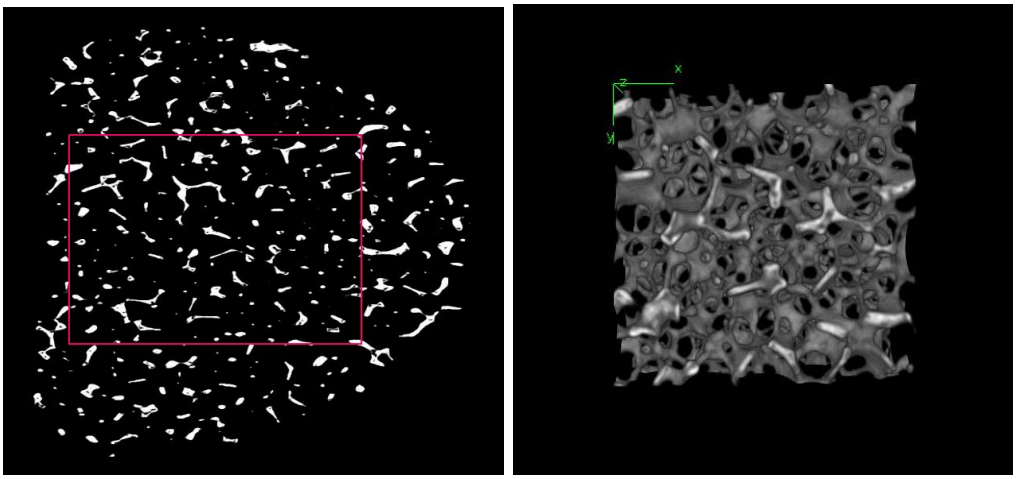

(a) 2D-view. *(b) 3D-view.*

Figure 3.8: MATLAB constructed 2D and 3D image views of a plastic bone substitute used for this project. The redlines representing the size of the main cube (not to the scale)excised from the most homogeneous part of the sample. In figure, (a) is 2D-view of a single DICOM image slice of a plastic bone substitute and (b) represents a 3D-view for whole image slices used for this project.

3.6.3 Conversion from Micro CT (µCT) numbers to Hounsfield Units

Computed tomography (CT) images play an important role for radiation therapy planning as they provide information about attenuation and scattering of radiation beams and help to delineate the tumor volume and normal tissues around the treatment volume [74]. A µCT image captures the actual trabecular bone architecture from which three-dimensional connectivity, trabecular thickness, trabecular number and trabecular spacing can be obtained. As these CT images are acquired for kilo voltage (KV) x-rays therefore, the images do not provide direct information about radiological properties relevant to the beam quality such as high energy photons, heavy ions and protons, which have been used in radiation therapy. Consequently, a precise conversion from CT numbers to their electron densities is most important for an accurate proton dose delivery [75]. The µCT numbers are directly related to the x-ray attenuation coefficient of the material [76]. Therefore, linear transformation has been used to convert these CT numbers on the bone images to their relevant Hounsfield

units (HU).

$$HU = [(Grayvalue \times slope) + intercept] \tag{3.1}$$

Usually the numerical values for the slope and intercept are attained from the image header files which are automatically generated for DICOM images. However, for this project the raw images were not provided with any such information; Therefore, the equations of line have been used to get the necessary information (slope and intercept) required for runnning the Monte Carlo simulations.

$$Y_1 = mx_1 + c \tag{3.2}$$

$$Y_2 = mx_2 + c \tag{3.3}$$

where,

$Y_1 = 3000$ (Hounsfield unit for cortical bone)

$Y_2 = 0$ (HU for water), $x_1 = 61156$ (maximum pixel value (µCT number) obtained from the given bone image) and $x_2 = 5000$ (is the minimum pixel value for the given bone material)

Manually calculated values for the slope and intercept were used in the above equation (3.1) and this relation is employed to the series of image slices to convert µCT numbers to their corresponding Hounsfield units. These bone images are now ready for use in FLUKA to design a skull flat bone model.

3.6.4 Skull Bone Modelling for FLUKA

Based on information about skull bone thickness extracted from the literature, a skull bone phantom is prepared which represents real bone dimensions. The average measured skull bone thickness for females is 7.1 mm while for men this value is 6.5 mm [77]. All available DICOM images were representative of spongy bone. An accurate knowledge about each layer is attained from a publication by E. M. Lillie et al. [14] which says that the physically measured average thickness for the isolated outer layer of the skull bone is 2.4 ± 0.8 mm. Figure 3.9 shows a female skull phantom that has been designed for this project. A 2.3 mm thick layer of trabecular bone is sandwiched between two outer cortical bone layers, each one of them is 2.4 mm thick.

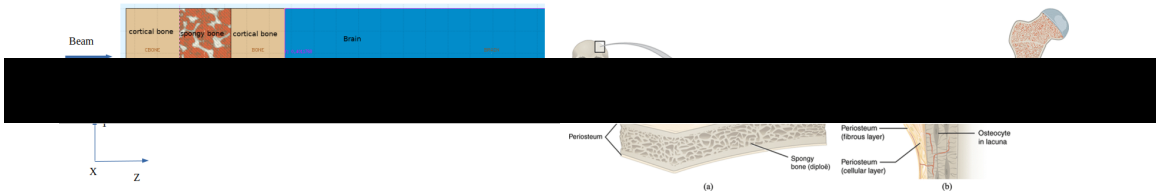

(a) Female skull phantom. *(b) Skull bone anatomy.*

Figure 3.9: A Skull bone phantom designed in FLUKA. Figure (a) is a screen shot for phantom geometry taken from FLUKA-FLAIR which represents the female skull model, and (b) is a presentation of skull bone anatomy (taken from publication [15]).

3.6.5 FLUKA for Monte Carlo Simulations

FLAIR is capable to process the DICOM files with the use of the pydicom module and eligible to convert them into FLUKA VOXEL or USRBIN compatible files. The FLUKA DICOM tab is used to load the CT images with an appropriate dataset to construct a body. The computed tomography images contain HU numbers and FLUKA combines a group of voxels with the same HU (or in a given HU interval material) in order to indicate it as an organ. This code handles each organ as a combinatorial geometry (CG) region in addition to other pre-defined non voxel regions. The FLUKA/FLAIR (when handling the voxel geometry) automatically generates a rectangular parallelepiped (RPP) based on the vxl file information. The vxl file contains all voxels inside. It is highly recommended to surround the RPP by a void region in order to escape unreliable boundary crossing anomalies. The origin of the beam is placed within the void region.

A blackhole region (bounding the vacuum) is suggested to surround the void region which has ability to catch all particles leaving the geometry. For this project the blackhole region is a sphere of radius r = 1×10^{6} cm while the void region sits within this volume having a radius r = 1×10^{4} cm. The FLUKA input file is prepared as an ordinary input file and the geometry is written like a normal CG input. In addition to that a VOXELS card is inserted right after the GEOBEGIN card and before the Geometry title card in the FLUKA input file as can be seen in figure 3.11.

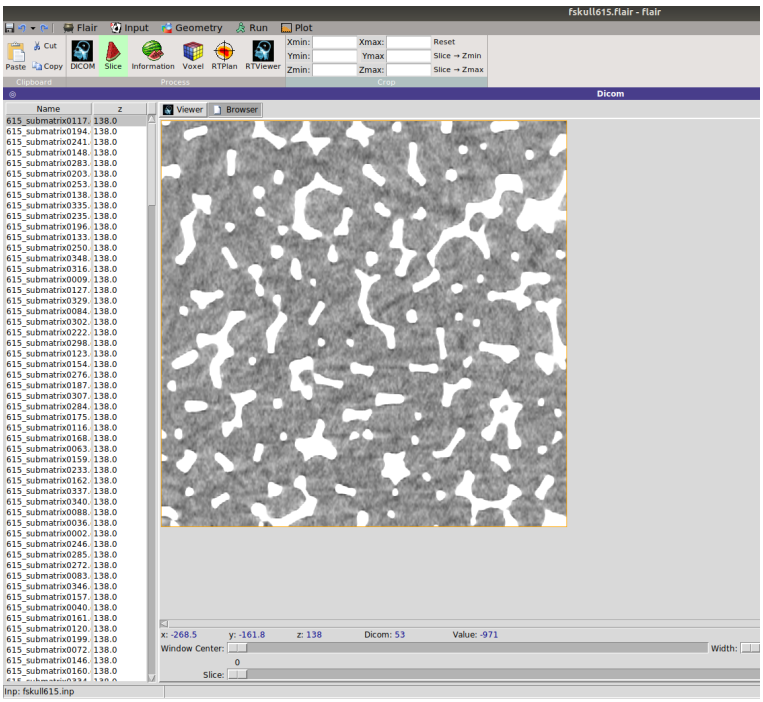

Figure 3.10: A screen capture for DICOM-FLAIR input file which gives us information about a series of z-slices used to model the skull phantom

.

3.6.6 DICOM Image Processing for FLAIR

The main purpose of this project is to record changes in the range of proton beam traversing the skull bone with respect to variations in the trabecular bone pore size. The individual voxel size is varied with MATLAB processing to make the bone more or less porous (larger the voxel size, bigger the pore and vice versa). Modifications in voxel size also results in variation for slice thickness in each image series. Therefore, the number of slices required to construct the skull bone model are also different in each case. Random sampling of the region taken from the bone substitute was employed to obtain the statistical variation in the texture and six different sets of matrices (each with individual dimensions) were excised from the main image matrix. Dimensions of these matrices are $615 \times 615 \times 353$, $369 \times 369 \times 212$, $246 \times 246 \times 141$, $123 \times 123 \times 71$, $90 \times 90 \times 52$ and $62 \times 62 \times 36$. The voxel size for each set of sub-matrices is changed to make a structural change in trabeculae of the bone.

A set of required number of slices is placed in each directory having the FLUKA in-

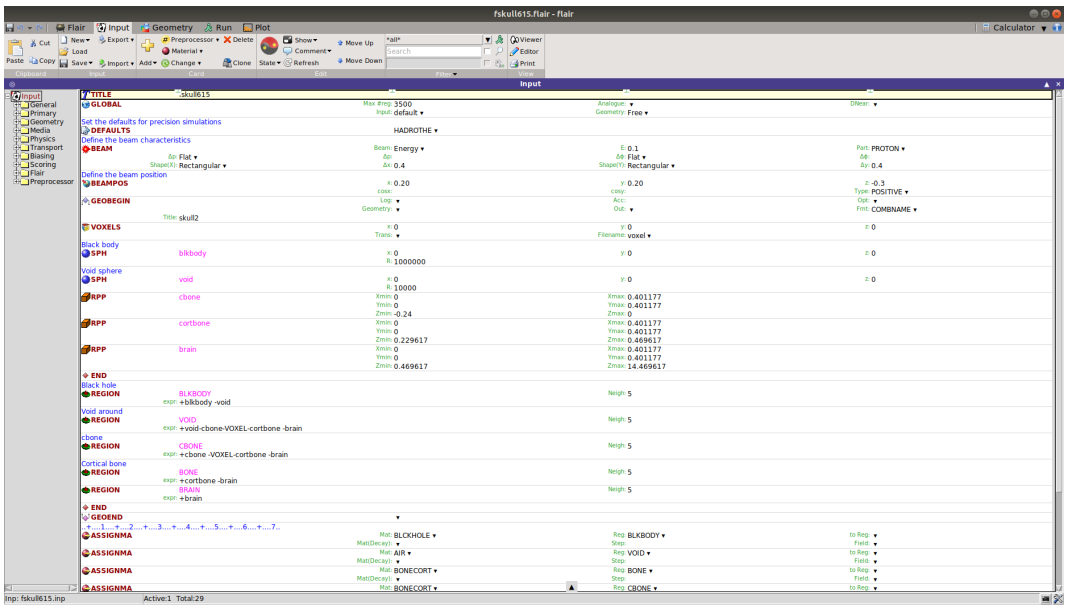

Figure 3.11: A screen capture for FALIR input which contains information about basic cards used to prepare analytical skull bone model for this work

.

put and FLAIR files; the DICOM tab is used to compile the images into a dataset. After adding a materials file, the parallelepiped voxel can be generated and saved in the folder. For FLUKA-FLAIR two additional files "material.inp" and "head.mat" are required to be in the same directory which contains FLUKA input file. The head.mat file contain conversion ramp which is required by FLAIR to map DICOM files for creating the relevant .vxl file. After inserting the head.mat and material.inp file, FLAIR automatically generates the .vxl file which is inserted into the VOXELS card. Organs and voxel region numbers are lodged into the .vxl file. The material.inp comes with the standard FLAIR distribution and contains the MATERIAL and COMPOUND card. For this work the "headfinal.mat" and the "matfinal.inp" have been customisd to create a .vxl file. The Hounsfield unit intervals for the bone materials can be seen in the table 3.1.

At microscale level a single trabecula ranging from tens to hundreds micrometres, represents trabecular bone tissue [78]. Based on this information, the trabecular bone is modelled with different pore sizes varying from 0.4 mm to 4 mm as shown in figure 3.12.The overall bone thickness is kept constant for all these cases by making a selection of sensible number

HU Minimum	HU Maximum	Tissue type
-1020	-1020	Air
7	300	Soft tissues, bone marrow
300	700	Cancellous bone
700	3070	Dense bone

Table 3.1: HU intervals for different materials in human body(information is extracted from the article [19])

.

of slices. The phantom geometry is also kept constant in the X, Y and Z directions for all six

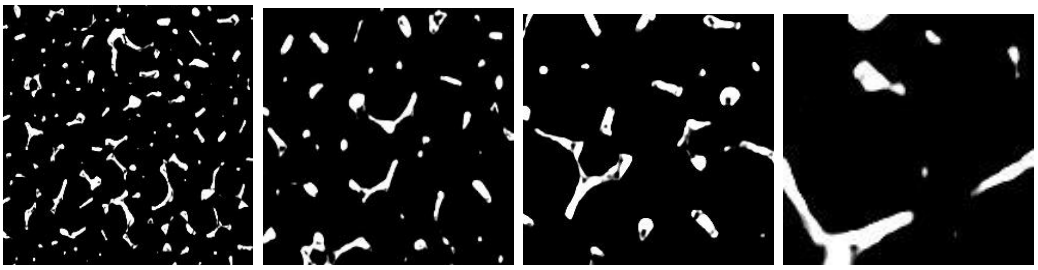

(a) 0.4mm *(b) 0.6mm* *(c) 1mm* *(d) 2mm*

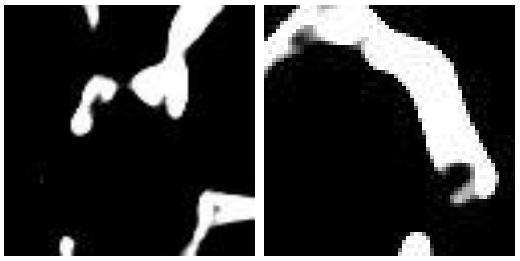

(e) 2.8mm *(f) 4mm*

Figure 3.12: A screenshot for six(a-f) CT image slices with different voxel values (to represent pore size) and same dimensions cropped from the main trabecular bone image.

cases, all x,y and z coordinates for RPP can be seen from table 3.2. The RPP (Rectangular Parallelepiped) represent phantom geometry for cortical bone, spongy bone and brain. A 100 MeV proton beam position is defined to make sure that it covers almost all the width of the phantom which starts at 0.3 cm, travels in the positive Z-direction and is rectangular (0.4×0.4 mm) in shape. Figure 3.13 demonstrates the beam specifications for this project.

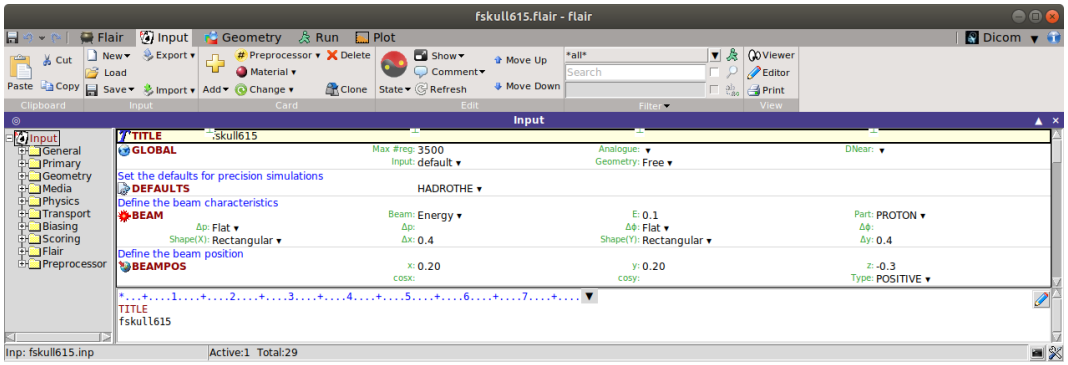

Figure 3.13: FLUKA-FLAIR beam information.

Directly in front of beam there is a 2.4 mm thick layer of cortical bone after which the beam penetrates through a 2.3 mm heterogeneous layer of trabecular bone and another 2.4 mm cortical bone. The setup demonstrates the flat skull bone anatomy. After passing through the skull beam enters into the brain that has been modeled as a blackhole catching all particles leaving the second cortical layer. It is important to deposit residual energy in the brain so that it becomes the measure of additional range for the proton beam after it traversed through the bone. This choice also makes it easy to calculate the amount of energy deposited in the bone. Simulations are run for maximum number of 5,000 primary histories for each cycle (i.e. $5000 \times 5 = 25000$ histories) at this instance. As protons interact in every they pass through so statistics are better than 1 % i.e. (1 s.d.) (1/sqrt(25000). These were sampled 5 times giving significantly larger variance. It was felt that the default number of histories was satisfactory for the test of the hypothesis that skull bones lead to clinically non significant changes in range. It takes about 15 minutes for 5 cycles to be completed.

Body	X-minimum (cm)	X-maximum (cm)	Y-minimum (cm)	Y-maximum (cm)	Z-minimum (cm)	Z-maximum (cm)
Cortical Bone	0.0	0.40117	0.0	0.40117	-0.24	0
Voxels/spongy bone	0.0	0.40117	0.0	0.40117	0.0	0.231791
Cortical Bone	0.0	0.40117	0.0	0.40117	0.231791	0.471791
Brain	0.0	0.40117	0.0	0.40117	0.471791	14.471791

Table 3.2: Values for x,y and z-coordinates for all the geometric bodies used to construct bone phantom

.

3.7 Results and Discussion

The mean energy deposited in the brain is taken from FLAIR output is tabulated for each simulation. All other information that has been used to manipulate the range shift can also be seen in table 3.3. As the loss of energy due to inelastic Coulomb interactions is helpful to ascertain the range in patient's body [2] therefore, the energy deposited in the brain (94 MeV) out of 100 MeV gives the information about the range of proton in the bone which is determined by using the following stopping power formula.

$$Rangechange\,(cm) = (94 - energy)/6.5/1.85/(meandensity + 1000) \times 1250 \times 10 \quad (3.4)$$

whereas, 6.5 MeVcm^2/g is total stopping power for 100 MeV proton beam in the ICRP cortical bone (taken from NIST PSTAR data base). The density of cortical bone is 1.85 g/cm^3. The mean density refers to the mean calculated HU value for each specific set of slices plus a 1000 (HU) correction factor. Column 6 of table 3.3 gives values (in mm) for the pore size. The author has modeled different pore sizes ranging from 0.4 mm to 4 mm to see if there were any variations in the range of proton beam versus changes in the pore size of the bone.

A scatter plot for variations in the range of proton beam vs changes in the pore size of trabecular bone is shown in figure 3.14. The range points on the graph are quite dispersed. The dispersion of the points for each set of the pore size is due to the Monte Carlo statistics and due to small differences in the type of the material. The hypothesis was to get a very narrow range over a broad distribution of pore size. This study indicates that a very large change in the pore size has a very small effect on the range of protons passing through the trabecular bone. The R^2 value on the graph shows that only 7.5% of variation is expected due to a change in the pore size. Changes in the range for this specific case are not clinically significant and support the normal practice for treatment through a flat skull bone. The density of the trabecular bone is almost kept constant for all sets of the FLUKA run. The following expression has been used to keep the overall density constant for each specific set of slices.

pixel values $\times$ No. of voxels = constant

or

N0. of Voxels x Pixel value	Energy deposited in brain (MeV) Output FLUKA	No. of slices	Mean density	Pixel value	Pore size(mm)	Range shift(mm)
615x0.0065232	89.3081	353	242.232	615	0.403252033	3.926136241
369x0.010872	89.4167	212	237.6512	369	0.672086721	3.849530146
369x0.010872	89.2166	212	231.0371	369	0.672086721	4.039144292
369x0.010872	89.5288	212	234.3487	369	0.672086721	4.081980517
369x0.010872	89.2339	212	254.8762	369	0.672086721	3.948120817
369x0.010872	89.2605	212	249.6358	369	0.672086721	3.942501346
246x0.016308	89.3328	141	252.9865	246	1.008130081	3.871968914
246x0.016308	89.1893	141	249.9185	246	1.008130081	4.000768429
246x0.016308	89.4229	141	268.0922	246	1.008130081	3.752029754
246x0.016308	89.1983	141	235.7626	246	1.008130081	4.039066719
246x0.016308	89.3556	141	270.8122	246	1.008130081	3.799024257
123x0.032616	89.4272	71	224.7759	123	2.016260163	3.881041189
123x0.032616	89.2257	71	277.5165	123	2.016260163	3.884794174
123x0.032616	89.2312	71	287.8081	123	2.016260163	3.84932651
123x0.032616	89.2643	71	246.5921	123	2.016260163	3.948942408
123x0.032616	89.3306	71	254.4091	123	2.016260163	3.869418932
90x0.0445752	89.2822	52	255.2295	90	2.755555556	3.906969735
90x0.0445752	89.3912	52	228.5209	90	2.755555556	3.899734924
90x0.0445752	89.0386	52	232.2666	90	2.755555556	4.185246506
90x0.0445752	89.2949	52	207.7724	90	2.755555556	4.049508008
90x0.0445752	89.1135	52	246.0552	90	2.755555556	4.076503072
62x0.064706	89.1808	36	261.919	62	4	3.969772608
62x0.064706	89.1104	36	246.6185	62	4	4.077192337
62x0.064706	89.2327	36	216.1285	62	4	4.074872723
62x0.064706	89.4188	36	225.9195	62	4	3.88454308
62x0.064706	89.4454	36	196.0802	62	4	3.958309897

Table 3.3: Results for variations in the 100 MeV proton beam range vs pore size (ranging from 0.4 mm to 4 mm).

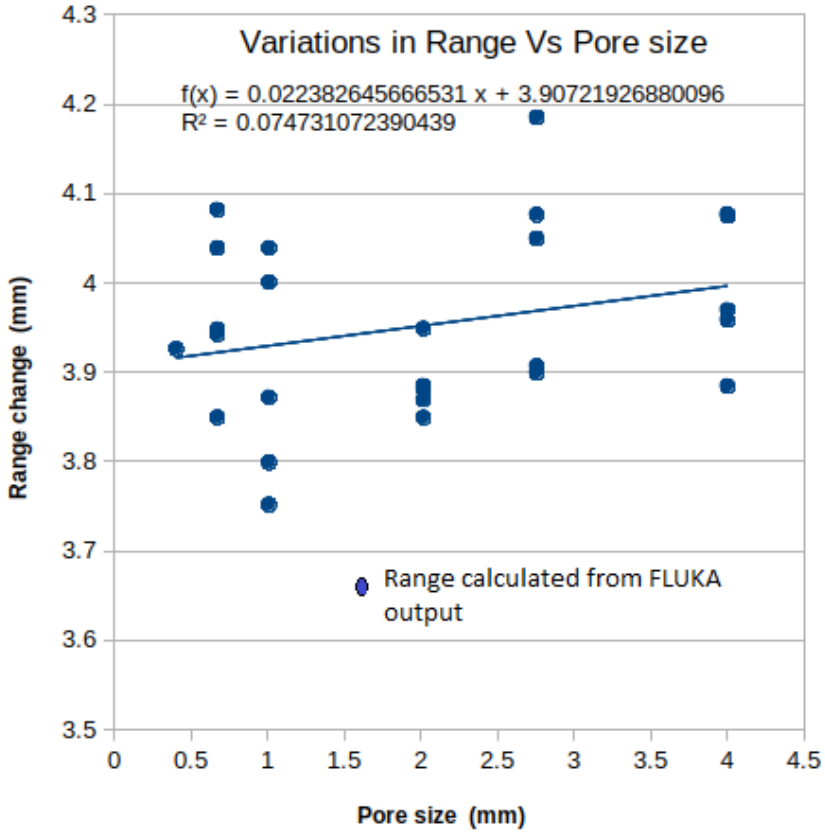

Figure 3.14: Graphical representation of change in the range of proton beam introduced by the trabecular component vs variations in the pore size. Here we can see five data sets for each pore size except for 0.4 mm. As mentioned in section 3.2 that random sampling of the region was taken from the bone substitute and employed to obtain the statistical variations in the texture. Five datasets represents each sample taken from a certain region of the main CT image. For 0.4 mm pore there is only one data set as for this size (615 × 615) random sampling was not possible.

slice thickness × No. of voxels = constant

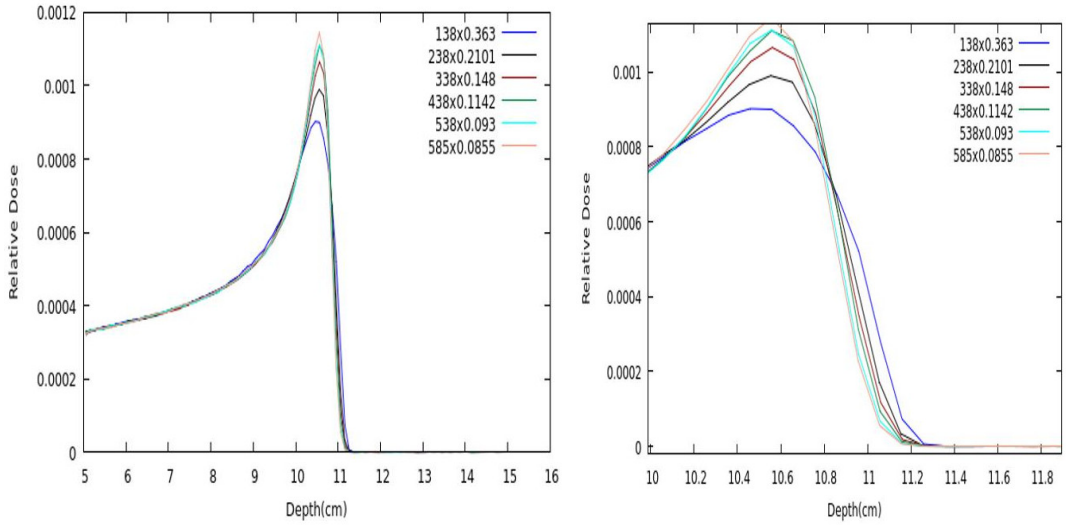

Figure 3.15: Broadening of Bragg peak at the distal end due to the sub-structure's variations.

Moreover, this density variance has been controlled by sampling the bone matrices from different parts of the trabecular bone. Therefore, results shown above do not include the differences in density. This study also demonstrates that a change in the range is not due to a change in the density of the bone. This change depends only on the structure of bone. So, if the author consider only the structure of the trabecular bone, there does not appear to be a tendency for the change in the range of protons beam vs change in the pore size for a thin, flat skull bone at the position of d20. This work signifies only a small variation in the range as a function of the pore size. Figure 3.15 suggested that variations in size of sub-structures led to a broadening of the Bragg peak and extension of the proton range. The percentage depth dose shows the largest variations at d20.

3.8 Conclusions and Future Work

The trabecular bone is very thin in the flat part of the human skull. It is normal practice to deliver proton therapy through the flat skull bone as there have not been reported any issues of range uncertainties for the proton dose delivery through this part of the bone. The present

work demonstrated that there were no major problems found for the proton beam therapy in terms of scattering in the flat skull bone. This fact has not been previously reported in the literature; therefore these outcomes support the normal proton therapy practice for treating through the thin flat bone. Considering the results obtained so far, future studies will be aimed at understanding the influence of the trabecular bone thickness on proton therapy. To evaluate the influence of other factors, the author will consider the other parts of the body such as the lung for delivering proton therapy. As lung is the most complex body part with air and tissues interface, a large effect on a proton's beam range is expected to be seen for repeating the same set of calculations at air and tissue interfaces. In chapter 4, the physics models used for scattering will be explored to see whether there is support for the use of Monte Carlo (MC) study. More densely packed trabecular bones, where they occur in the body, should also be examined to see if the same methods could be used for a denser bone for which author have to create larger and complicated phantom models. Future studies will include an example treatment and CT, MRI of patient skull as there may be some possibility of looking at better characterisation of bone using MRI. By considering all these prospects, Mr Owen Thomas Williams (an MSc student at Swansea University) have used an MRI based technique knwon as Fine Structure Analysis or ***fine***SA™in order to determine shift in the Bragg peak width and position occurs at energies of 200 MeV for a range of pore sizes, bone lengths and densities [79].

3.9 Summary

For precise treatment outcomes in terms of sparing the normal tissues and treating the tumor volume only, it is essential to have accurate knowledge about the range of the proton beam in tissue. Current work demonstrates little variations in the average range of the proton beam when it penetrates through the thin part of the skull bone. The d20 was shown to increase by 2 mm. However, these variations are not clinically significant and motivate the continuation of the practice of treating the brain tumor through thin part of the skull bone. The use of FLUKA code for this project, instigates the need for a Monte Carlo benchmark to verify the physical models for implementation of scattering accurately.

In the subsequent chapter measurements of a 36 MeV proton beam to assess the range uncertainties through thick bones of varying densities as a benchmark of the FLUKA code are presented.

Chapter 4

A Benchmark of the Effect of Sub-CT Resolution Inhomogeneities in Proton Radiotherapy

4.1 Aims and Objectives

The primary objective of this work is to quantify the range uncertainties associated with proton beams due to sub-CT resolution structures in the beam path when they penetrate through porous materials of variable densities. This project is designed to benchmark the similarity between experimental results and simulation data from Monte Carlo. To do this, a FLUKA code has been written to simulate an experiment performed at the Birmingham University proton beam line. In this way, experimental validation of the effects of sub-CT inhomogeneities in a bone substitute material predicted in chapter 3 with Monte Carlo modeling will be achieved.

4.2 Bone Substitute Foam Samples

SAWBONES® is a medical technology company that constructs customised bone and soft tissue models. One of their products is a series of cell blocks (foams) designed to imitate the trabecular bone. This open cell polyurethane foam has a cell size that is closer to a

human cancellous bone used in medical research [73]. Five different bone blocks of densities varying from 0.09 to 0.48 g/cc were chosen for this project. According to SAWBONES® literature, the blocks can be categorised in terms of two values; density or volume fraction, the latter of which can be defined as the ratio of block material to the volume of the block. Due to SAWBONES® operating within the United States each block is designed with density values of pounds per cubic ft (lb/ft^3) in mind, but this report will use density values in units of g/cc and differentiate the blocks by their respective catalogue numbers. Sections of SAWBONES® samples were cut into radiation-equivalent thicknesses (areal density), equivalent to 4 mm of water. Table 4.1 gives information about the foam densities and the water equivalent thickness of them. Figure 4.1 shows these bone samples cut into equivalent areal density, used to perform the experiment.

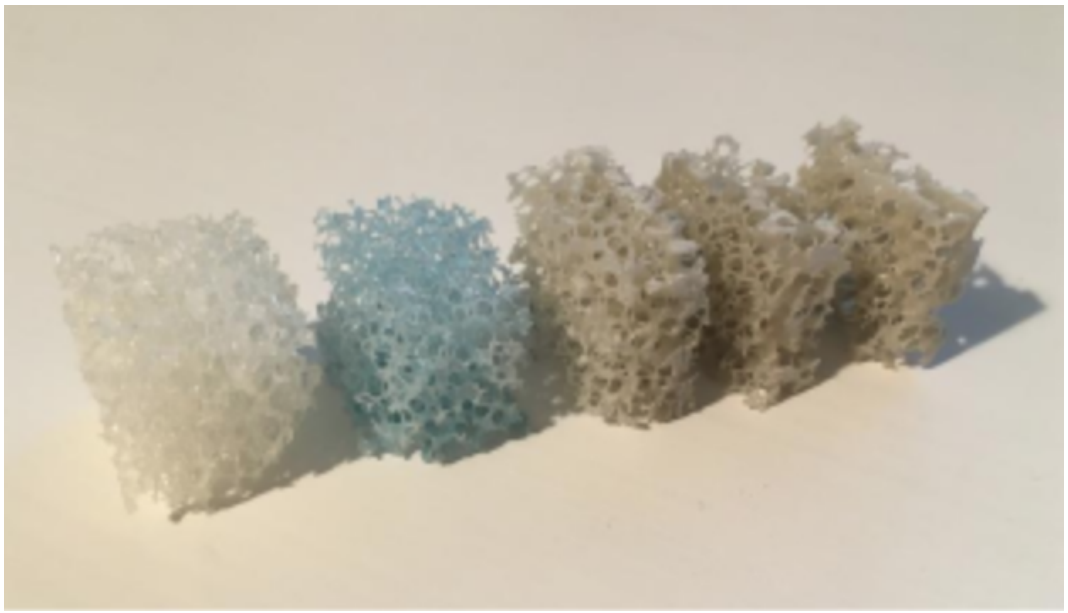

Figure 4.1: SAWBONES® samples (from right to left) in order of increasing density cut into 0.4 cm water equivalent equivalent thickness.

Foam product codes	Percentage of water equivalent density	Foam densities (g/cm^3)	0.4 cm water equivalent thickness (cm)
1522-505	8.8	0.09	4.44
1522-507	12	0.12	3.33
1522-524	24	0.24	1.666
1522-526-1	32	0.32	1.25
1522-525	48	0.48	0.833

Table 4.1: SAWBONES® foam properties and 0.4 cm water equivalent thickness for each foam sample.

4.2.1 Gafchromic Film

Gafchromic is a brand name for a variety of radiochromic films produced by International Speciality Production (ISP, Wayne, NJ). Conventional radiographic film generally consist of clear polyester outer layers with one or two thinner, internal gelatin coated, active layers which suspend small radiation sensitive silver-halide crystals. The gelatin emulsion on the outer layers helps to keep film stable for carrying out radiation procedures effectively.

The present work is focused on the latest generation of EBT Gafchromic films, EBT3 which was first introduced in 2012 at a commercial level. The EBT3 films are upgraded, unlike EBT2, the EBT3 films have a microscopic silica particle coating which helps to minimise the Newton's ring patterns on the film during image acquisition. The atomic composition of EBT3 film is tissue equivalent and it can be dunked into water without any damage. These films are one of the most promising dosimeters for accurate and precise two-dimensional dosimetry with a high spatial resolution, better than 0.1 mm. Furthermore, these films does not require post-exposure physical or chemical developing. These films are available in two sizes: EBT3 - $8" \times 10"$ boxed in packages of 25 sheets and EBT3 - $1417 - 14" \times 17"$ boxed in packages of 10 sheets.

Gafchromic EBT3 films consist of an active layer (total thickness 27 µm), embedded between two identical polyethylene terephthalate (PET) based (each one of thickness 125 µm) plastic layers. The atomic composition of the film is shown in the following table 4.2.

After irradiation, the active layer of the EBT3 film gets polymerised which results in darkening of the film. The degree of darkness can be measured in terms of optical density (OD) of the film. For any kind of film dosimetry, it is always important to know that the

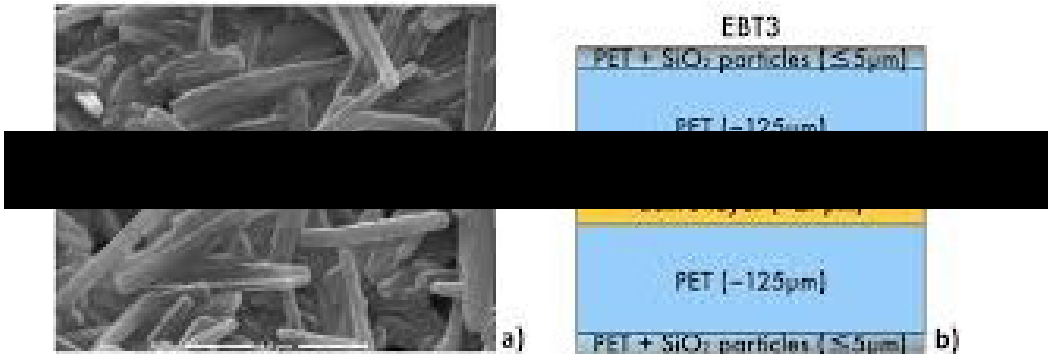

Figure 4.2: (a) Microscopic view of the active layer in EBT3 (b) Geometrical description of EBT3 film. Figure taken from Roberta Castriconi's thesis. [16]

EBT3	H	Li	C	N	O	Na	S	Cl
Act. Layer	58.2	0.8	29.2	0.1	10.7	0.1	0.1	0.9
PET	36.4	-	45.5	-	18.2	-	-	-
PET + SiO_2 where, PET = 99.986	-	-	-	-	-	-	-	-
and SiO_2 = 0.014	-	-	-	-	-	-	-	-

Table 4.2: Material composition of EBT3 films (percentage by atom) [16].

optical density is equivalent to the dose absorbed by the film. The optical density of a scanned film can be characterised as :

$$OD = \log_{10}\left(I_0/I_{\text{film}}\right), \tag{4.1}$$

where I_0 is the intensity of light with no film and I_{film} is the intensity of the light which passes through the film. It is practically recommended to scan a film before any exposure to it. It will help to obtain the background OD which will then be subtracted from the total optical density acquired after the film exposure, in order to relate the net optical density to dose [80].

4.3 Materials and Methods (Experiment)

4.3.1 Experiment Part-1

This experiment has been performed in two attempts in order to determine the same objective. Some discrepancies were found in the final results (from film analysis) of the first trial which have suggested a few improvements to achieve the goals. A detailed description of the second experiment is described in section 4.4 ; comprehensive information about the first experiment is given here.

4.3.2 Overview of Experiment-1

A team of three people, Dr Richard Hugtenburg, Jordan Pritchard and Sumaira Nazir of Swansea University partnered with Dr Tony Price of Birmingham University to use the proton beam line at Birmingham in an experiment on a series of heterogeneous foam phantoms.

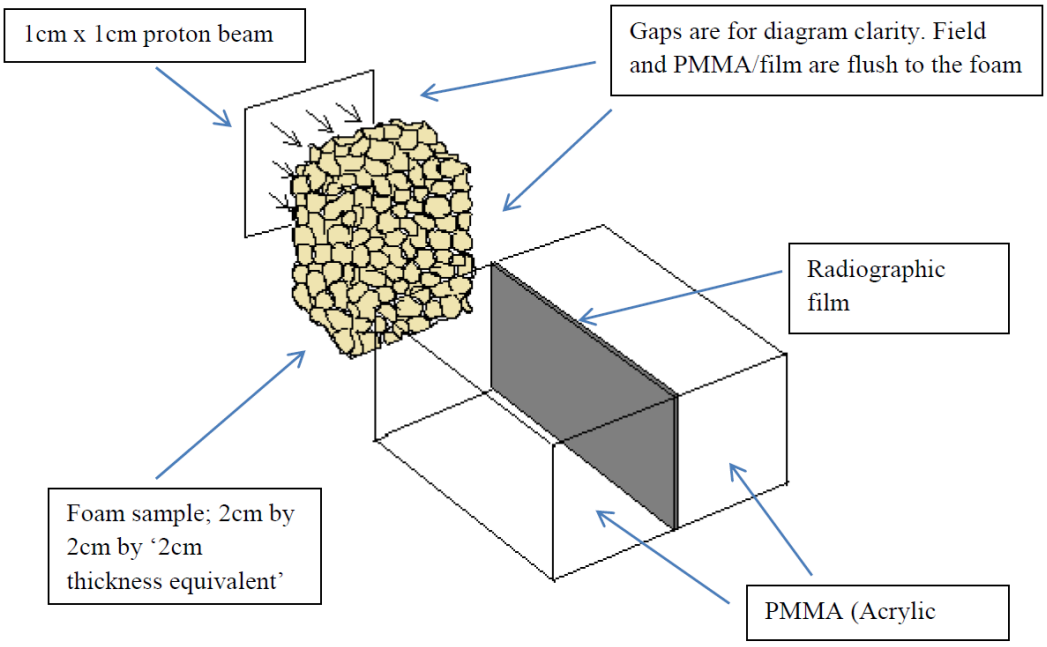

Figure 4.3: A sketch of the setup used to perform experiment at Birmingham University beamline.

The five foam samples (as shown in fig 4.1) having different densities and pore size

were taken to designed trabecular bone and lung tissue models. The proton beam line at Birmingham University was used to generate a 28 MeV 1 cm $\times$ 1 cm proton beam field. Figure 4.3 is drwan to explain the experimental arrangements. The foam samples were placed directly in front of the beam individually. The radiographic film was placed perpendicular to the foam sample and clamped between two layers of PMMA (acrylic glass). Each sample was subjected to 30 minutes of 3 Gy of protons before being replaced along with the film. There was also a reading taken without a foam sample so as to produce the most pristine Bragg peak possible given the experimental set-up. The radiochromic film used was HD-V2 by Gafchromic. It has a HU number similar to tissue which is useful for modeling the lung and has a high spatial resolution (features down to $\approx 5\ \mu$).

The films were developed using a confocal microscope and computer processed by Paolo Pellicioli of Grenoble and Swansea Universities [81]. Figure 4.4 shows a developed film of a 'pristine' Bragg peak. On these images the proton path is downwards from the top and as expected, the Bragg peak is expected to be very consistent across the image. The brightness of the image indicates where the energy is being deposited and it can be seen that the majority is deposited at the bottom of the image which is consistent with the Bragg peak theory (mentioned in chapter 2)

4.3.3 Double Bragg Peak

It is also possible to see a second less visible Bragg peak located just above the main peak (see figure 4.4a). This Bragg peak could be caused by a number of factors but the most likely is that because the density of PMMA (1.18 g/ccm) is lower than the tissue equivalent film (approximately 1×10^{-4} g/ccm) there are additional protons entering from the edge of the PMMA. The protons from the PMMA will have a later peak because of the denser material they have travelled through and where it would be expected to see some (negligible amount) of protons from either material crossing over. The cross over will become more uni-directional due to the difference in densities. In Kimball-Smith's work [82] in order to explore this double peak (found on the pristine Bragg peak film from the original experiment) a simulation was run without a voxel with the film being assigned water and another identical simulation was also run but with the film being assigned PMMA. It is concluded that this

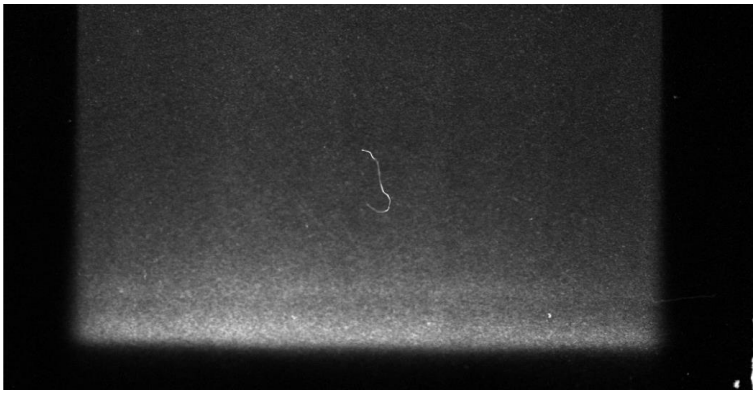

(a) Developed film without a foam sample (pristine peak).

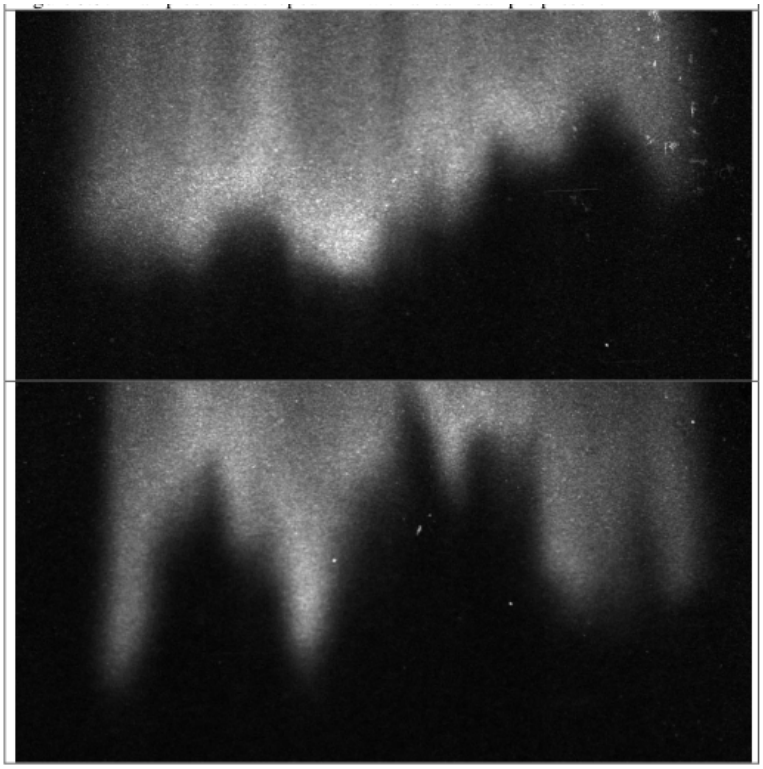

(b) Examples of developed film with a foam sample present

Figure 4.4: (a) is a developed film which was exposed to a proton beam without a foam sample to observe the pristine peak and (b) the examples of two different developed films with foam samples (of variable densities, top 0.09 g/cc and bottom 0.48 g/cc) present in the path of the beam.

is an error which cause a double peak due to the density difference. It is known that the density of HD-V2 is 1.4 g/ccm. Making PMMA a material of choice the densities will not change between the film and two blocks on both sides and thus it will eliminate a double

Bragg peak caused by density changes. Figure 4.6 justifies the formation of the double Bragg peaks due to a difference in densities of the material that the protons passes through.

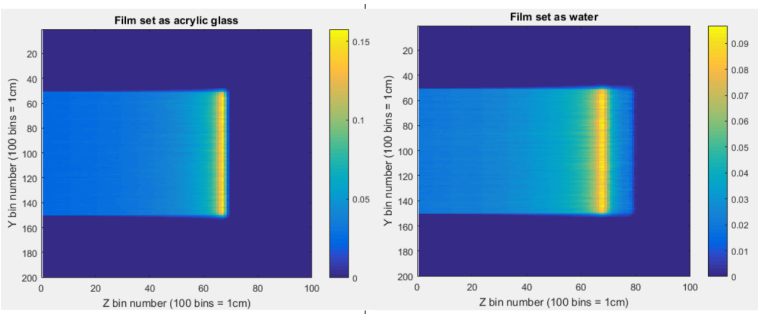

(a) FLUKA output desplaying energy intensity in the y and z planes.

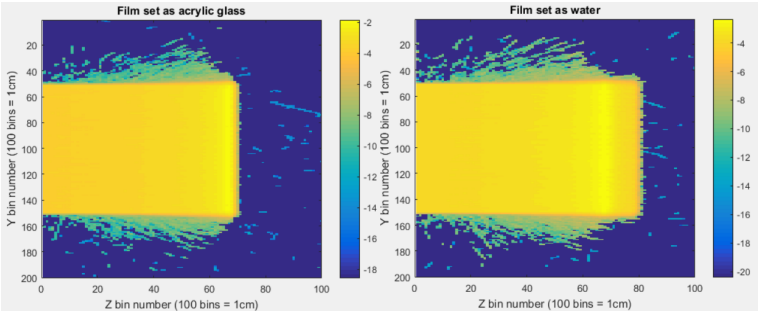

(b) Graphs to show the log of the energy deposited in the y and z planes.

Figure 4.5: FLUKA output to see the Bragg peak variations in both cases. (a) is the display of formation of Bragg peak ehrn the film is set as acrylic glass (right) and water (left). Similarly, (b)shows the enegry deposited in the film in both situations

.

A MATLAB code was written to post process the FLUKA output. The double Bragg peak distortion was avoided in these samples by keeping the film as PMMA in the simulation. The same effect would be seen by switching the PMMA with water (a container for water would be unnecessary for FLUKA).

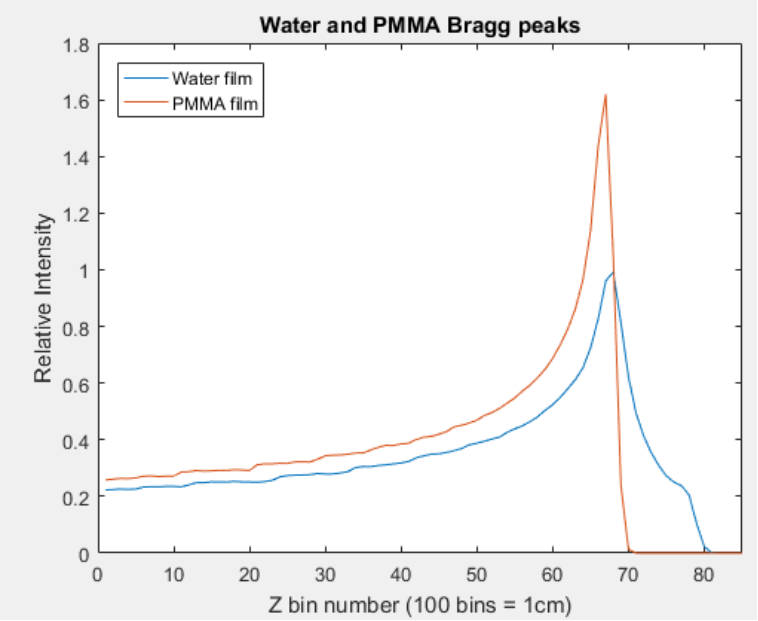

Figure 4.6: Graphical presentaion of the FLUKA output to show the 'pristine' Bragg peaks. Red graph shows the formation of the Bragg peak when the film is assigned as PMMA while blue graph shows the Bargg peaks when the film is used as water.
'materials' in FLUKA.

4.3.4 CT Image Manipulation

The DICOM images of all foam samples were manipulated using MATLAB code given in appendix C ; except the Hounsfield unit conversion. The bit depth refers to the maximum intensity of each pixel and this indirectly affects the Hounsfield unit of each pixel. These values were different between the data sets and therefore, needed to be changed. The Hounsfield unit conversion in Flair is in part calculated using a calibration curve following a $y = mx + c$ line where m equals the variable 'rescale gradient' (RescaleSlope in the code) and c is the 'rescale intercept'. The gradient is usually by default 1, however we want to calibrate the pixels so that the maximum intensity is equal to a solid pixel of foam and hence is equal to a Hounsfield unit of 0 (water equivalent). From the now working dataset, importing the dataset into Flair produced a minimum value of approximately -1000 and a maximum of -757. Using a rescale gradient of 4 this can be recalibrated to giving a HU number much closer to 0. The rescale intercept is set to -1000 in both sets to account for the HU scale starting at -1000. Pixel spacing, slice thickness, spacing between slices and slice location were altered to match. The spacing between slicing is stated as 0.0434 despite the slices being flush because it takes this value as the distance between the centres of successive slices. The slice location was calculated by using the current slice number and the distance between slices. UID numbers, which are unique identification numbers associated with each CT dataset, were changed as so differentiate between slices (the fixed metadata was based off of one file not a whole set). A new folder is created to contain the cropped file and function 'dicomwrite' is used to write the cropped images as new files with the associated altered metadata from the structure. These new files can now be read into Flair as DICOM files to create a VOXEL.

4.3.5 Monte Carlo Simulations

To simulate the experiment in Birmingham, a geometry similar to experimental set-up as shown in figure 4.3 was created in FLAIR. A rectangular 1×1 cm^2 proton beam of 28 MeV

was placed starting at the origin (see figure 4.7). Directly in front of the beam is either the foam sample or nothing (in the case of generating a pristine peak). Geometry is added by first creating geometrical shapes and assigning names to them and defining coordinate positions. Regions created can be just a shape or a combination of shapes and subtracted shapes. Finally, materials are assigned to these regions; for example, the void is just the air that fills everything in between objects. The materials used in original experiment are all available in the program including PMMA except for the foam. Therefore, all the HU numbers and material densities are automatically associated with a region when assigning them a material. The foam is not an exact region as the pixels are intensities. These intensities are associated with a degree of mixture of air and foam material where 0 intentisity represents air ($-1000HU$) and maximum intensity is the foam bulk material (a tissue-equivalent HU). Therefore, during creation of the foam voxel it is necessary to include a materials file which convert intensity ranges into HU numbers. Because there are only two materials, air and foam, the standard example (built-in materials file) does not need to be altered as the rescaled slope fits the data between -1000 and 0 HU. After adding the voxel as a loaded file shown in the figure 4.8, FLAIR automatically considers each intensity range as a region and assigns a HU to that region. The number of primary histories (400000) refers to individual protons. More particles increase the computation time but decrease errors and gives better statistics.

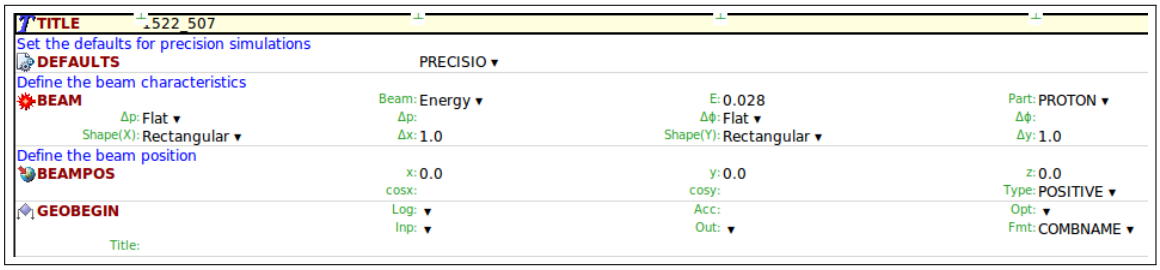

Figure 4.7: A screenshot of FLUKA-FLAIR input to display the beam information

.

For each FLUKA simulation requiring a voxel the cropped images are placed inside the same directory as the simulation file and the DICOM tab is used to compile these images into a dataset. After adding a materials file the voxel can be generated and saved in the

same folder. Following the voxel or air gap there are two regions of PMMA and a thin film in between. The film is approximately 100 microns thick as stated in the specification documents for HD-V2 film. The film centres on the x- plane and follows perpendicular to the y plane. The proton beam moves in the z-direction therefore, the film starts where the foam stops on the z-plane and ends 2 cm further, deep enough for the Bragg peak to appear.

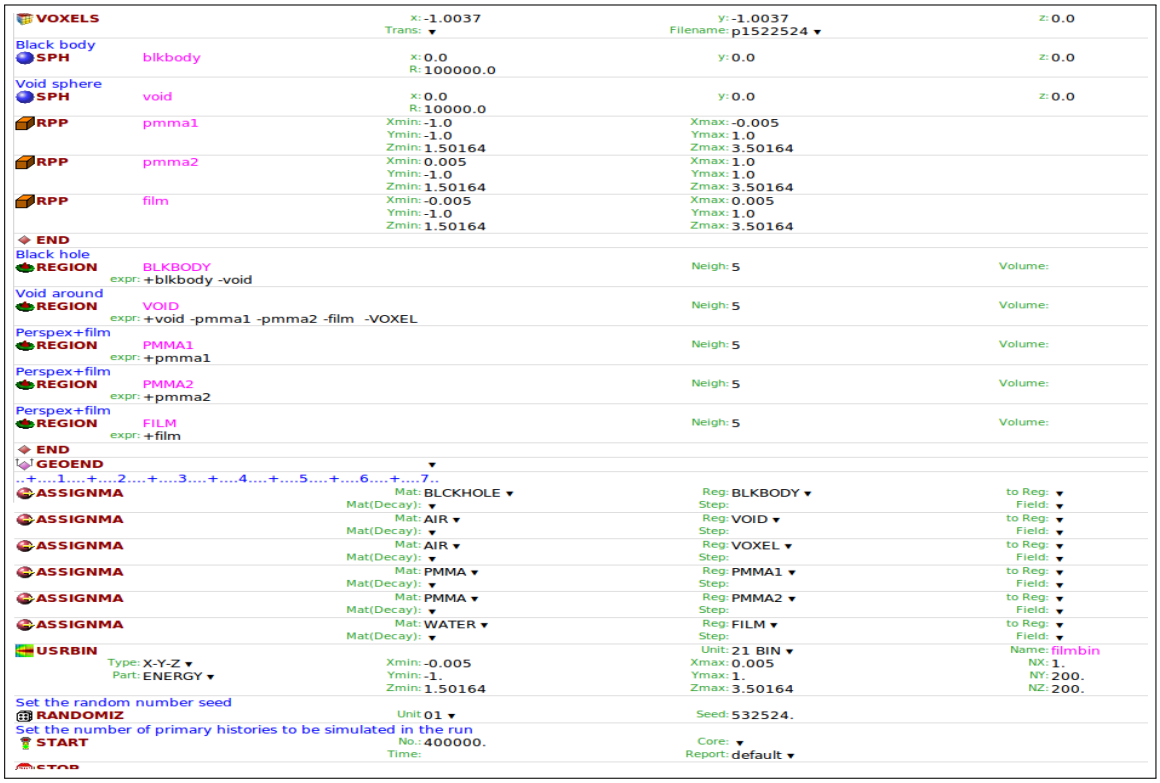

Figure 4.8: A screen cast of FLUKA-FALIR input file to represent the geometry information

.

The size of the film required to encapsulate the entire Bragg peak can be quickly tested by running the simulation on a large film over a short primary particles. Short simulations produce poor images with low resolution however, it is possible to observe where the limit of the proton paths is. The film is assigned water as its material to simulate the tissue equivalency (this was later found to be a significant error). The PMMA is made large enough to encompass the entire beam so that it all diminishes around the film and their is no contamination of the film from the edge of the beam moving through air. To record

data like a radiochromic film a 'USRBIN' is created to encompass the entire film region. By making the x direction one bin wide, but 200 in both the y and z planes. The USRBIN can score energy as a 2-D image again recording intensities into a 2-D matrix. Each simulation makes 5 runs hence every intensity value comes with an associated standard deviation. The bin can be exported into ASCII format and imported into MATLAB to be manipulated for graphing.

4.3.6 Analysis

For the radiochromic film used in experiment, a MATLAB script was written for locating the d20 location and Bragg peak along each pixel on the Z-axis by Dr Richard Hugtenburg. The d20 position is calculated by searching for the first zero and fitting a polynomial curve, using the function 'polyfit', between it and the Bragg peak value. The d20 is positioned at 20% of the distal falloff. The axis is cropped to exclude the sides of film not exposed directly to the beam. The code is modified to obtain results from the FLUKA output. It is a slightly easier task as there is little to no noise as the 'film'; the USRBIN, in the FLAIR input is a perfect detector.

```
pf      = zeros(length(PB),2);
[m,i]   = max(PB');
[mz,iz] = min(max(PB,750*ones(size(PB)))');

for k = 1:length(PB)

pf(k,:) = polyfit(1:(iz(k)-i(k)+1),PB(k,i(k):iz(k)),1);

end

%plot((i'-m'./pf(:,1)),'g')
%hold on; plot(i/10,'b')

% B =
reshape(sum(reshape(reshape(sum(reshape(mf_image_microscope(:,5:11104),kr,[
])),mk,[]).',kc,[])),nk,mk)'
```

Figure 4.9: MATLAB code to locate maximums in film dosimetry.

Because the distal falloff just hits zero and stays there the code does not have to search for the first zero, it just takes the position of the minimum value. The axis is again cropped,

between bins 40 and 160 to exclude the areas not exposed directly at the beam. The 'polyfit' function can create anomalous values in these regions as the values tend back towards zero; there is never going to be a polynomial that perfectly fits the graph. One of the constraints of polyfit is that the order of the polynomial cannot exceed the number of points.

The spread of the Bragg peak can be taken as the distance between the Bragg peak maximum and the d20 value. By finding the average over all of the z-direction pixel lines which encompass the path of the proton beam the different foams can be compared. The errors of this calculation is calculated using the standard deviation function. The MATLAB code given in Appendix E is used to calculate the z position of d20, to subtract the lower z position of the Bragg peak, find the mean and standard deviation. The results are tabulated in table 4.3 against the density of the sample. This can be taken as a zero density sample. The density is plotted against the mean distance between Bragg peak and d20 position.

Figure 4.10 shows that the graph plotted from FLUKA output is equivalent to that produced for the radiochromic film data, obtained in the original Birmingham experiment.

Sample	Density (g/ccm)	Mean distance between Bragg peak and d20 (mm)	Error (standard deviation (mm))
none (pristine)	0.0	3.2192	0.3633
1522-507	0.12	5.4543	1.3533
1522-524	0.24	12.0295	2.8985
1522-526	0.32	14.3073	5.7802

Table 4.3: Table of average distance between Bragg peak and d20 for pristine and 3 foam samples.

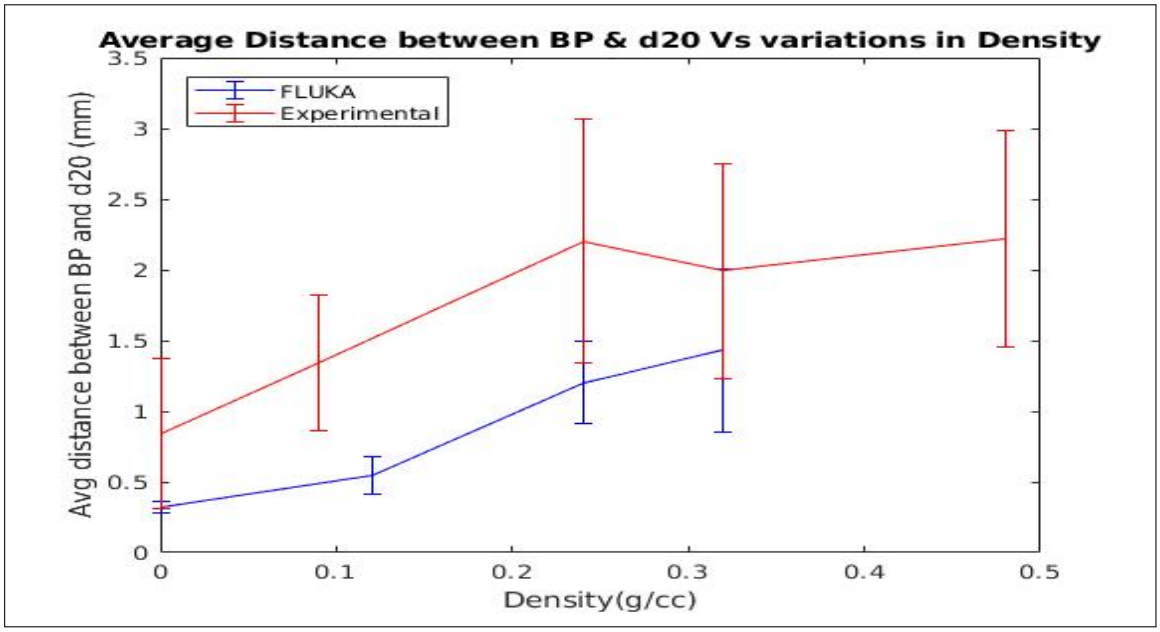

Figure 4.10: A graph to show the relationship between foam density and difference between the d20 of the distal falloff and the Bragg peak as a function of the foam density. Each bin is equivalent to 10 microns. Here it can be seen that the data points for beam simulation in highest density foam sample is missing. It is because the DICOM image file for bone sample 1522-525 was corrupted and there were no images available to construct an analytical model in FLUKA for simulation.

4.4 Experiment Part-2

4.4.1 Experimental Set-up

After investigating the most important characteristics of EBT3 such as response at high-dose levels, high spatial resolution and small energy dependence (for details see section 4.2.1), it has decided to utilise EBT3 to perform experiment. The EBT3 radiochromic films were purchased in a box of 25 sheets and few of them were cut into thirty pieces; each one of them was 2×2 cm^2 in area. A small arrow was drawn on each piece (see figure 4.11) to keep a track of orientation with respect to the original sheet. The proton beam line at Birmingham University was used to generate a 36 MeV (a higher energy than the previous experiment), 1×1 cm^2 field. The foam samples were then placed directly in front of the beam individually. As shown below in figure 4.12, the film was placed perpendicular to the foam sample and clamped between two equivalent density layers of polyethylene terephthalate (PET). The reason here for making PET a material of choice is that it has comparable density and chemical formulation to that of EBT3. Therefore, it helps to eliminate the possibility of double Bragg peaks which were seen in previous experiments, performed with PMMA (acrylic glass) blocks. For each one of the foam samples, the films were irradiated at three different positions (right, middle and left) of the bone substitute to get a better understanding of the degradation effect and to improve statistical sampling of the foam.

4.4.2 Radiochromic Film Calibration and Irradiation Procedures

The pieces of radiochromic film were individually clamped between two blocks of PET and irradiated to a 36 MeV radiation (1×1 cm^2) beam. At first 6 pieces of film were exposed at a dose level of 0.5, 1, 1.5, 2.0, 2.5 and 3 Gy to obtain the calibration curve.

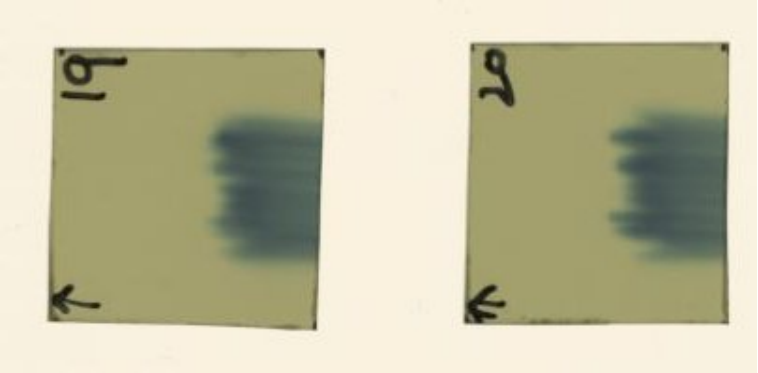

Figure 4.11: Figure displaying two pieces of film post-exposure. It can be seen that an arrow is drawn on each piece to keep a track of orientation with respect to the original film.

Figure 4.12: Experimental set-up used to measure variation in proton range due to variable bone structure and density. A piece of EBT3 film is placed perpendicular to the beam direction, clamped between pieces of PET block in front of the bone foam sample.

For an EBT3 readout the film pieces (with the same orientation) were placed at the centre of an Epson 11000XL Pro flat-bed scanner (available at Singleton Hospital). A cardboard template is used to ensure film position reproducibility. Films were scanned in the 48-bit colour mode with a spatial resolution of 720 d_{pi} corresponding to a pixel size of 0.0353 mm. The digital images thus obtained were saved in uncompressed tagged image file format (TIFF) and analysed with the help of MATLAB. A MATLAB script was written (as given in Appendix E.2) to readout the dose (intensity of the film) from all three (RGB) channels which are summed-up together and Bragg peaks were obtained from all irradiated films. The film intensity is taken as the sum of the amount of energy deposited at the entrance of the calibration films. Dose from measurements performed with a Markus Chamber were plotted against the film intensity. A third order polynomial gives an acceptable line of best fit between dose and the film intensity (measured from film darkening). A polynonmial function is designed to interpolate over a range of values that would not increase uncertainty in the relationship between film intensity and dose. Here third order polynomial gives a better fit than the second order polynomial and it actually interpolates between the data points that have been taken from the experiment.

Intensity of film(W/m^2)	Dose (Gy)
7.085e4	3.946
7.459e4	3.208
7.857e4	2.644
8.451e4	1.945
9.183e4	1.284
1.01e5	7.410
1.125e5	0

Table 4.4: Values of entrance dose measured from EBT3 irradiated films and Markus Chamber.

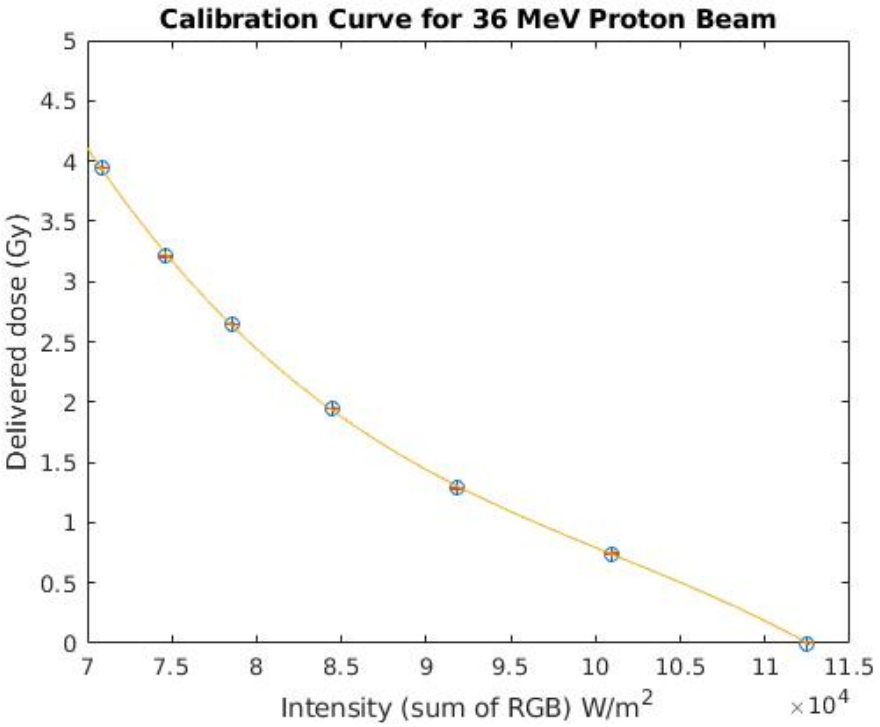

Figure 4.13: Calibration curve for dose measured with Markus Chamber vs dose measured from irradiated films. The uncertainty in the dose is much smaller (0.0026%, shown as vertical error-bars) and 5% is the uncertainty (horizontal error bars) in the film is applied to all measurement points. In practice it is probably less than this as the films were all from the same batch.

4.5 Film Analysis

The experimental films were scanned by following the same procedure as described in section 4.4.2. The calibration films were scanned together with the experimental films to keep the ambient temperature constant for both sets and it also helps to reduce the scan-to-scan differences between sessions. In all cases, the scans were performed two days after irradiation to allow post-exposure optical absorption to be stabilised [83]. A MATLAB code given in listing E.3 was written to automate the experimental film's analysis. The examples of developed films for different foam samples are shown in figure 4.14 . These heatmaps provide a great visual analysis of the films. However, for further analysis it is necessary to find the specific points at which there is a maximum, minimum, the d80 and d20 of the distal fall-off. By graphing and comparing these quantities, the difference between the samples of varying

density are examined. This MATLAB code determines the location of each Bragg peak along each line of pixels from the top to the bottom line in figure 4.14 .

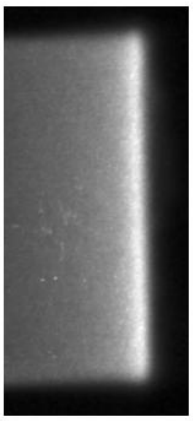

(a) Bragg peak with no foam

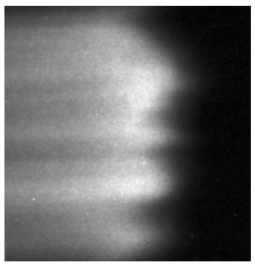

(b) 1522-505 (0.09 g/cm^3)

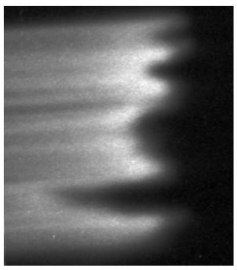

(c) 1522-524 (0.24 g/cm^3)

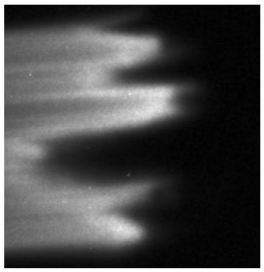

(d) 1522-526-1 (0.32 g/cm^3)

Figure 4.14: Examples of developed films; (a) is a film for Bragg peak with no foam in the beam path and others were exposed to radiations with different densities foam samples present in the path of a 36 MeV proton beam.

Figure 4.15 shows variation in the Bragg peak between the four samples. The red line corresponds to the Bragg peak position, the blue lines are the d20 while the magenta lines represent the d80 position. The d20 location is calculated by searching for the first minimum and fitting a polynomial curve, using the function 'polyfit', between this position and the Bragg peak value. The spread of the Bragg peak is taken as the distance between the Bragg peak maximum and the d20 value. By finding the average over all of the z-direction, pixel

lines which encompasses the path of the proton beam in the different foams, can be compared. The errors are calculated using the standard deviation function. The code in listing E.3 is used to calculate the z position of d20 and subtract the lower z position of the Bragg peak and to find the mean and standard deviation. Similarly, the z position of d80 is calculated and the mean and standard deviation is calculated for d80 location.

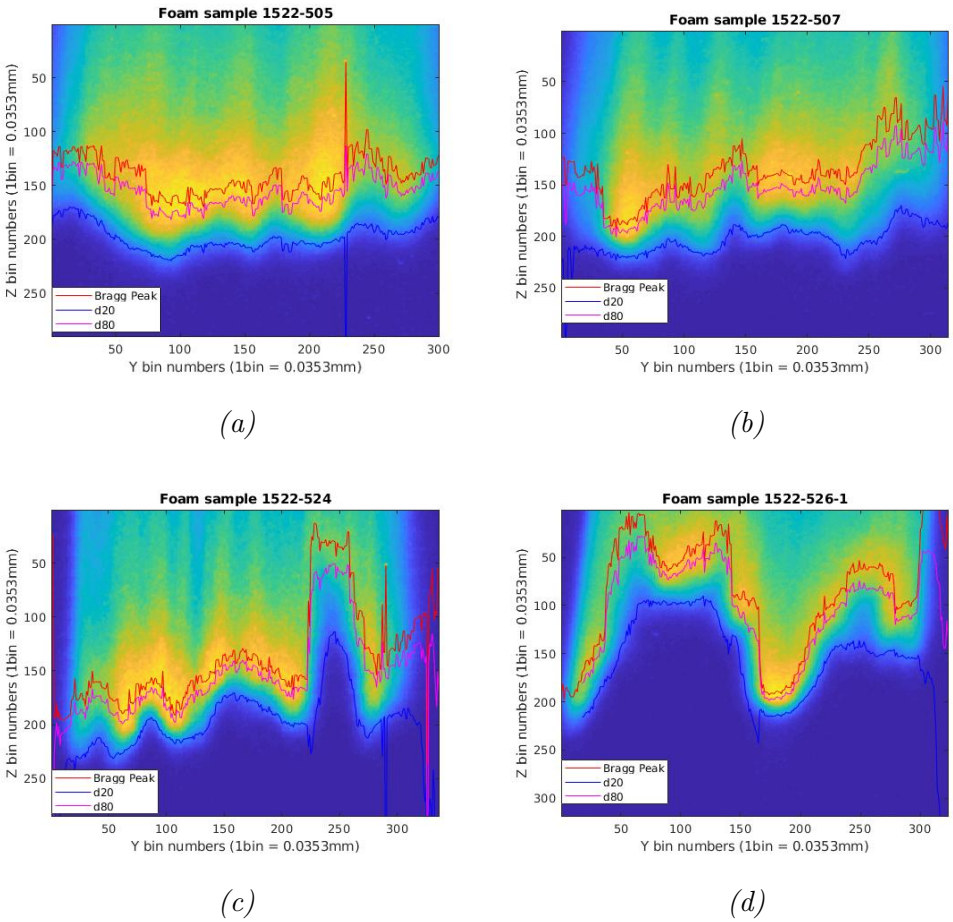

Figure 4.15: Bragg peak, d20 and d80 locations of each pixel line in the z-direction (downward) for experimental films.

4.6 Monte Carlo Benchmark

4.6.1 Monte Carlo Simulations for Finding the Bragg Peak

To explore the double Bragg peak as found in the previous experiment (figure 4.4), four sets of simulations were run without a voxel and with film assigend as water, PMMA, PET and KAPTON respectively. By assigning the film as a KAPTON (having the same density as that of two PET blocks on either side of the film) the double Bragg peak (assumed to be caused by density changes) disappeared as can be seen in figure 4.16.

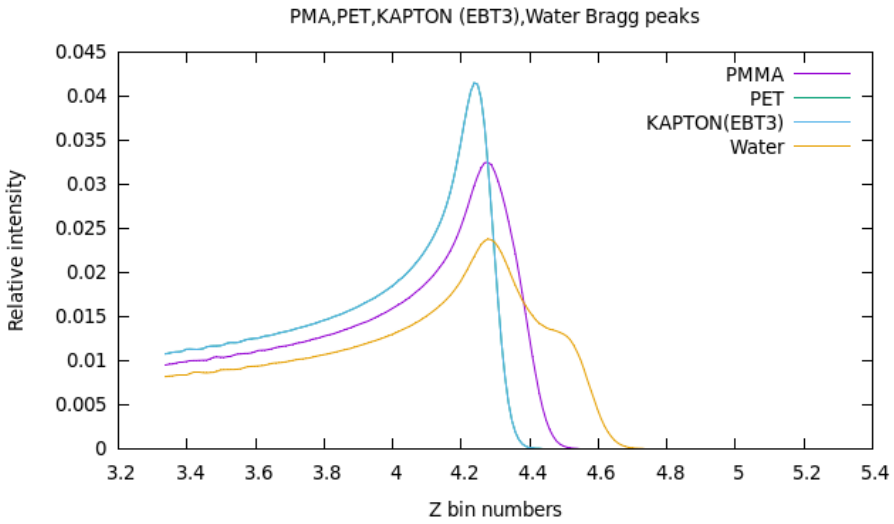

Figure 4.16: Graphs to show the 'pristine' Bragg peaks using water, PMMA, PET and KAPTON for the film 'materials' in FLUKA. Peaks for PET and KAPTON are very similar. PMMA represents the conditions in experiment-1.

4.6.2 SAWBONES® Scanning

The foam samples were scanned by Sarah Aldridge using Nikon XT H-225 micro-CT scanner which uses a Varian PaxScan 2520 1.3 megapixel amorphous silicon panel, available at the Materials Science and Engineering department at Swansea University. The scans were performed at 65 kV at a current of 190 μA on a tungsten target with only intrinsic filtration and 1 second acquisition per projection. The scanned foam samples were not cut to the size

used in the experimental set-up and were taken from different sections. During the cutting process, there was a possibility of foam edge deformation where material is lost or pushed inward and creating a slightly different desired density. It would not be possible to precisely align the foam, so a statistical approach is taken. The five foam samples were scanned and the images were stored in a format called DICOM which is a standardised medical imaging format compatible with MATLAB and the Monte Carlo graphical user interface FLAIR. The DICOM image data is structured in such a way that it contains the 3D monochromatic image and all the particulars related to the set-up of a usual scan as well as the details about an individual image and image as a set. Image information such as the image series number, the width and height of each individual pixel, the distance between each two slices and slice thickness are important for calculating the dimensions of image series when loading the series as a three dimensional object.

4.6.3 CT Image Processing with MATLAB

For creating a model (similar to the experiment) and running the Monte Carlo simulations, a set of CT images was required for loading in FLAIR which creates the Fortran input cards for FLUKA as described in section 3.5.1. Since the micro-CT images were for the entire foam, not the cut samples, the images had to be cropped using MATLAB. The 'dicomread' function is used to extract the images in MATLAB which creates a two-dimensional image matrix, and the matrix values corresponds to the intensity of the image. Extracts from the following MATLAB code specifically correspond to one foam sample (1522-507). All the CT data sets are handled in the same way and therefore the scripts are almost identical as can be seen in appendix C. The folder containing DICOM images data set is opened in MATLAB. The images are cropped with the same dimensions as were employed for the experiment i.e. in a 2 cm $\times$ 2 cm cross section. Two temporary variables 'tagimage' and 'imginfo' are generated to determine the image information by finding the number of pixels (see Appendix E.4 and E.5). The 'dicomread' function reads all the image information and here the 'tagimage' provides with the size of each pixel on the image series. Pixel information has been used to determine the proximate number of pixels required to create a 2 cm $\times$ 2 cm size matrix. The pixel dimensions are found to be 0.0434 mm by 0.0434 mm and accordingly

the number of pixels required to make a 20 mm thick section is 460.83 rounding up to 461 the nearest pixel. All pixels and slice numbers are rounded up to make sure that all of the 2×2 cm^2 proton beam is covered by the foam sample. From table 4.1 , the 0.4 cm water equivalent thickness of each foam is known and this can be kept constant by determining the exact thickness of image slices and calculating the approximate number of slices necessary to match the foam sample thickness. A list of image names is stored with a new variable using the 'dir' function to easily call all the files in a sequence.

Most of the standard DICOM information required to import the images into FLAIR for creation of VOXEL was missing from the micro-CT images. Therefore, another data set taken from some other phantom's (patient not involved) DICOM image was used to create new metadata. The spacing between slicing is stated as 0.0434 mm despite the slices being flush because it takes this value as the distance between the centres of successive slices. Pixel spacing, slice thickness, spacing between slices and slice location were altered to match. The slice location was calculated by using the current slice number and the distance between slices. UIDs, which are unique identification numbers associated with each CT dataset, were changed so as to differentiate between slices (the fixed metadata was based on one file not a whole set). Appendix E.6 is the code used to edit all image information and 'dicomwrite' writes new DICOM images with all necessary information.

The Hounsfield unit conversion in FLAIR is in part calculated using a calibration curve following a $y = mx + c$ line where m equals the variable 'rescale gradient' (RescaleSlope in the code) and c is the'rescale intercept'. The MATLAB code, given in Appendix E.7 , shows written to scale the overall image density equivalent to 0.4 cm water equivalent foam density. A new folder is created to contain the scaled files and the function 'dicomwrite' is used to write the cropped images as new files with the associated altered metadata from the structure. These new files can now be read into FLAIR as DICOM files for creation of a VOXEL.

4.6.4 Monte Carlo-FLUKA-FLAIR

For the Monte Carlo (FLUKA) simulation, an interface program called FLAIR, as discussed in chapter 3, was used. The program has the ability to 'build' a geometry of shapes, objects,

beams and detectors. To simulate the experiment at Birmingham University, a geometry similar to the set-up shown in figure 4.12 was created. Figure 4.18 is a screenshot showing the FLUKA geometry. A rectangular 1 cm $\times$ 1 cm proton beam of 0.036 GeV starts at the origin. Directly in front of the beam is either the foam sample or nothing (in the case of generating a pristine peak). In a real beam scenario, the accelerated particles energy are not ideally mono-energetic. It is because when the beam particles are accelerated around an accelerator in clusters, the accelerating potential at opposite ends differs from that in the middle as they gravitate slightly out of phase with the radio frequency (RF). This particular phenomenon and other effects together produce a small amount of energy (or momentum) spread that can be represented by a Gaussian distribution about the nominal energy [80]. Therefore, the full width half maximum (FWHM) of the beam needs to be considered for the FLUKA input and this value is quoted as 0.5% of the beam energy which is $\approx$ 0.25% of the momentum. So, the momentum difference has been calculated to input into FLUKA which is 0.00067 GeV/c (see figure 4.17).

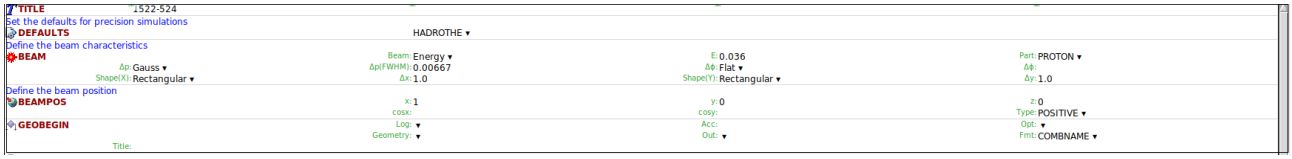

Figure 4.17: Screenshot of FLUKA input displaying beam settings.

Geometrical shapes are generated as a general geometry, structures are named and co-ordinate positions are assigned to them. Regions are then created, which can be a shape or a combination of shapes and subtracted shapes. For example, the blackbody around the experiment, which is used as a sink for stray particles is a region which consists of a sphere minus everything else in the geometry so as to create a shell to catch stray particles. Finally, materials are assigned to regions, for example, the void is just the air that fills everything in between objects. The materials used in actual experiments are all available in the program including PET, except for the foam. Therefore all the HU numbers and material densities are automatically associated with a region when assigning the material. The SAWBONES® foam is not an exact region as pixels are intensities. These intensities are associated with a

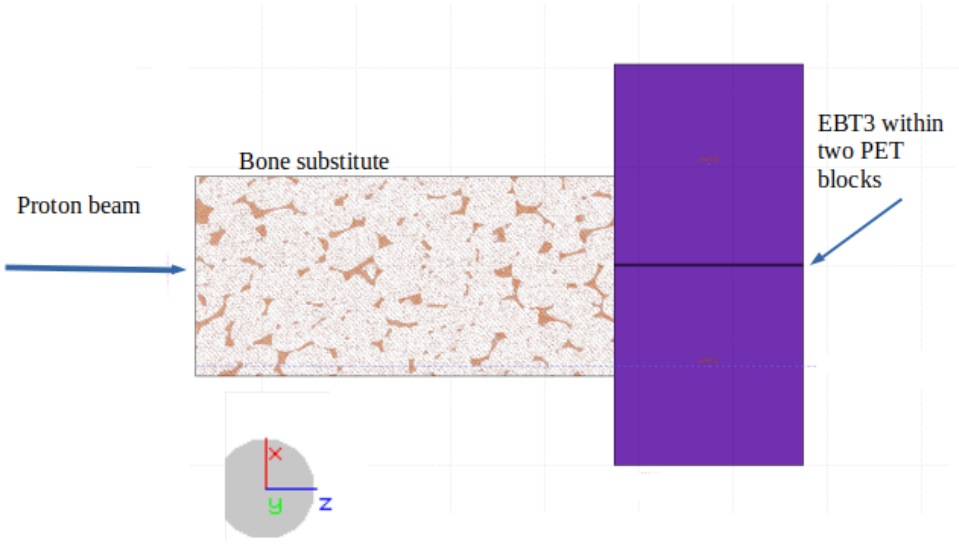

Figure 4.18: Screenshot of FLUKA geometry similar to experimental set-up.

degree of bone material where 0 intensity is taken as air (-1000 HU) and all other intensities belong to real bone material (tissue equivalent HU). Therefore, for creation of the foam VOXEL it is important to include the material file which converts the image intensities into relevant HU numbers. The standard example material file does not need to be altered as the rescale slope fits the data between given HU numbers. After adding the voxel as a loaded file, shown in the figure 4.19, FLAIR automatically takes a range of intensities as a region and assigns a HU. The number of primary, 2,000000, refers to individual protons. The main objective here is to do MC calculations to see the effect of variations in the geometry. For this project a big challenge is to have a statistically robust sample geometries and 2×10^6 particles are sufficient to have statistical precision of 3% which is considered good enough for determining the position of d80 and d20. More particles increase computation time but decrease errors. For each FLUKA simulation, in order to generate a voxel, the cropped images are placed inside the same directory as the simulation file and the DICOM tab is used to compile the images into dataset. After adding the materials file, the voxel can be generated and saved in the same folder. Following the voxel, there are two regions of PET and

(a) *(b)*

Figure 4.19: FLUKA geometry (a) defines regions (b) shows materials assignment to these regions.

a thin radiochromic film in between. The film is approximately 287 microns thick as stated in the specification document for EBT3 film. The film centres on the x-plane and follows perpendicular to the y-plane. The proton beam moves in the z-direction therefore the film starts at the point where the foam ends on the z-plane and ends 2 cm further, deep enough for the Bragg peak to appear. The PET is made large enough to encompass the entire beam so that it all diminishes around the film and there is no contamination of the film from the edge of the beam moving through the air. To record data as on the radiochromic film, a 'USRBIN' is created to encompass the entire film region. By making the x-direction one bin wide, but 200 in both the y and z planes the USRBIN can score energy as a 2D image, again recording intensities into a 2D matrix. Each simulation is repeated 5 times hence every intensity value comes with an associated standard deviation. The Userbin can be exported into ASCII format and then imported into MATLAB to be manipulated for graphing.

4.6.5 Dose Correction Factor for FLUKA

For proton radiation dosimetry, ionisation chambers have been commonly used to get results promptly. However, ionisation chambers do not easily provide information about 2D or 3D dose distributions which is often required for quality assurance in radiotherapy. Radiochromic films are a cheap and easily available dosimeter, which have comparably a much higher resolution and provide 2D or 3D dose information. For proton dosimetry with radiochromic film, the dose extraction procedure is however quite more elobrated as it involves a long film handling process (such as film cutting, scanning, calibration and then step-by-

step analysis) as well as their energy dependent behaviour, known as the LET effect, in film. For this project, Kirby's suggested model has been followed to account for the LET effect as a function of peak energy for running the FLUKA simulations. The comscw.f, a user routine in FLUKA, was modified so that the energy deposited at each step in the simulation was multiplied by an evaluation of the sigmoidal RE function at the proton energy in that step. The customised comscw FLUKA routine is given in appendix D.1 . According to Kirby's model:

$$RE = RE_0 + \frac{\Delta RE}{1 + \exp\left(-C\left(\mathrm{logE} - \mathrm{logE_0}\right)\right)} \tag{4.2}$$

where E is the proton energy and all other sigmoidal fit variables for EBT3 are taken from a thesis written by Daniel Kirby [80].

4.6.6 Monte Carlo Data Analysis

The ASCII files from the FLUKA output were exported into MATLAB for post-processing. The FLUKA input scripts for all simulations can be found in the appendix D . The files are generated as a 10 $\times$ 4000 matrix and before the data can be examined this must be converted into a 200 $\times$ 200 matrix which reflects the true dimensions of the models. The values are in order row-by-row so first the 10 by 4000 matrix must be transposed so it is read row-by-row not column-by-column. The function 'imagesc' generates a heatmap graph so it is possible to view where the Bragg peak is on the 2D image similarly to the original films, albeit in colour.

Four of the five CT datasets were converted into voxels and simulations were run. One of the datasets was corrupted and DICOM files were unusable. The four datasets were graphed using the MATLAB script given in listing 4.1 .

The graphs in figure 4.20 provide great visual analysis; however, for further comparison it is necessary to locate the precise points at which there is a maximum, minimum, d80 and the d20 of the distal fall-off. By graphing and comparing these the differences between the samples can be examined. For the radiochromic film in the experiment, a MATLAB script 4.1 was written for locating the d20, d80 and Bragg peak along each pixel on the Z-axis. The red lines corresspond to the Bragg peak position, the blue lines represent the

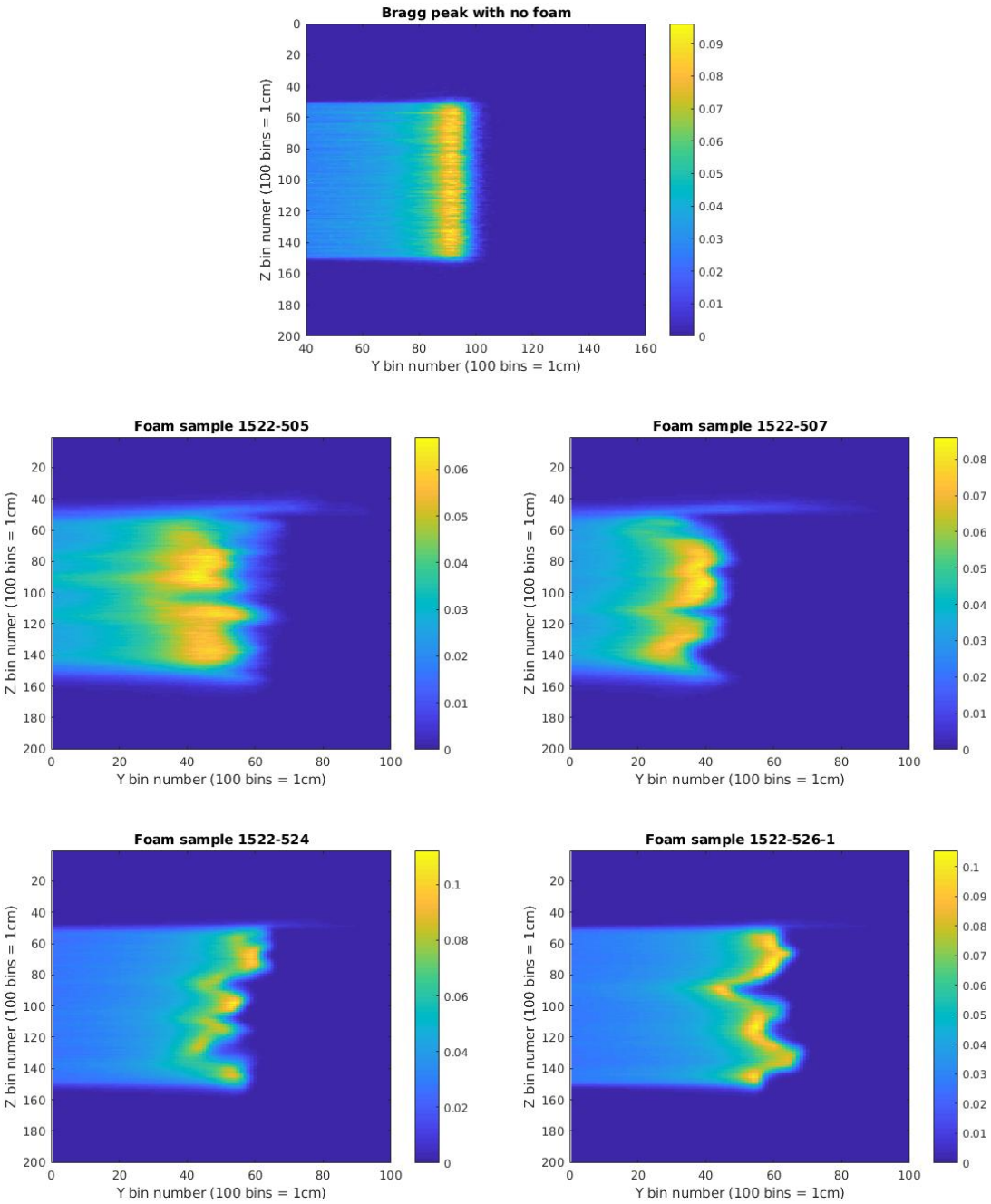

Figure 4.20: Outputs from FLUKA simulation show variations in Bragg peak for all four samples. A few streaks at the top of the four bottom inserts can be seen. This is the algorithm failing at the beam edge. The method samples a large number of rows, so these rows are excluded during film analysis.

d20 locations and the magenta lines the d80 position.

The d20 position is calculated by searching for the minimum dose threshold and fitting a best polynomial curve, using the function 'polyfit', between it and the Bragg peak value. The 'polyfit' function can create anomalous values in these regions as the values tend back towards zero; there is never going to be a polynomial that perfectly fits the graph. One of the constraints of polyfit is that the order of the polynomial cannot exceed the number of points. The d20 and d80 are positioned respectively at 20% and 80% of the distal fall-off. The axis is cropped to exclude the sides of film not exposed directly to the beam.

Listing 4.1: MATLAB code for determining the locations of the Bragg peak d80 and d20 locations based on a fitted polynomial.

```
T = load('505frun.asc');
PB = reshape(T',[200,200])';
figure(2); imagesc(PB)
pf = zeros(length(PB),2);
[m,i] = max(PB);
[mz,iz] = min(max(PB-m*0.1,0));
for K = 1:length(PB)
pf(K,:) = polyfit(1:(iz(K)-i(K)+1-2),PB((i(K)+2):iz(K),K)',1);
end
hold on
plot(i,'r')
plot((i'-m' ./pf(:,1)*0.8),'b')
plot((i'-m' ./pf(:,1)*0.2),'m');
%plot(iz,'r')
axis([40 160 1 100])
xlabel('Y bin number (100 bins = 1cm)')
ylabel('Z bin numer (100 bins = 1cm)')
title('Foam sample 1522-505')
legend('Bragg Peak','d20','d80', 'Location','Northwest')
```

The spread of the Bragg peak can be taken as the distance between the Bragg peak maximum and the d20 value. By finding the average over all of the z-direction pixel lines

which encompass the path of the proton beam the different foams can be compared. The errors of this calculation is calculated using the standard deviation function. The code given

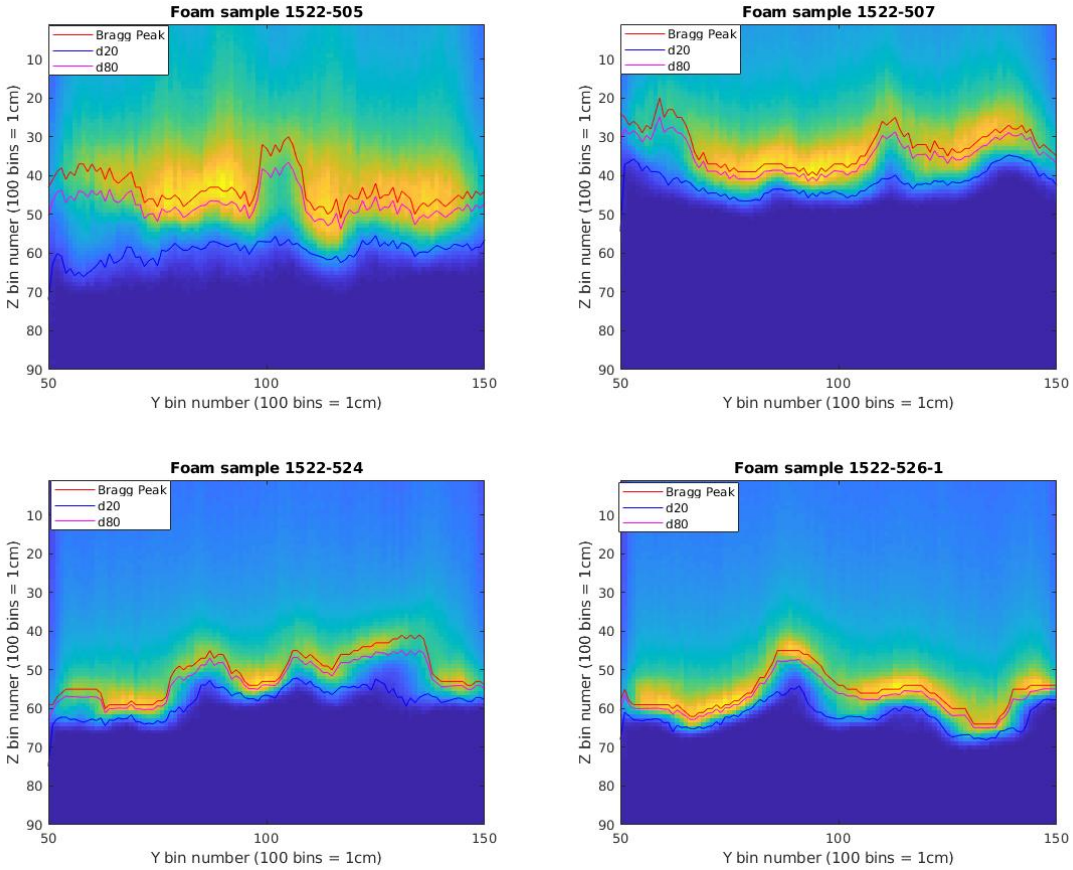

Figure 4.21: Bragg peak,d20 and d80 locations of each pixel line in the Z direction (downwards) superimposed on a heatmap obtained earlier from MC simulations without applying the LET corrections.

in listing 4.2 is used to calculate the z-position of d20 and subtract the lower z-position of the Bragg peak and then find the mean and the standard deviation. Similarly, the z-position for d80 is found. The mean and standard deviation for difference between d80 and d20 is calculated and compared for all sets of foam to analyse the effect of heterogeneities on the range of the beam.

Listing 4.2: MATLAB code for determining the mean and standard deviation.

```
d20 = (i'-m'./pf(:,1)*0.8);
d80 = (i'-m'./pf(:,1)*0.2);
d80_20=d20-d80;
d20t=[];
d20t=[d20t; d20(53:153)];
mean(d20(53:153))
std(d20(53:153))
mean(d80_20(53:153))
std(d80_20(53:153))
```

Sample	Density (g/ccm)	Mean d20 (mm)	Std d20 (mm)	Mean d80-d20 (mm)	Std d80-d20 (mm)
1522-505	0.09	7.119,5.959,7.212	0.324,0.382,0.307	1.503,1.481,1.719	0.222,0.259,0.472
1522-507	0.12	7.234,6.746,7.339	0.400,0.442,0.480	1.6607,1.800,1.748	0.5165,0.4384,0.423
1522-524	0.24	7.181,7.540,7.248	0.768,0.604,0.478	1.711,1.663,1.219	0.5976,0.554,0.457
1522-526-1	0.32	5.579,5.232,6.709	1.538,1.411,1.376	2.169,1.778,1.926	0.792,0.747,1.403
1522-525	0.48	6.610,5.5311,6.931	1.654,1.029,1.052	1.473,1.347,1.228	0.827,0.562,0.576

Table 4.5: Table of values calculated for mean d20 and mean $d80 - d20$ for all five foam samples used in this experiment. As it has been explained in section 4.4.1 that for each foam sample, the films were irradiated at three different positions (right, middle and left) of the bone substitute to get a better understanding of the degradation effect and to improve statistical sampling of the foam. Therefore, in the last four columns of this table three values in each column are calculated from three irradiated films for each foam sample.

Sample	Scaled density DICOM (g/ccm)	Mean d20 (mm)	Std d20 (mm)	Mean d80-d20 (mm)	Std d80-d20 (mm)
1522-505	0.089	6.123	0.261	1.267	0.301
1522-507	0.121	6.214	0.221	0.788	0.085
1522-524	0.240	6.817 1	0.453	0.826	0.185
1522-526-1	0.321	6.547	0.374	0.744	0.093

Table 4.6: Table of values calculated for mean d20, mean $d80 - d20$ and relevant standard deviations from the films placed in front of the four bone samples with an LET corrections applied (as explained in section 4.6.5) for MC simulation.

Sample	Scaled density DICOM (g/ccm)	Mean d20 (mm)	Std d20 (mm)	Mean d80-d20 (mm)	Std d80-d20 (mm)
1522-505	0.089	6.175	0.264	1.261	0.304
1522-507	0.121	6.249	0.215	0.783	0.084
1522-524	0.240	6.846	0.409	0.819	0.189
1522-526-1	0.321	6.575	0.384	0.739	0.096

Table 4.7: Table of values calculated for mean d20, mean $d80 - d20$ and relevant standard deviations from the films placed in front of the four bone samples with no LET corrections applied for MC simulation

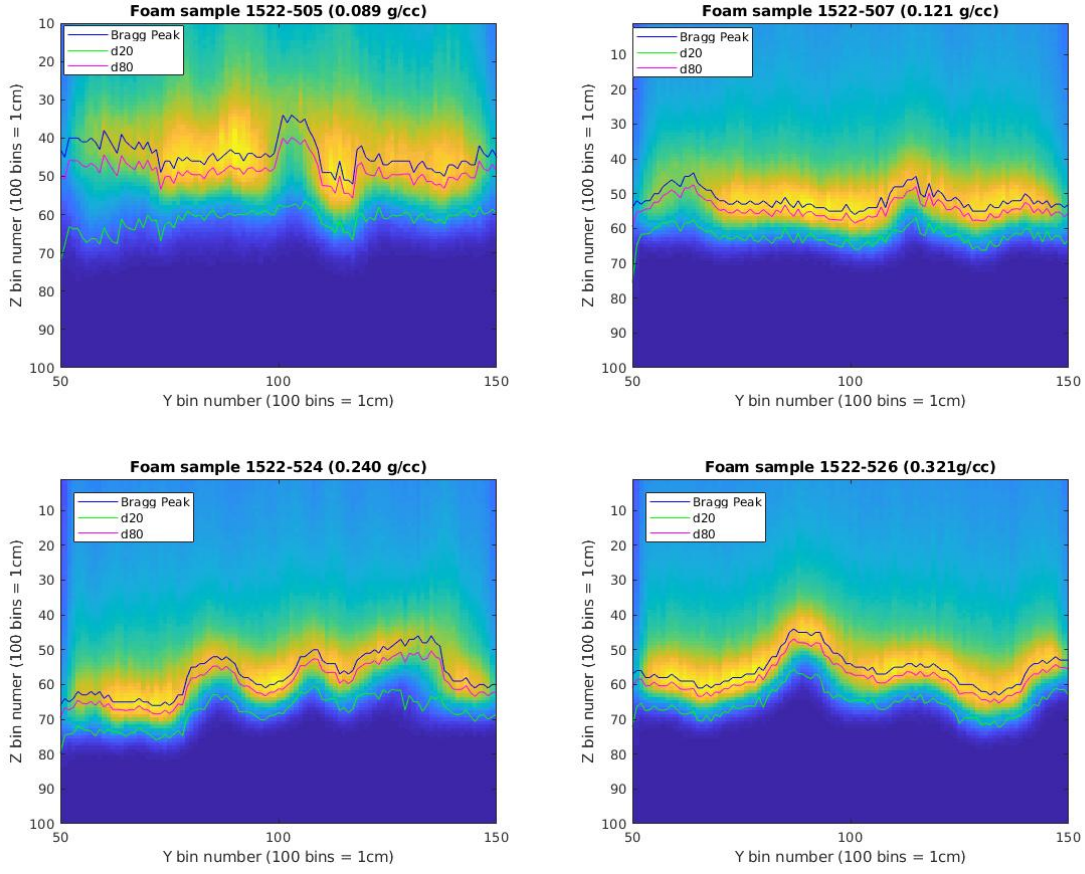

Figure 4.22: Variations in Bragg peak between the four samples simulated with FLUKA with LET corrections applied

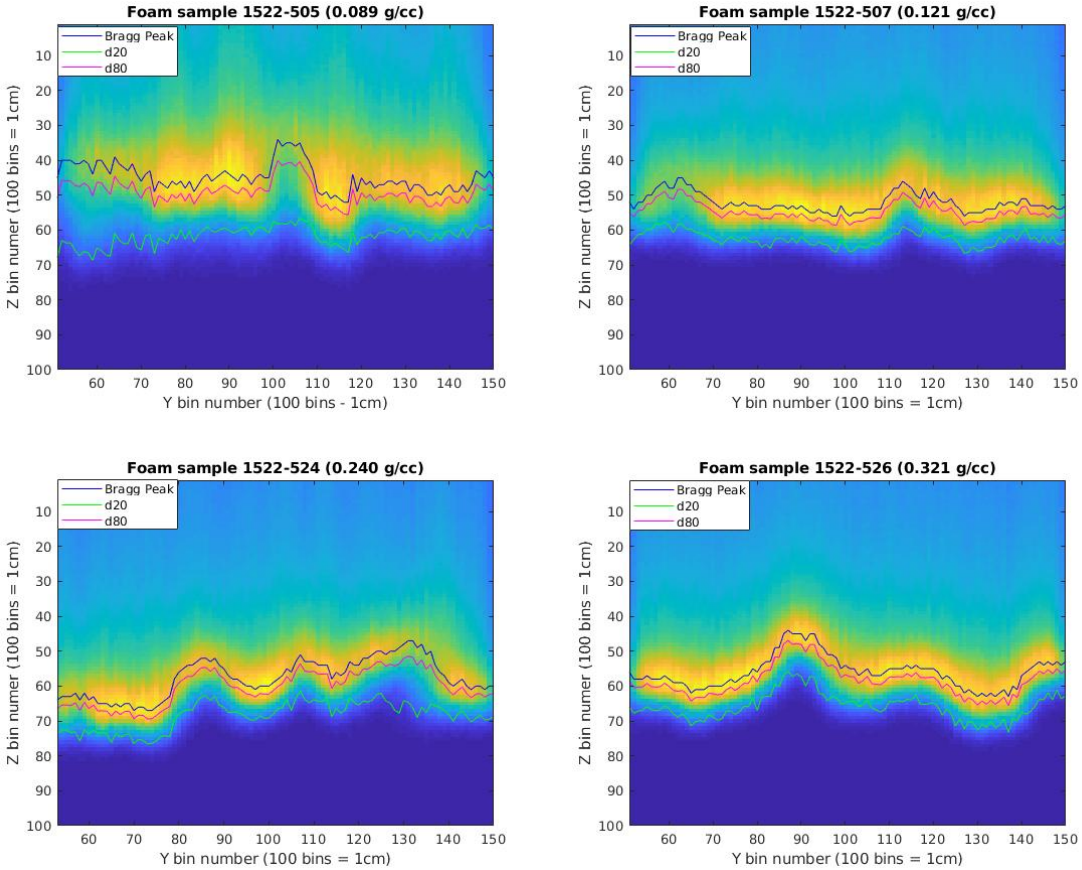

Figure 4.23: Bragg peak,d20 and d80 locations of each pixel line in the Z direction (downwards) superimposed on a heatmap obtained earlier from MC simulations without applying the LET corrections.

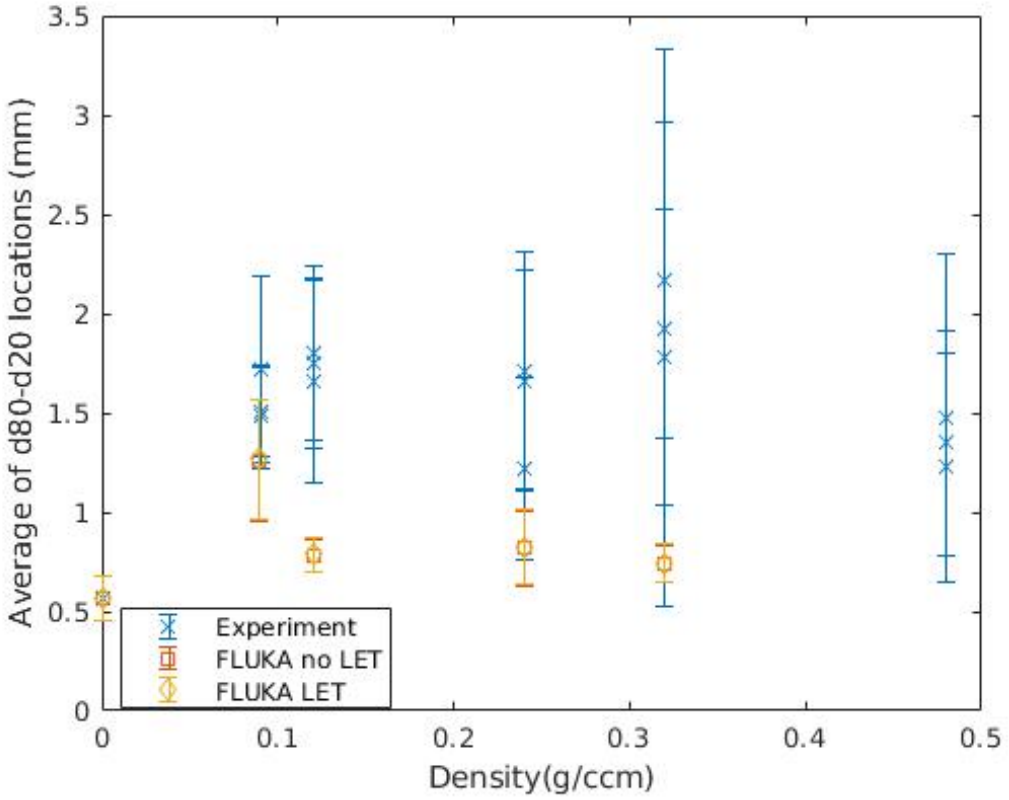

Figure 4.24: A graph to show relationship between foam density and mean difference in $d80 - d20$ *location of the distal fall-off as a function of foam density. The spread of the Bragg peak is taken as the difference between the d80 location of the peak and d20 of the distal fall-off. It has been explored by finding the average distance between the d80 and d20 line. This figure shows these averages and the standard deviation plotted as error bars. For simulated output some data points are missing as not all CT scans were available for simulation due to corrupted data in the highest density foam.*

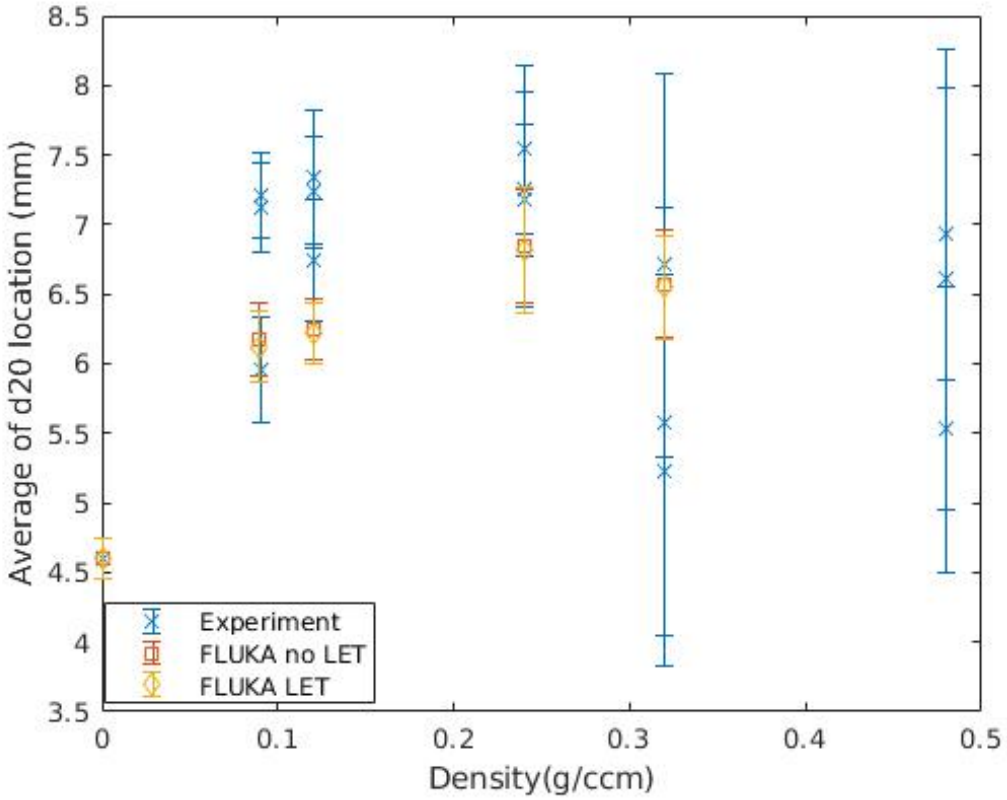

Figure 4.25: A graph to show relationship between foam density and d20 location of the distal fall-off as a function of foam density. The d20 of the distal fall-off is calculated to observe the general noise. Due to corrupted CT scans again missing simulation data points can be seen for high density foam.

4.7 Experiment Outcome and Analysis

4.7.1 Experiment-1

This experiment has been performed twice. On the first attempt, a double Bragg peak was recorded on the film in the absence of a foam sample. Figure 4.4a shows a pristine peak and an early Bragg peak can be clearly seen on the film. This is unintentional and not beneficial as a clear single Bragg peak is what is needed for post-processing of the data. Two Bragg peaks are persistent along the z-position, which is only expected for a uniformly shaped film when there is air between the beam origin and the film. Therefore, it was initally suspected that there was an air gap between the PMMA and film. Later it was found to be due to a mismatch in density, discussed in next section. This could have affected the position of the Bragg peak.

Figure 4.4b shows two examples of the films where a foam sample was present in the path of the beam. Both images belong to two different exposures with two separate foam samples; the top image is of one of the less dense foams and the bottom one of the higher density. By looking at these images it is clear that there are large variations in the Bragg peak compared to the pristine are along the y axis. It can also be seen that these variations are more intense for high density foam which is one of the expected outcomes of the experiment.

There are various stumbling blocks in the first experiment which make it difficult to reproduce the set-up with a computer model. Even though the thickness of the film is uniform by design, the use of clamps to remove the air gaps might cause the film to become slightly inconsistent in terms of its flatness and some variations in dose absorption might be expected. This is an effect which cannot be replicated on FLAIR. It is also difficult to record the precise dimensions and location of the experimental set-up according to the accuracy specified in the computer model. The orientation of the foams will affect the positions of the Bragg peaks on the film because of the nonuniform distribution of the pores and since the face in the field of view of the beam is square, there are eight possible orientations. The smaller foam samples (higher density) appeared to be fairly deformed at the edges of one side from the cutting method used. The side of the film with the active layer was also not recorded.

4.7.2 Double Bragg Peak Fact-finding

FLUKA simulations were run to investigate the reason for the double Bragg peak, found on the film during the experiment. At the first instance in the FLUKA geometry, the film and the blocks surrounding it were assigned the same HU number (PMMA) with no foam sample. The first graph in figure 4.5a showed a singular and consistant Bragg peak. For second set of simulations the block material has been replaced with water. The second graph (water film) is also steady but the distal fall-off is comparatively large. Figure 4.5b is a the representation of the amount of protons which escape the beam path due to collisions and other factors; however, the energy deposited in these tracks is negilgible. Summation of sections of y-plane and plotting of these examples of film materials reveals a clear second peak. The graph in figure 4.6 shows a very sharp and unique singular Bragg peak for PMMA film, and a double peak in water film at the same peak location as PMMA and a higher Z bin number. The convergence of the peaks at just below bin 70 clearly shows that a majority portion of the photons detected by the USRBIN are the result of a net increase of protons being received from the PMMA outside the film. In a setup like the PMMA film where the densities and HU numbers are consistent it is expected that protons from either sides of the boundaries will track in and out but this number should average out as a net increase/decrease of zero. This shows that the changes in densities are directly responsible for the net increase within the water film. Water has a lower density and HU number and therefore would be easier to travel through. The first peak is much higher than the second, suggesting more protons from outside the film than protons that originated in the film. This could be explained by the massive surface area to volume ratio of the thin film and the PMMA blocks being many times the size of the film.

In the experimental film it appears that the second peak has a higher intensity not the first. This could be explained as only roughly a tenth of the film is the active layer where the rest of the film could be absorbing protons and not recording any data. Another possibility is that the edges of the PMMA were distorted and higher density 'discouraging' protons scattering in the boundary region between the PMMA and the film.

4.7.3 Comparison Between the Experiment and the FLUKA Simulations

In figure 4.10 there is a trend for all samples observed in the original experimental data. It can be seen that the fourth data actually has a decrease in Bragg peak spread. The third and fourth points correspond to datasets that are both included in the FLUKA data. There are a number of factors that could account for this difference. The data are not of sufficient quality to form conclusions about the trend. It might be reasonable to expect them all to be the same, as foams were cut to equal areal density. The effect is stronger per unit length in the higher density foams. The general noise observed, particularly with the d20 line, in the original film data could skew the average up or down. The sample may not have been completely square to the beam. The general trend is upwards, even more so with the FLUKA results. The effect is stronger per unit length in the higher density foams. More samples for both the FLUKA simulations and the experiment would be required to further justify the similarity in graphs but they do both suggest the expected outcome of this research; that the higher density porosity leads to increased d20. Porosity increases to 50% density then decreases. It can also be seen that with the FLUKA results there is reduced error at lower density samples showing a trend between density and error size which represents the variation in the path length.

4.7.4 Experiment-2

The second experiment was performed with an aim to achieve several possible improvements in the outcome of the physical experiment.

4.7.5 Double Bragg Peak Solution

This time by considering the properties of EBT3 film as described in section 4.2.1, it has been decided to use EBT3 rather than HD-V2. In order to eliminate the double Bragg peak, it was absolutely essential to find a block material that would have a density similar to the density of the film. After research, it has been found that the polyethylene terephthalate (abbreviated as PET) has a density (1.38 g/cm^3) equivalent to the density of EBT3 film.

Figure 4.16 shows the graphs obtained from FLUKA simulations for different film and block material combinations. The film material was kept as KAPTON (which replicate EBT3 properties in FLUKA) and the block material was changed each time to find a singular and consistent Bragg peak. The Bragg peaks for PET and KEPTON overlaid each other as can be seen in figure 4.16. Therefore, for the real experiment the radiochromic flim was clamped between two blocks of PET with a dimension of 2×2 cm^3. This time every possible attempt was made to minimise the air gap between the beam origin and the film. Figure 4.14a shows a pristine peak recorded with the absence of a foam sample. A very clear and consistent single Bragg peak can be seen as needed for post-processing of the data.

4.7.6 FLUKA Simulations

Figure 4.20 compares the PET film for a pristine beam with the simulations run with the four working datasets of the foam samples. They are ordered with increasing densities; top left, top right, bottom left and bottom right. As the density increases the Bragg peak location starts to vary remarkably. These variations are due to how much of the foam material is in the path of the proton. The foam density is only an average as some beam tracks will have more air pockets and others will pass through more 'joints' in the structure. The thickness of these joints will increase with an increase in the density of the foam; as visible in figure 4.1 . More significantly the Bragg peak does appear to smear or spread out, as the density of the sample increases, this being the result of the experiment we wish to replicate. The FLUKA simulations were run twice; first without applying any LET corrections for film and secondly with the LET corrections to resolve the film quenching effect. The code was originally written to find the maximum, d80 and d20 values of the original film data (figure 4.21 and figure 4.23). The spread of the Bragg peak is taken as the difference between d80 location of the peak and d20 of the distal fall-off. This was explored by finding the average distance between the d80 and d20 line. Figure 4.24 shows these averages and the standard deviation of their calculation as error bars.

4.7.7 Comparison Between the Birmingham Experiment and the FLUKA Simulations

The results obtained from experiment were plotted against the results from both sets of FLUKA simulations. Figure 4.24 shows the trend for all samples as observed in the original experiment versus results from FLUKA. This experimental benchmark manifests similar trends in the variations of the range of protons penetrating through different density foam samples. The magnitude of the effect for the experimental datasets is larger compared to those from the FLUKA output. As the film for each set of foam was exposed at three different locations; these larger error bars certify the passage of the beam through different paths in the foam. As the protons get scattered along the path; therefore, changing their directions; this effect here exaggerates the variations in the range. The physical experiment evidence these scatterings. The Monte Carlo modeling back up the experimental data and gives similar features to the experiment. Quenching of the film response in the Bragg peak results in variations in the error bars. An attempt was made to model this effect in FLUKA; however only small variations were evident.

In chapter 5 the characteristics of FLUKA are benchmarked against the Eclipse treatment planning system (TPS) golden data for proton therapy.

Chapter 5

Comparison of a Monte Carlo Model of a Proton Radiotherapy Beam with Eclipse Golden Data

5.1 Aims and Objective

The main purpose of the work described in this chapter is to benchmark the characteristics of FLUKA (a Monte Carlo code) against the Eclipse golden data for proton therapy. This project has been designed to assess the following aspects: 1) What the treatment planning system has determined for the energies required to deposite a desired dose in a 10 $\times 10 \times 10$ cm^3 VOXEL in a water-filled phantom,2) What sort of distributions it gives on recalculation with a high quality Monte Carlo calculation (FLUKA). 3) Compared with the treatment plans acquired from a planning system, what happens with a change in the phantom material, for example: bone or graphite. Graphite is a material of interest because it is used in proton calorimetry for the propagation of primary standards.

5.2 Merits of Radiation Dosimetry

The main objective of radiation therapy for any cancer treatment is to provide maximum dose to the target volume (to kill cancer cells) and minimum dose to the adjacent healthy tissues

(to avoid side effects and cancer recurrence in future). Therefore, a precise knowledge of the dose deposition is required for optimum treatment outcomes. Thus it is very important to acquire the exact target position and information about the beam output. Accurate dosimetry is always essential to boost and maintain the patient's survival rate.

The basic requirements for uncertainty calculations in the dose to a target volume are prescribed by national or international government organisations responsible for providing recommendations and guidance on radiation protection. According to the International Commission on Radiation Units and Measurements (ICRU) report 24, the uncertainty in the amount of energy transferred and therefore the dose delivered to a target volume must be within 5% for practical clinical radiotherapy [84]. There is always a possibility for many other factors such as patient positioning, target movement and tissue heterogeneities to contribute towards dose uncertainties in the patient's body. Therefore, to stay within the ICRU recommended target dose limits, the uncertainty in the absorbed dose in a homogeneous phantom should be 3% or less [19, 85].

For most precise measurements and to provide compliance and consistency in radiation dosimetry as well as across all fields, primary standards laboratories at national measurement institutes (NMI) exist in over one hundred countries. Among these, only thirteen laboratories provide primary standards for dose measurements [86]. These national measurement institutes hold the standards for basic units and establish new standards to sustain novel measurement solutions [87]. The National Physical Laboratory (NPL) is the UK's leading NMI which provides accurate measurements of the primary standards for radiation dosimetry. There are new proton therapy centers under construction in the UK [88] therefore, for precise proton dose measurements, it is important to know which primary standards are ready for publication by the NPL. According to the Particle Therapy Co-Operative Group (PTCOG) survey, NPL has agreed to provide measurement services for all five under construction proton therapy centers in the UK [89].

5.2.1 Absorbed Dose

The absorbed dose to tissue (D) is one of the fundamental quantities used in radiation dosimetry. It is defined as the amount of radiation energy absorbed in a material-filled

volume per unit mass. This transmitted energy is equal to the sum of all energy that enters the volume minus all energy leaving that volume, considering any mass energy conversion within that volume [90]. The mathematical notation for absorbed dose is:

$$D = \frac{\triangle E}{\triangle m} \tag{1}$$

The SI units for absorbed dose are gray (Gy). While, 1 Gy = 1 Jkg^{-1}.

As clinically relevant quantities such as tumor-control probability (TCP) and normal tissue-control probability (NTCP) are highly dependent on the accuracy of the absorbed dose, it is more important to consider the accuracy and reproducibility in absorbed dose determination. For dosimetry data comparisons at different institutions, the dosimetry proficiencies should be similar at all facilities [91]. The absorbed dose absolutely depends on the strength of the radiation field and the quality of the absorbent material. In the field of radiation therapy, a substitute of the material to human tissue which is being irradiated is considered. The main purpose of treatment planning is to predict the precise amount of energy absorbed by irradiated tissues. The standard uncertainty in the absorbed dose to the treatment volume should be less than 5% while, in some cases the criterion is less than 3% [92]. However, to certify standardisation, clinical reference dosimetry takes into account the absorbed dose in water which is basically the measurement of energy deposited in water rather than in tissues. The main reason for water to be the material of choice is that its irradiation absorption characteristics are similar to human tissues. It is possible to convert the dose from one material to another by applying some conversion factors [93]. Therefore, for proton therapy the dose to water can be converted into the dose to tissue by multiplying it by the ratio of the proton stopping power of the medium.

5.3 Calorimetry

Calorimetry is the most commonly adopted method for dosimetry of in-practice proton beams as recommended by ICRU report 59 and TRS-398, published by the International Atomic Energy Agency (IAEA) [94]. When ionising radiation interacts with a material,

it causes an increase in the temperature of the absorbent material and appears as heat (i.e. all the ionisations resolve into heat without changing the physical or chemical state of the absorbent material). The measurement of this rise in temperature due to irradiation is called calorimetry. Calorimeters are absolute dosimeters as they are designed to measure the direct energy in an absorbent material by measuring the rise in temperature. Currently, both graphite and water calorimeters are used as primary standards at most national measurement institutions. If ΔT_m is the rise in the absorbent temperature that can be measured with a thermistor and a Wheatstone bridge, the absorbed dose to the material D_m can be measured as [95] ;

$$D_m = C_m \times \Delta T_m \tag{5.1}$$

where C_m is the specific heat capacity of the absorber and ΔT_m is the increase in temprature due to radiations [96]. In accordance to the relationship between dose and energy, the absorbed dose to water D_w can be calculated as:

$$D_w = C_x \Delta T f_{w,x} \tag{5.2}$$

where C_x is the specific heat capacity of the calorimeter material and $f_{w,x}$ is the dose conversion factor for converting the measured dose to its water equivalent. Many other materials such as polystyrene, aluminum, silicon have also been used for commercial dosimetry [86]. In radiotherapy practice, the most commonly used material for absorbed dose calorimetry is graphite. Water calorimeters are useful for direct measurement of heat, but due to interaction of ionising radiations with water some radiochemical reactions take place which may either discharge extra heat or absorb the medium's heat and therefore obstruct the correct measurements of the absorbed dose, is known as heat defect. Therefore, the complexity of these calorimeters makes it difficult to achieve correct values for absorbed dose. Graphite calorimeters have been used historically as graphite itself is a solid material with high thermal conductivity and a negligible heat defect. However, the main constraint for these calorimeters is that the graphite is not actually a material of interest [97]. Therefore, for radiotherapy dosimetry, the use of graphite calorimeters acquires accurate knowledge of conversion factors for the dose from graphite to absorbed dose in water. The International Commission

on Radiation Units and Measurements (ICRU) report 14 also recommends graphite as the best choice for calorimetry and provides conversion factors [98].

Calorimetryhas been the method of choice for the National Physical Laboratory (NPL) as a primary standard for calibration of absorbed dose measurements for many years in the UK. Calorimetry for photons and high-energy electron beams for treatments is already used in practice by NPL and they claim for calorimetry to be the premise of dosimetry for high dose rate (HDR) brachytherapy calibrations as well as for highly energetic protons.The NPL calorimeters are fabricated from graphite and the absorbed dose from graphite is converted to absorbed dose in water after applying some correction factors [99]. These graphite calorimeters are used to calibrate the field chambers by comparison against the calorimetry results in one of the NPL's well-defined LINAC facilities.

5.4 Gamma Index(γ) Analysis

The high complexity of the modern radiation dose delivery systems and requirement for precise dose to the target results in a demand for accurate dose evaluation tools. The main objective of these evaluation techniques is the comparison between delivered and planned dose distributions. For quantitative dose analysis, the γ-evaluation tool was first introduced in 1998 by Low et al. [100]. Since then improvements and modifications in the original γ-evaluation algorithm by various authors have made it one of the most popular dose distribution comparison methods [17, 101].

Gamma analysis has become a standard method to analyse measured dose distributions in one detector system versus the dose predicted by commercial treatment planning systems. It integrates the dose difference (DD) and distance to agreement (DTA) criteria to determine a dimensionless matrix for each point in the evaluated distribution. DTA is typically taken as the distance between points in the two dose distributions that have equal dose. The DTA and DD criterion are set to ascertain the passes or fails of the dose distributions across each point. The reference points are computed one by one to dictate their dose difference and DTA and these points are compared versus pre-set DD and DTA criterion. Conventionally, the measured dose distributions (evaluated dose distributions), $D_m(\vec{r}_m)$ are compared to the

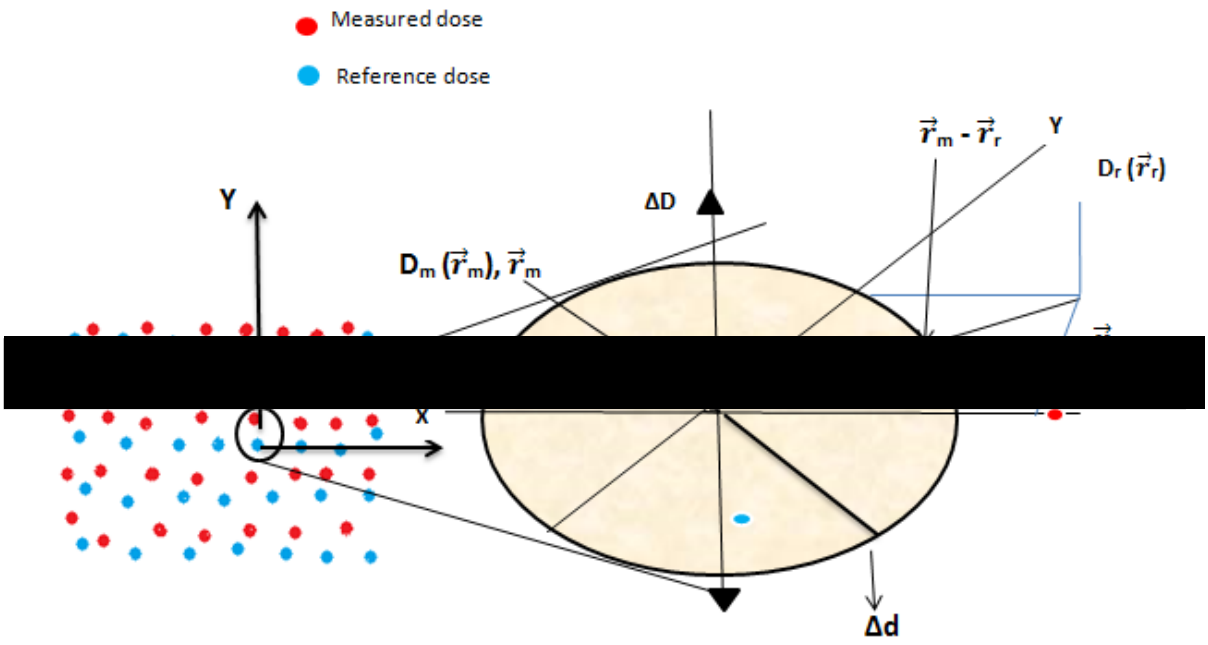

Figure 5.1: The Geometric representation of combined gamma criterion for dose difference and distance to agreement for a 2D dose distribution figure is redrawn based on information taken from [17]

.

reference dose distributions $D_r(\vec{r}_r)$ given at $\vec{r}_m$ and $\vec{r}_r$ vector positions respectively.

The generalised gamma evaluation function Γ is defined as

$$\Gamma(\vec{r}_m, \vec{r}_r) = \sqrt{\frac{\vec{[r}_m - \vec{r}_r|^2}{\Delta d^2} + \frac{[D_m(\vec{r_m}) - D_r(\vec{r_r})]^2}{\Delta D^2}}, \tag{5.3}$$

where, Δd here is used for distance to agreement and ΔD represents the dose difference criteria. The expression $|\vec{r}_m - \vec{r}_r|$ is the spatial distance between the evaluated and reference positions and $|D_m(\vec{r_m}) - D_r(\vec{r_r})|$ is the dose difference between the two positions. The gamma calculation is performed for each pixel value within the reference dose distributions data set. The evaluated point with the minimal $\Gamma(\vec{r}_m, \vec{r}_r)$ value is precisely proportionate to the reference point and is known as the gamma (γ) index correspondent to that reference point:

$$\gamma(\vec{r_r}) = \min\Gamma(\vec{r}_m, \vec{r}_r) \forall \vec{r}_m \tag{5.4}$$

A value of $\gamma \leq 1$ specifies that the points lie within the DD/DTA passing criteria therefore the evaluated distribution is accepted at that point. While for all $\gamma > 1$, the calculation fails [101]. Commonly used passing criteria are $\Delta D = 3\%$ and $\Delta d = 3$ mm or $\Delta D = 5\%$ and $\Delta d = 5$ mm. A percentage of points will fail due to measurement uncertainty. A distribution is typically considered acceptable if 95% of points pass the criterion.

5.5 CERR

A MATLAB-based computational environment for radiotherapy research (CERR) is produced in order to fulfill basic needs in radiotherapy planning research. CERR is an efficient integration tool to develop treatment planning concepts. It helps to combine different programming languages such as MATLAB, C^{++},FORTRAN, etc. with radiotherapy planning data. CERR is designed to access treatment plans from entirely different treatment planning systems using archiving tool and allows sharing and distributing research results.

5.6 Materials and Methods

5.6.1 Eclipse Single Field Treatment Plan

The Eclipse treatment planning system (TPS) from the Varian Medical System which contains golden data can be used to find contributions of individual energies for forming a 10 cm wide spread-out Bragg peak. For this purpose, a water-filled phantom (HU=0) having $20 \times 20 \times 20$ cm^3 dimensions has been created in Eclipse and inside it a box of $10 \times 10 \times 10$ cm^3 was contoured. These two structures were named as PHANTOM and PTV-HIGH respectively. A single field plan was generated for a designed phantom in order to deliver a uniform dose of 100 cGy to the PTV-HIGH volume. This plan produced a 10 cm wide spread out Bragg peak and a series of beam energies with the superposition of 714 spots to paint the dose to the target volume. A set of all these energies along with their weightings is shown in the table 5.1.

5.6.2 Creation of FLUKA Input File

The Monte Carlo system FLUKA has been used to simulate the transport of protons in water phantom for generating a radiotherapy plan similar to the one generated by treatment planning system (TPS). The Eclipse plan was exported in a DICOM format, which contains information required to create FLUKA input files. TPS generated RT files contain sets of DICOM images, the RD files provide information about the dose distributions, the RI files gives beam information and the RS files contain structure sets and regions of interest (ROI) as anatomical contours. Based on all information extracted from these files, FLUKA input files were produced for 19 nominal beam energies ranging from 81.7 MeV to 147.8 MeV.

FLUKA Defaults

FLUKA offers a set of default physics settings which enable the user to select the best settings for specific applications. The DEFAULTS card settings have all been optimised for a particular type of application. The script defines what FLUKA defaults are to be used for calculations. It provides the input file with a HADROTHErapy DEFAULTS card. The

Number	Nominal beam Energy(MeV)	Weights
1	147.8310	29.2690
2	144.4980	9.5707312
3	141.0220	7.8421016
4	137.5930	6.0577307
5	134.2030	4.9137096
6	130.8360	4.0850229
7	127.4790	3.4765034
8	124.1160	3.0308599
9	120.7310	2.6969254
10	117.3100	2.4457521
11	113.8360	2.2627070
12	110.2930	2.1231220
13	106.6610	2.0203412
14	102.9220	1.9474663
15	99.0520	1.8895754
16	95.0270	1.8525060
17	90.8180	1.8217480
18	86.3920	1.7971231
19	81.7090	1.7799022

Table 5.1: TTPS generated set of nominal beam energies required to paint the target volume. Information is extracted from the RN.dcm (TPS output file) using the MATLAB code as can be seen in Appendix F

.

HADROTHErapy settings are optimised for hadron therapy physics, and are further outlined below:

- Electro Magnetic FLUKA (EMF) is on by default for SDUM HADROTHErapy. EMF is used to request a detailed transport of electrons, positrons and photons.

- The inelastic form factor corrections to Compton scattering and Compton profiles are activated.
- Low-energy neutron transport is turned on. Thermal energies are included (with high energy neutron thresholds at 20 MeV).
- Fully analogue absorption is implemented for low-energy neutrons.
- The particle transport threshold is set at 100 keV, except for neutrons (1×10^{-5}eV).
- The multiple scattering thresholds set at the minimum allowed energy, for both primary and secondary charged particles.
- Delta ray production is on with a 100 keV threshold.
- Restricted ionisation fluctuations are on, for both hadrons/muons and electromagnetic particles.
- The ratio between hadron/muon upper- and lower interval limits of dp/dx momentum loss is set at 1.03. The amount of the kinetic energy to be lost in a step is set at 2%.

Beam Energy

A set of 19 different nominal beam energies, as given in table 5.1, have been utilised to create FLUKA input files. These beam energies and the particle types are defined in the FLUKA input files using the available BEAM card which defines several beam characteristics such as the type of particles, energy, divergence and profile. An example of FLUKA input for 147 MeV beam energy can be seen in figure 5.2. For this project, the kinetic energies of particles have been converted into associated momentum (GeV/c) and also the momentum spread Δ P(FWHM) (GeV/c) is defined on the BEAM card as Gaussian distributions. The beam divergence angle ($\Delta\phi$) was calculated and entered in mrad by considering the distance from source to the phantom isocenter and information obtained from DICOM data.

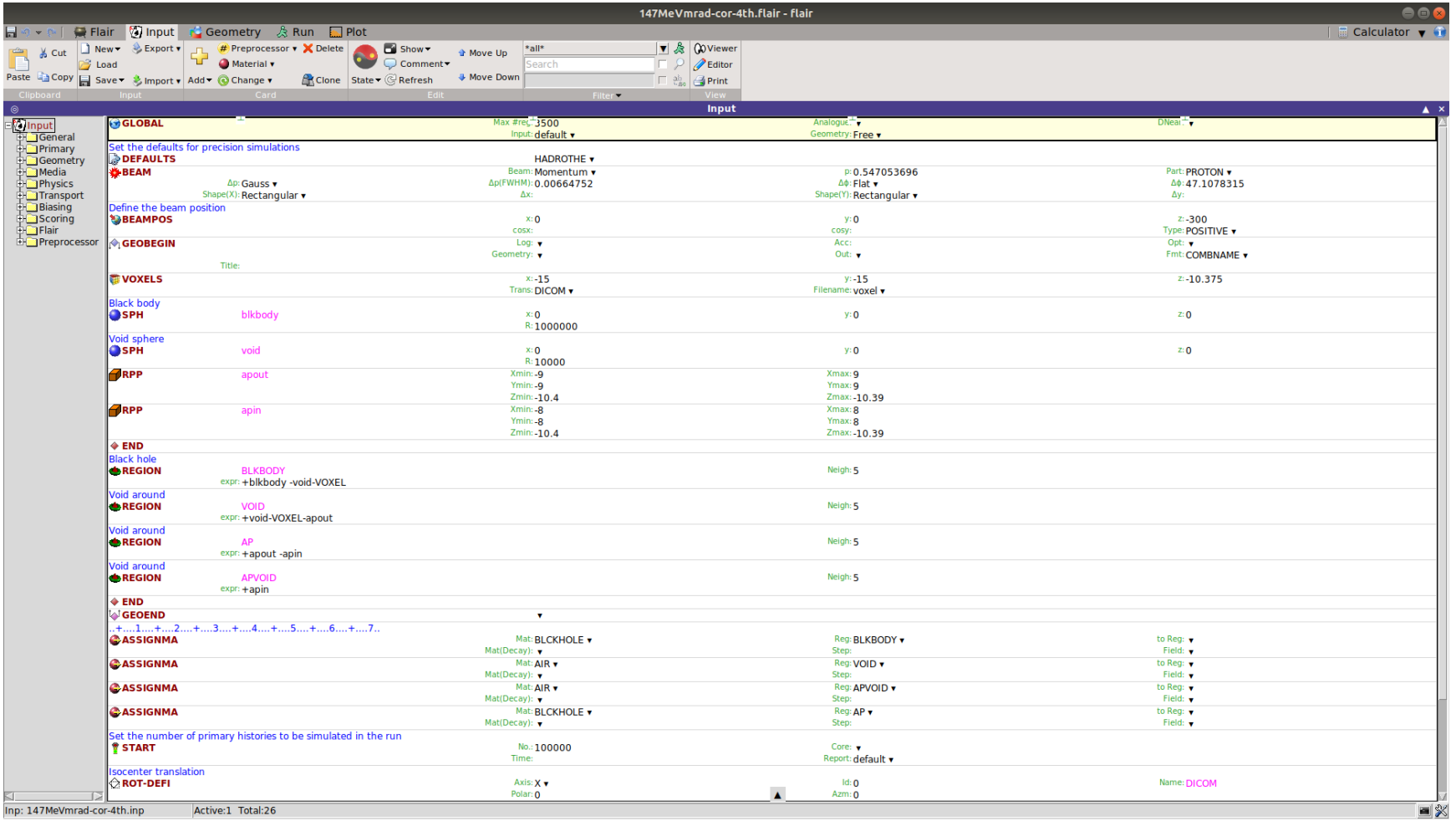

Figure 5.2: A screenshot of the FLUKA input file (147 MeV beam energy) used to simulate beam. Similarly nineteen individual input files (each with different beam energy) were generated to run Monte Carlo simulations.

Beam Direction Transformation

The BEAMPOSit card defines coordinates of the centre of the beam spot (i.e. the point from where the beam starts) and the beam direction. In the FLUKA coordinate system the beam is referred to as travelling along the positive z-direction [102]. For the simulation of a phantom in FLUKA, the transformation of the beam direction in relation to the placement of radiation source with respect to the patient position is essential. Therefore, by comparison of the FLUKA coordinate system with that of the International Electro-technical Commission (IEC) it has been realised that the patient on the treatment table will receive radiation in xy-plane. So, the beam position and its coordinates are defined in the BEAMPOSit card to reflect this (see in fig 5.2).

Dose Scoring

The USRBIN scoring card was inserted into each input file for dose scoring. USRBIN scores the distribution of one of several quantities in a regular spatial structure (binning detector) independent from the geometry [102]. A dose grid of size equal to the TPS dose grid was defined for all three x, y and z-coordinates, and the binning information was kept similar to that of the TPS dose-grid to remap the dose distributions at the correct position.

Running the FLUKA Input

For each simulation, the number of primary histories was set equal to 1×10^6 and each input was run for 5-cycles to get better statistics with a minimum standard deviation. It took around 33 hours to run the simulations for all the 19 input files.

5.6.3 MATLAB Post-Processing

MATLAB is a numerical computing environment, written in a proprietary programming language and developed by MathWorks. The USRBIN outputs were extracted from FLUKA-FLAIR to MATLAB for plotting a 3D dose distribution similar to the TPS-generated 3D dose profile in order to compare and analyse any differences in dose to the target volume. A code was written in MATLAB to extract all the plotting information from the USRBIN

output .bnn files and to multiply each beam's deposited dose to its relevant ScanSpotMetersetWeights to make a dose from FLUKA to be comparable to the dose from the treatment planning system (TPS). A 3D dose matrix with dimensions similar to those of the TPS was created. Figure 5.3 shows 3D dose profiles from both the TPS generated dose file and the Monte Carlo output post-processed file.

(a) TPS 3D dose. *(b) FLUKA 3D dose.*

Figure 5.3: 3D dose profile from treatment planning system vs FLUKA-FLAIR dose profile.

Normalising the Dose Distributions

It is important to normalise the dose distributions for making a comparison between dose from FLUKA and TPS outputs. Any information about the number of particles used for treatment by TPS was not provided, which caused a problem for proper normalisation. FLUKA calculates the dose distributions normalised per unit of primary particle (Gy/particle) therefore, if the number of particles used for dose calculations in the TPS are available these numbers can be multiplied by the FLUKA calculated dose in order to achieve the total calculated dose comparable to the TPS dose distributions. The ICRU report 78 gives us information that the relative dose can be normalised at a well-defined geometric point [103]. Therefore, it has been decided to normalise the dose at the isocenter position to get sensible results for this project.

5.7 Results

Dose Uniformity

The main goal of radiation therapy is to distribute a uniform dose to the cancerous volume while sparing the surrounding normal structures. In radiation therapy treatment planning, the dose uniformity is defined as the dose homogeneity inside the target volume that plays a vital role for effective treatment output [104]. In most of the patients, the exact distribution of clonogenic cells is always unknown and the planners always aim to attain uniform dose distributions within the planning target volume. However, the intrinsic attributes of the treatment beam makes it difficult to achieve the 100% dose homogeneity. Therefore, in clinical practice some dose heterogeneity is always expected and has to be accepted [105].

The beam uniformity or flatness is basically a maximum admissible percentage difference from the mean dose within the central 80% of the full width half maximum (FWHM) of the profile. This definition of the flatness is in correspondence to the American Association of Physicists in Medicine (AAPM) report 47.

$$Flatness = \left[(d_{max} - d_{min})/(d_{max} + d_{min})\right] \times 100 \tag{5.5}$$

where, d_{max} and d_{min} are the maximum and minimum dose values across the dose profile inside the core of 80% of FWHM. The flatness defined in equation 5.5 actually quantifies the unflatness [106]. As this terminology is extensively used and accordingly the same title has been used in this project. The beam flatness has been measured for a 10×10 cm^2 field size.

Dose Flatness in Water

For measuring the normalised depth dose as a function of energy in the absence of any experimental data, it has been assumed that the treatment planning system (TPS) has a built-in relationship between the monitor unit (MU) and the dose. But, the exact type of relationship is quite difficult to ascertain. However, some obvious knowledge about the monitor chamber behaviour has motivated building a few models to analyse the dosimetry behaviour for proton beams. As the monitor chamber is graphite or an air-filled chamber,

which will have dependency proportional to the stopping power S of the beam energy.

$$MU \propto S \tag{5.6}$$

Based on information from PSTAR stopping power and range table (see figure 5.4) presented by the National Institute of Standards and Technology (NIST) [3] for protons in the range 70 MeV to 200 MeV, it is reasonable to approximate that the stopping power decreases exponenetially with an increase in energy of the particles:

$$S \propto E^{-\mathrm{a}}, \tag{5.7}$$

$$\mathrm{a} = 0...1$$

Therefore,

$$MU \propto E^{-\mathrm{a}} \tag{5.8}$$

It is a very simple model of an ion chamber S indicates the stopping power, where E is the beam energy beam energy and a is determined by using the line of best fit. The a was found to be $a = 0.72$ by using the PSTAR data in the proton beam range from 70 MeV to 200 MeV.

All nineteen ASCII files from FLUKA output which contained dose deposition information exported into MATLAB. A script was written to generate a three-dimensional dose matrix (see F.1) having dimensions similar to the TPS generated dose matrix ($159 \times 159 \times 80$). A two-dimensional spread out Bragg peak was plotted in MATLAB. To check the non-uniformity in SOBP, a linear regression method was employed and equation 5.5 is used for all three monitor unit calculation models.

Initially, the monitor units were assumed to be equal to the amount of energy deposited in the homogeneous water phantom. The calculated non-uniformity in the dose profile is 3.25% which is large for this benchmark. It has been presumed that for accurate uniformity somewhere in between is a dependence on $E^{-\mathrm{a}}$ where, a is between 0 and 1. Therefore, the monitor units were calculated by using the following two models. For the MATLAB code, used to plot the SOBP (see appendices B.1).

$$MU \propto E^{-0.5} \tag{5.9}$$

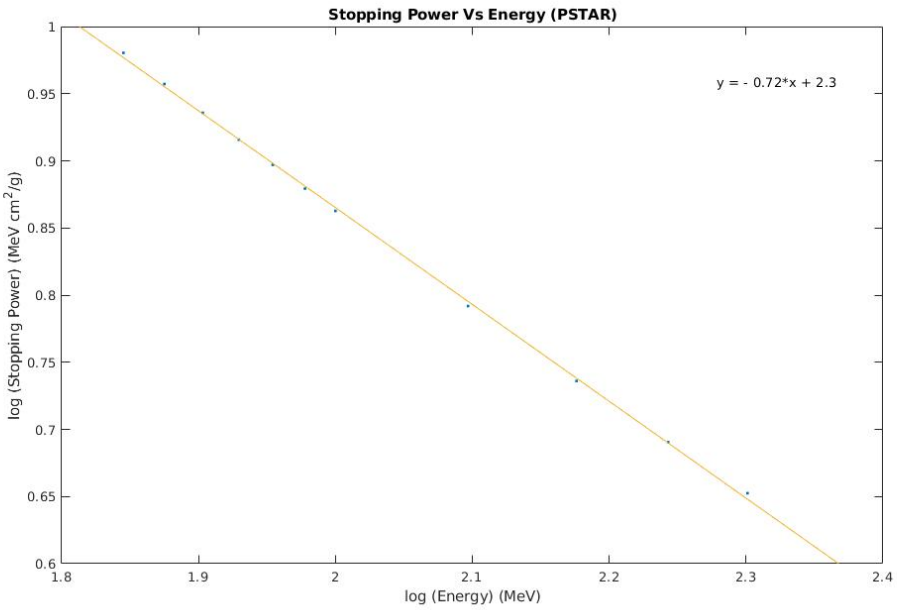

Figure 5.4: PSTAR: A graph of PSTAR relationship between stopping power and energy of protons ranging from 70 MeV to 200 MeV.

and

$$MU \propto E^{-1} \tag{5.10}$$

These calculated values were employed to generate the spread out Bragg peaks and the flatness was computed using equation 5.5.

The percentage beam non-uniformity calculated for MU calculation model, $MU = E^{-1/2}$ is 0.155%. Figure 5.5 elaborates this beam flatness. According to AAPM task groups TG-40 and TG-142 recommendations for mega voltage photon beams, the flatness and beam quality should be constrained within ±2% (TG-40) and ±1% (TG-142) of the established values used for commissioning of treatment planning system (TPS) [106]. The beam homogeneity has also been calculated for the SOBP drawn for MU=E^{-1} and the calculated beam flatness is 2.67%.

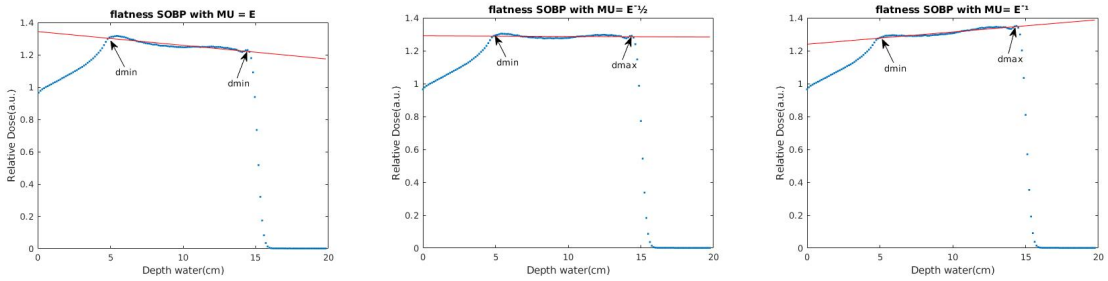

(a) for MU=E^0. *(b) for MU=$E^{-1/2}$.* *(c) for MU=E^{-1}.*

Figure 5.5: Flatness of spread out Bragg peak (SOBP) in water phantom at 5cm depth calculated for three different MU calculation models.

Dose Flatness in Graphite

For Monte Carlo simulations, the phantom material is replaced with graphite to check the dose uniformity for different materials under same conditions and for the same set of beam energies. In order to calculate the dose flatness for graphite, the same procedure is repeated

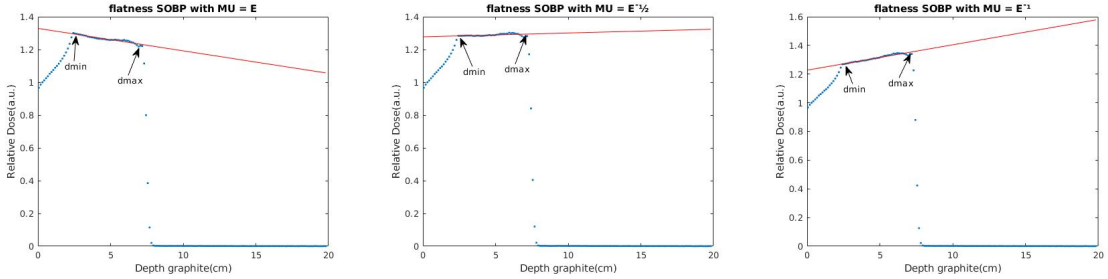

(a) for MU=E. *(b) for MU=$E^{-1/2}$.* *(c) for MU=E^{-1}.*

Figure 5.6: Flatness of spread out Bragg peak (SOBP) in graphite phantom at 5cm depth calculated for three different MU calculation models.

as for water and non-uniformity values are obtained. Assuming $MU = E$, the dose non-uniformity is recorded as 2.493% while this value is 0.426% for $E^{-1/2}$ and for $MU = E^{-1}$ model, the calculated value for dose flatness is 3.198%.

Medium	non-uniformity for MU=E	non-uniformity for MU=$E^{-1/2}$	non-uniformity for MU=E^{-1}
Water	3.25%	0.155%	2.67%
Graphite	2.493%	0.426%	3.198%

Table 5.2: Percentage dose non-uniformity values calculated by using three different MU calculation models for water and graphite.

SOBP Comparison

After the determination of the best model, the FLUKA-based simulation outcomes were justified against dedicated data obtained from the Eclipse treatment planning system (TPS) for a range of 15.38 cm and a modulation of 10 cm. The spread out Bragg peak (SOBP) generated by FLUKA for a set of 19 different beam energies is compared to the data from Eclipse TPS in figure 5.7 (arbitrary units were used to normalise the data in the SOBP region). The simulation data has very good correspondence with the treatment planning

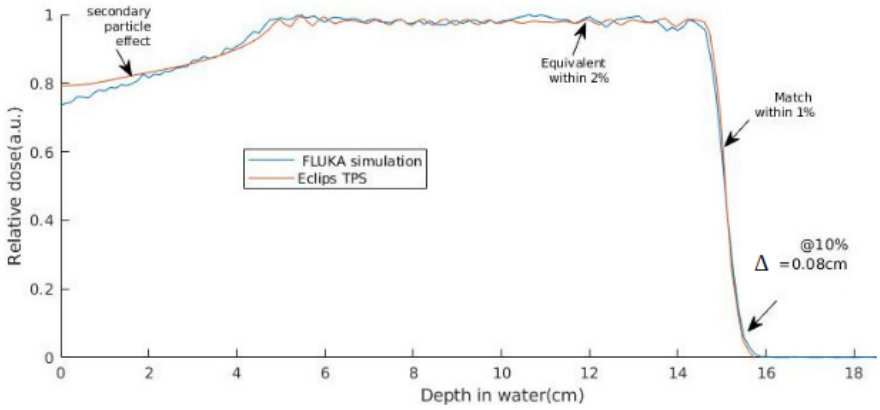

Figure 5.7: Comparison of SOBP's generated from FLUKA simulation and TPS data for a modulation of 10 cm. The distributions are normalised in the SOBP region.

system generated data. From figure 5.7, the data analysis shows that from the beginning to the end of the SOBP, the data points match within 2%. A noticeable difference between simulation and TPS data has been observed, which is due to the effect of the differing amounts of secondary particles generation, a consequence of the difference of beam alignment between

the simplistic FLUKA simulation and the Eclipse treatment planning system. At the distal 10% dose end, a depth difference of 0.08 cm has been observed.

Gamma Analysis

The USRBIN card in FLUKA scores the distribution of one of several quantities in a regular spatial structure (binning detector) independent from the geometry [102]. Using the $MU = E^{-1/2}$ model, the USRBIN card was inserted in each input file with 125 bins (each of them 0.125 cm wide) in the beam direction to score the amount of energy deposited per unit mass in the Phantom. The USRBIN output information from FLUKA is exported into MATLAB for post-processing. An algorithm is developed to extract dose deposited in the whole Phantom and then to write this information as a 3D DICOM file with all necessary data required to generate a treatment plan. The dose is normalised at the centre of the SOBP of the TPS plan. This dose matrix is then replaced with the TPS RD.dcm (dose) file. All the data from the RD.dcm is imported into CERR to generate a new TPS plan, based on the simulation outcomes. CERR is designed to insert more than one treatment plan at a time and provide a facility to the user to perform a gamma analysis for the dose. This feature is then used to analyse the gamma index for the TPS and FLUKA generated plans. The PTV-High was the primary target volume and following the standard depth dose criteria the TPS plan was generated with an aim to deliver the 95% of the dose to the 100% of PTV-High (target volume). For gamma (γ) analysis, with an ambition to achieve 95% pass rate, the dose difference parameter was set to 3% and distance to agreement (DTA) parameter was defined at 3 mm. This DD/DTA combination is clinically applied at most of the radiotherapy centres for gamma assessment [18, 107].

5.8 Discussion

The Eclipse proton therapy treatment planning system at Singleton Hospital is available for research purposes, it only contains certain experimental Golden Data information for dose calculations. Golden data is the experimentally derived data we have been attempted to model in this project. A fundamental of the characteristics of the proton acceleration

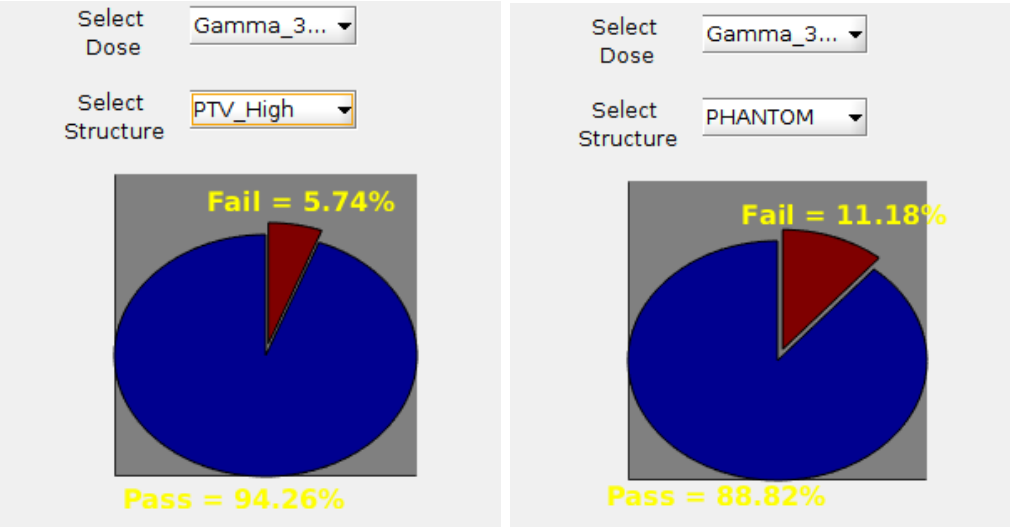

(a) γ-index PTV-HIGH. *(b) γ-index PHANTOM.*

Figure 5.8: Results for gamma analysis with 3% 3 mm gamma passing criteria [18].

monitoring system is ionization chamber, a relationship between the monitor units (MU) and stopping powers has been defined to analyse the dosimetric dependence of the proton beams. It has been concluded that $MU = E^{-1/2}$ is the best weighting function to achieve the dose uniformity expected from TPS. The relationship does not precisely relate to the variations of stopping power.

After the modelling with the FLUKA Monte Carlo code it has been observed that the dose uniformity is good for water and also the non-uniformity in graphite is not drastic. It is actually reasonably acceptable and that means the practice of creating beams using the same material as water will be acceptable for recalculating plans for the irradiation of the graphite calorimeter because the flatness in this case is 0.5 %.

For gamma analysis, the general passing criteria is 95%. For PTV-HIGH (primary volume) this is very close to 95%, but for PHANTOM the outcomes are out of tolerance and clinically unacceptable. This is because of the several limitations of the study including that the ion chamber has not been explicitly modeled. Knowledge about spot positions and weighting factors is essential to run MC simulations over the whole of the phantom accurately. However, for this work a square field of 10 $\times$ 10 cm^2 has been used. Despite these limitations, the study gives confidence to the use of TPS in the preparation of fields for

calorimetry experiments.

The next chapter gives a brief description of the work presented in this thesis and the future directions to extend further research in the field of the proton beam therapy.

Chapter 6

Summary

This final chapter summarises the main results and outcomes of the work described in this thesis and discusses some possible future work to continue what has been achieved so far. This work aims to investigate the presence of range uncertainties in proton therapy beams when they penetrate through the sub-millimeter-sized heterogeneities. The effect of Bragg peak degradation has been demonstrated in bone models with the FLUKA Monte Carlo code and experimental measurements with a 36 MeV proton beam.

6.1 Range Uncertainties in Brain Proton Therapy

A female flat skull bone is modelled in FLUKA to simulate the proton beam in order to estimate the range uncertainties associated with sub-CT resolution heterogeneities in the path of the beam. The effect on the range of a 100 MeV proton beam is examined, simulating typical proton therapy of the brain. Chapter 3 describes all the procedures an methods adopted to complete this work. In particular, the model simulates the practice of using the flat skull bone as an entrance surface as opposed to traversing more complex and thick bones of the skull. The overall thickness of the bone was 7.1 mm and the trabecular layer was 2.3 mm. The dimensions of the voxels in the micro-CT data was manipulated to simulate variations in trabecular pore size, from approximately 0.4 to 4 mm diameter. The proton beam was square field of 4×4 mm^2, which therefore, traversed many pores at one extreme and fewer pores for larger voxel sizes. Random sampling of the region was taken from the bone substi-

tute and employed to obtain the statistical variation in the texture. The range of the proton beam and the spread of the Bragg peak was determined and examined as a function of pore size. The average range was found to vary by 0.08 mm, with an $R^2 = 0.07$, suggesting that only a small part of the variation was demonstrated to be systematic. The results therefore confirm that sub CT heterogeneity is unlikely to result in significant uncertainties, given the practice of irradiating through flat bone; however, for a larger thickness of trabecular bone, e.g. greater than 20 mm, range uncertainties of the order of 1 mm may be present.

This work has sound no major problems for the proton beam therapy in terms of scattering in the flat skull bone. This has not been previously reported in the literature; therefore, these outcomes support the normal proton therapy practice of treating through the thin, flat bone.

6.2 FLUKA Benchmark of Experimental Data

The main purpose of this work was to quantify range uncertainties related with proton beams due to sub-CT structures of variable density material, present in the path of the beam. This project was designed to perform an experiment to delineate range uncertainties when a 36 MeV proton beam penetrates through a porous material of variable densities. Five SAWBONES® foam-block phantoms of different densities were used to ascertain the effect of heterogeneous structures on the range of the proton beam. FLUKA simulations were run to benchmark the correspondence between experimental and MC results. The experiment was performed twice as on the first attempt there were few discrepancies found in the methodology. These discrepancies were addressed appropriately and expected results were successfuly obtained from experiment on second attempt. For a detailed description about these experiments and FLUKA simulations see chapter 4 .

The results obtained from experiment were plotted against those from both sets of FLUKA simulations. Figure 4.24 shows trends for all samples as observed in the original experiment versus results from FLUKA. It has been observed that the variance increased with an increase in the foam density. This experimental benchmark reveals a similar trend in the variations of the range of protons penetrating through foam samples with variable

density. It can also be seen that the magnitude of the effect for experimental datasets is larger compared to those from FLUKA output. The film for each set of foam samples was exposed at three different locations to see the effect of beam path variation as well. These larger error bars authenticate the passage of the beam through different paths in the foam such as air pockets and joints present in the foam samples. As the protons scatter they change their directions; an effect that exaggerates the variations in the range.

The Monte Carlo modelling backs up the experimental data and gives similar features to the experiment. AS quenching of the film response in the Bragg Peak; therefore an attempt was made to model this effect in FLUKA; however small variations were evident.

6.3 Monte Carlo Benchmark of Eclipse Golden Data

The characteristics of FLUKA were benchmarked against the Eclipse golden data for proton therapy. Chapter 5 gives an in-depth information about the whole process. A Monte Carlo analytical was developed to recalculate the dose distributions, originally obtained for a $10 \times 10 \times 10$ cm^3 water-filled box. Golden data is the experimentally derived data which we have attempted to model in this project. The fundamental behaviour of monitor chamber (used for dosimetry) and PSTAR stopping power and range table has motivated the development of a relationship between the energy and monitor unit of the particles. This MU calculation model is then utilised to clculate and compare the dose non-uniformity in different materials such as water and graphite.

After making calculations with this model, MU$=E^{-1/2}$, the dose non-uniformity in water and graphite material was recorded as 0.155% and 0.426% for water and graphite phantom respectively. After the modelling it has been observed that the dose uniformity is good for water and the non-uniformity in graphite is acceptable, which means the practice of creating beams using the same material as water will be acceptable for determining plans for the irradiation of the graphite calorimeter.

6.4 Potential Improvements and Future Work

There is significant scope for work building upon the results of this thesis. Although the proton therapy is becoming widely available in developed countries, the issue of range uncertainty is still a question that needs a urgent attention. This overall project was designed to find the range uncertainties associated with sub-CT resolution heterogeneities present in the path of the proton beam. Micro-CT scan of SAWBONES® foam-block phantoms were used in FLUKA to develop an analytical female flat skull bone model and to employ the range uncertainties in a 100 MeV beam on its penetration through the bone. The results obtained for this thin part of the bone support the treatment of brain tumors through flat skull bone. However, more work could be done in future to determine the uncertainties in proton range within the deeper bone such as the skull base and femoral head.

Moreover, an experiment has been performed at Birmingham University low energy proton beam line. A 36 MeV beam is used to observe the range uncertainties in the beam when it penetrates through bone of variable densities. The Monte Carlo modelling gives similar features to the physical experiment and shows a trend in the variations in proton beam range when it pass through the bone. These findings indicicates an urgent requirement to perform this experiment at therapeutic beam range (70 to 250 MeV) to better evaluate the range uncertainty when treatment planning for proton therapy.

Bibliography

[1] M. M. Ladra and T. I. Yock, "Proton radiotherapy for pediatric sarcoma," *Cancers*, vol. 6, no. 1, pp. 112–127, 2014.

[2] W. D. Newhauser and R. Zhang, "The physics of proton therapy," *Physics in medicine and biology*, vol. 60, no. 8, p. R155, 2015.

[3] P. M. Laboratory, "Stopping-power & range tables for electrons, protons, and helium ions." NIST Standard Reference Database 124, 2017.

[4] H. Paganetti, "Range uncertainties in proton therapy and the role of monte carlo simulations," *Physics in medicine and biology*, vol. 57, no. 11, p. R99, 2012.

[5] H. Owen, A. Lomax, and S. Jolly, "Current and future accelerator technologies for charged particle therapy," *Nuclear Instruments and Methods in Physics Research Section A: Accelerators, Spectrometers, Detectors and Associated Equipment*, vol. 809, pp. 96–104, 2016.

[6] F. M. Khan and J. P. Gibbons, *Khan's the physics of radiation therapy*. Lippincott Williams & Wilkins, 2014.

[7] Christie, "How proton beam therapy is delivered." `https://www.christie.nhs.uk/patients-and-visitors/services/protons/what-is-proton-beam-therapy/how-proton-beam-therapy-is-delivered`, 2019.

[8] D. Wang, "A critical appraisal of the clinical utility of proton therapy in oncology," *Medical devices (Auckland, NZ)*, vol. 8, p. 439, 2015.

[9] B. Pehlivan, E. Topkan, and A. Yavuz, "Klinik proton terapi uygulamaları," *Ege Tıp Dergisi*, vol. 50, no. 1, pp. 1–6, 2011.

[10] A. Lomax, "Intensity modulation methods for proton radiotherapy," *Physics in Medicine & Biology*, vol. 44, no. 1, p. 185, 1999.

[11] A. Lomax, "Intensity modulated proton therapy and its sensitivity to treatment uncertainties 1: the potential effects of calculational uncertainties," *Physics in Medicine & Biology*, vol. 53, no. 4, p. 1027, 2008.

[12] L. Crampton, "Interesting and Surprising Facts About the Human Skeleton." `https://owlcation.com/stem/Interesting-and-Surprising-Facts-About-the-Human-Skeleton/`, 2017.

[13] D. Shier, J. Butler, and R. Lewis, *Hole's human anatomy and physiology*. McGraw-Hill Education, 2015.

[14] E. M. Lillie, J. E. Urban, S. K. Lynch, A. A. Weaver, and J. D. Stitzel, "Evaluation of skull cortical thickness changes with age and sex from computed tomography scans," *Journal of Bone and Mineral Research*, vol. 31, no. 2, pp. 299–307, 2016.

[15] Y. Dong, X. Liu, T. Song, and S. He, "Topology optimization for structure with multi-gradient materials," *Structural and Multidisciplinary Optimization*, vol. 63, no. 3, pp. 1151–1167, 2021.

[16] R. Castriconi, "Response of EBT3 radiochromic film dosimeters to proton and carbon ion hadrontherapy beams," 2015.

[17] M. Wendling, L. J. Zijp, L. N. McDermott, E. J. Smit, J.-J. Sonke, B. J. Mijnheer, and M. van Herk, "A fast algorithm for gamma evaluation in 3d," *Medical physics*, vol. 34, no. 5, pp. 1647–1654, 2007.

[18] T. Tessonnier, A. Mairani, F. Cappucci, A. Mirandola, G. V. Freixas, S. Molinelli, M. Donetti, and M. Ciocca, "Development and application of tools for monte carlo

based simulations in a particle beam radiotherapy facility," *Applied Radiation and Isotopes*, vol. 83, pp. 155–158, 2014.

[19] C. Karger, O. Jäkel, H. Palmans, and T. Kanai, "Dosimetry for ion beam radiotherapy," *Physics in medicine and biology*, vol. 55, pp. R193–234, 10 2010.

[20] J. D. Zindler, J. Thomas, Charles R., S. M. Hahn, A. L. Hoffmann, E. G. Troost, and P. Lambin, "Increasing the Therapeutic Ratio of Stereotactic Ablative Radiotherapy by Individualized Isotoxic Dose Prescription," *JNCI: Journal of the National Cancer Institute*, vol. 108, 10 2015.

[21] K. Cheung, "Intensity modulated radiotherapy: advantages, limitations and future developments," *Biomed Imaging Interv J*, vol. 2, no. 1, p. e19, 2006.

[22] G. Roopashri and M. Baig, "Current advances in radiotherapy of head and neck malignancies," *Journal of international oral health: JIOH*, vol. 5, no. 6, p. 119, 2013.

[23] J. R. Carver, C. L. Shapiro, A. Ng, L. Jacobs, C. Schwartz, K. S. Virgo, K. L. Hagerty, M. R. Somerfield, and D. J. Vaughn, "American society of clinical oncology clinical evidence review on the ongoing care of adult cancer survivors: cardiac and pulmonary late effects," *Journal of Clinical Oncology*, vol. 25, no. 25, pp. 3991–4008, 2007.

[24] A. K. Bryant, M. P. Banegas, M. E. Martinez, L. K. Mell, and J. D. Murphy, "Trends in radiation therapy among cancer survivors in the united states, 2000–2030," *Cancer Epidemiology and Prevention Biomarkers*, vol. 26, no. 6, pp. 963–970, 2017.

[25] S. Doyle-Lindrud, "Proton beam therapy for pediatric malignancies.," *Clinical journal of oncology nursing*, vol. 19, no. 5, pp. 521–523, 2015.

[26] P. N. McDermott, *Tutorials in radiotherapy physics*. Taylor and Francis, 2016.

[27] S. M. MacDonald, T. F. DeLaney, and J. S. Loeffler, "Proton beam radiation therapy," *Cancer Investigation*, vol. 24, no. 2, pp. 199–208, 2006. PMID: 16537190.

[28] M. Goitein and M. Jermann, "The relative costs of proton and x-ray radiation therapy," *Clinical Oncology*, vol. 15, no. 1, pp. S37–S50, 2003.

[29] T. Mitin and A. L. Zietman, "Promise and pitfalls of heavy-particle therapy," *Journal of Clinical Oncology*, vol. 32, no. 26, pp. 2855–2863, 2014.

[30] M. Jermann, "Particle therapy statistics in 2014," *International Journal of Particle Therapy*, vol. 2, no. 1, pp. 50–54, 2015.

[31] D. R. Olsen, Ø. S. Bruland, G. Frykholm, and I. N. Norderhaug, "Proton therapy–a systematic review of clinical effectiveness," *Radiotherapy and oncology*, vol. 83, no. 2, pp. 123–132, 2007.

[32] D. Schulz-Ertner and H. Tsujii, "Particle radiation therapy using proton and heavier ion beams," *Journal of clinical oncology*, vol. 25, no. 8, pp. 953–964, 2007.

[33] H. Paganetti and H. Kooy, "Proton radiation in the management of localized cancer," *Expert review of medical devices*, vol. 7, no. 2, pp. 275–285, 2010.

[34] S. Tavernier, "Interactions of particles in matter," in *Experimental techniques in nuclear and particle physics*, pp. 23–53, Springer, 2009.

[35] F. H. Attix, *Introduction to radiological physics and radiation dosimetry*. John Wiley & Sons, 2008.

[36] A. J. Lomax, "Charged particle therapy: the physics of interaction," *The Cancer Journal*, vol. 15, no. 4, pp. 285–291, 2009.

[37] B. Jia, A. A. Mowlavi, M. H. Hadizadeh Yazdi, and M. Ebrahimi, "Impact of range straggling and multiple scattering on proton therapy of brain, using a slab head phantom," *International Journal of Radiation Research*, vol. 12, 2014.

[38] W. Wieszczycka and W. H. Scharf, *Proton radiotherapy accelerators*. World Scientific, 2001.

[39] T. J. Pugh and A. K. Lee, "Proton beam therapy for the treatment of prostate cancer," *The Cancer Journal*, vol. 20, no. 6, pp. 415–420, 2014.

[40] F. Albertini, S. Gaignat, M. Bosshardt, and A. J. Lomax, "Planning and optimizing treatment plans for actively scanned proton therapy," *Biomedical Mathematics: Promising Directions in Imaging, Therapy Planning, and Inverse Problems (ed 1). Madison: Medical Physics Pub Corp*, pp. 1–18, 2009.

[41] S. Dieterich, E. Ford, D. Pavord, and J. Zeng, *Practical Radiation Oncology Physics E-Book: A Companion to Gunderson & Tepper's Clinical Radiation Oncology*. Elsevier Health Sciences, 2015.

[42] R. Jena, "Preparing for proton therapy," *Clinical Oncology*, vol. 30, no. 5, pp. 269–270, 2018.

[43] N. F. Trust, "The Clatterbridge Cancer Centre." `https://www.clatterbridgecc.nhs.uk/patients/treatment-and-support/proton-therapy/proton-therapy-information-sheet`, 2018.

[44] I. REPORT, "I made the right decision, says first patient to have proton beam therapy in uk," 10 July 2018.

[45] A. Crellin, "The road map for national health service proton beam therapy," *Clinical Oncology*, vol. 30, no. 5, pp. 277–279, 2018.

[46] C. Toramatsu, N. Katoh, S. Shimizu, H. Nihongi, T. Matsuura, S. Takao, N. Miyamoto, R. Suzuki, K. Sutherland, R. Kinoshita, *et al.*, "What is the appropriate size criterion for proton radiotherapy for hepatocellular carcinoma? a dosimetric comparison of spot-scanning proton therapy versus intensity-modulated radiation therapy," *Radiation Oncology*, vol. 8, no. 1, pp. 1–8, 2013.

[47] A. Zurlo, A. Lomax, A. Hoess, T. Bortfeld, M. Russo, G. Goitein, V. Valentini, L. Marucci, R. Capparella, and A. Loasses, "The role of proton therapy in the treatment of large irradiation volumes: a comparative planning study of pancreatic and biliary tumors," *International Journal of Radiation Oncology Biology Physics*, vol. 48, no. 1, pp. 277–288, 2000.

[48] E. J. Hall, "Intensity-modulated radiation therapy, protons, and the risk of second cancers," *International Journal of Radiation Oncology Biology Physics*, vol. 65, no. 1, pp. 1–7, 2006.

[49] M. Moteabbed, T. I. Yock, and H. Paganetti, "The risk of radiation-induced second cancers in the high to medium dose region: a comparison between passive and scanned proton therapy, imrt and vmat for pediatric patients with brain tumors," *Physics in Medicine & Biology*, vol. 59, no. 12, p. 2883, 2014.

[50] M. Goitein, "The measurement of tissue heterodensity to guide charged particle radiotherapy," *International Journal of Radiation Oncology Biology Physics*, vol. 3, pp. 27–33, 1977.

[51] G. O. Sawakuchi, U. Titt, D. Mirkovic, and R. Mohan, "Density heterogeneities and the influence of multiple coulomb and nuclear scatterings on the bragg peak distal edge of proton therapy beams," *Physics in Medicine & Biology*, vol. 53, no. 17, p. 4605, 2008.

[52] S. España and H. Paganetti, "Uncertainties in planned dose due to the limited voxel size of the planning ct when treating lung tumors with proton therapy," *Physics in medicine and biology*, vol. 56, no. 13, p. 3843, 2011.

[53] A. Carabe, M. Moteabbed, N. Depauw, J. Schuemann, and H. Paganetti, "Range uncertainty in proton therapy due to variable biological effectiveness," *Physics in Medicine & Biology*, vol. 57, no. 5, p. 1159, 2012.

[54] M. Urie, M. Goitein, W. Holley, and G. T. Chen, "Degradation of the bragg peak due to inhomogeneities," *Physics in Medicine & Biology*, vol. 31, no. 1, p. 1, 1986.

[55] K. M. Kurian, M. D. Jenkinson, P. M. Brennan, R. Grant, S. Jefferies, A. G. Rooney, H. Bulbeck, S. C. Erridge, S. Mills, C. McBain10, *et al.*, "Brain tumor research in the uk: current perspective and future challenges,"

[56] C. UK, "Childhood Cancer Facts and Figures." `https://www.childrenwithcancer.org.uk/childhood-cancer-info/childhood-cancer-facts-figures/`, 2018.

[57] CBTRUS, "2018 CBTRUS Central Brain Tumor Registry of the United States, Fact Sheet." http://www.cbtrus.org/factsheet/factsheet.html/, 2018.

[58] H. Paganetti, *Proton therapy physics*. CRC press, 2016.

[59] G. O. Sawakuchi, U. Titt, D. Mirkovic, and R. Mohan, "Density heterogeneities and the influence of multiple coulomb and nuclear scatterings on the bragg peak distal edge of proton therapy beams," *Physics in Medicine & Biology*, vol. 53, no. 17, p. 4605, 2008.

[60] U. Titt, M. Sell, J. Unkelbach, M. Bangert, D. Mirkovic, U. Oelfke, and R. Mohan, "Degradation of proton depth dose distributions attributable to microstructures in lung-equivalent material," *Medical physics*, vol. 42, no. 11, pp. 6425–6432, 2015.

[61] M. Urie, M. Goitein, W. R. Holley, and G. T. Y. Chen, "Degradation of the bragg peak due to inhomogeneities," *Physics in Medicine & Biology*, vol. 31, no. 1, p. 1, 1986.

[62] K.-S. Baumann, M. Witt, U. Weber, R. Engenhart-Cabillic, and K. Zink, "An efficient method to predict and include bragg curve degradation due to lung-equivalent materials in monte carlo codes by applying a density modulation," *Physics in Medicine & Biology*, vol. 62, no. 10, p. 3997, 2017.

[63] B. Clarke, "Normal bone anatomy and physiology," *Clinical journal of the American Society of Nephrology*, vol. 3, no. Supplement 3, pp. S131–S139, 2008.

[64] D. Shier, J. Butler, and R. Lewis, *Human anatomy and physiology*. McGraw-Hill Boston, MA, USA, 2001.

[65] A. Ferrari, P. R. Sala, A. Fasso, and J. Ranft, "Fluka: A multi-particle transport code (program version 2005)," tech. rep., 2005.

[66] G. Battistoni, J. Bauer, T. T. Boehlen, F. Cerutti, M. P. Chin, R. Dos Santos Augusto, A. Ferrari, P. G. Ortega, W. Kozłowska, G. Magro, *et al.*, "The fluka code: an accurate simulation tool for particle therapy," *Frontiers in oncology*, vol. 6, p. 116, 2016.

[67] V. Andersen, F. Ballarini, G. Battistoni, M. Campanella, M. Carboni, F. Cerutti, A. Empl, A. Fasso, A. Ferrari, E. Gadioli, *et al.*, "The fluka code for space applications: recent developments," *Advances in Space Research*, vol. 34, no. 6, pp. 1302–1310, 2004.

[68] F. Ballarini, M. Biaggi, L. De Biaggi, A. Ferrari, A. Ottolenghi, A. Panzarasa, H. Paretzke, M. Pelliccioni, P. Sala, D. Scannicchio, *et al.*, "Role of shielding in modulating the effects of solar particle events: Monte carlo calculation of absorbed dose and dna complex lesions in different organs," *Advances in Space Research*, vol. 34, no. 6, pp. 1338–1346, 2004.

[69] V. Vlachoudis *et al.*, "Flair: a powerful but user friendly graphical interface for fluka," in *Proc. Int. Conf. on Mathematics, Computational Methods & Reactor Physics (M&C 2009), Saratoga Springs, New York*, 2009.

[70] V. Vlachoudis and D. Sinuela-Pastor, "Numerically robust geometry engine for compound solid geometries," in *SNA+ MC 2013-Joint International Conference on Supercomputing in Nuclear Applications+ Monte Carlo*, p. 02502, EDP Sciences, 2014.

[71] G. Battistoni, T. Boehlen, F. Cerutti, P. W. Chin, L. S. Esposito, A. Fassò, A. Ferrari, A. Lechner, A. Empl, A. Mairani, *et al.*, "Overview of the fluka code," *Annals of Nuclear Energy*, vol. 82, pp. 10–18, 2015.

[72] G. Battistoni, F. Broggi, M. Brugger, M. Campanella, M. Carboni, A. Empl, A. Fassò, E. Gadioli, F. Cerutti, A. Ferrari, *et al.*, "Applications of fluka monte carlo code for nuclear and accelerator physics," *Nuclear Instruments and Methods in Physics Research Section B: Beam Interactions with Materials and Atoms*, vol. 269, no. 24, pp. 2850–2856, 2011.

[73] S. USA, "Sawbones general catalog." A Pacific Research Company, 2018.

[74] L. De Marzi, C. Lesven, R. Ferrand, J. Sage, T. Boulé, and A. Mazal, "Calibration of ct hounsfield units for proton therapy treatment planning: use of kilovoltage and megavoltage images and comparison of parameterized methods," *Physics in Medicine & Biology*, vol. 58, no. 12, p. 4255, 2013.

[75] W. Schneider, T. Bortfeld, and W. Schlegel, "Correlation between ct numbers and tissue parameters needed for monte carlo simulations of clinical dose distributions," *Physics in Medicine & Biology*, vol. 45, no. 2, p. 459, 2000.

[76] A. V. Chvetsov and S. L. Paige, "The influence of ct image noise on proton range calculation in radiotherapy planning," *Physics in Medicine & Biology*, vol. 55, no. 6, p. N141, 2010.

[77] H. Mahinda and O. Murty, "Variability in thickness of human skull bones and sternum - an autopsy experience," vol. 26, pp. 26–31, 07 2009.

[78] E. Hamed, I. Jasiuk, A. Yoo, Y. Lee, and T. Liszka, "Multi-scale modelling of elastic moduli of trabecular bone," *Journal of The Royal Society Interface*, 2012.

[79] O. T. Williams, "The use of fine-structure spectroscopy techniques in determining proton range uncertainties," Master's thesis, School of Medicine, 2018.

[80] D. J. Kirby, *Radiation dosimetry of conventional and laser-driven particle beams*. PhD thesis, University of Birmingham, 2011.

[81] P. Pellicioli, S. Bartzsch, M. Donzelli, M. Krisch, and E. Bräuer-Krisch, "High resolution radiochromic film dosimetry: Comparison of a microdensitometer and an optical microscope," *Physica Medica*, vol. 65, pp. 106–113, 2019.

[82] C. N. Kimball-Smith, "Modelling the range uncertainty of protons in lung tissue with fluka," Master's thesis, Swansea University, 2018.

[83] M. J. Butson, K. Peter, T. Cheung, and P. Metcalfe, "Radiochromic film for medical radiation dosimetry," *Materials Science and Engineering: R: Reports*, vol. 41, no. 3-5, pp. 61–120, 2003.

[84] D. I. Thwaites, B. Mijnheer, and J. A. Mills, "Quality assurance of external beam radiotherapy," *International Atomic Energy Agency (IAEA). Radiation oncology physics: a handbook for teachers and students. Vienna, Austria: IAEA*, pp. 407–50, 2005.

[85] P. Andreo, D. T. Burns, K. Hohlfeld, M. S. Huq, T. Kanai, F. Laitano, V. Smyth, and S. Vynckier, "Absorbed dose determination in external beam radiotherapy: an international code of practice for dosimetry based on standards of absorbed dose to water," *IAEA TRS*, vol. 398, 2000.

[86] L. M. Petrie, *Characterisation of a Graphite Calorimeter in Scanned Proton Beams*. PhD thesis, University of Surrey (United Kingdom), 2016.

[87] BIPM, "Summary Results of BIPM.RI(I)-K4." `http://kcdb.bipm.org/AppendixB/appbresults/bipm.ri(i)-k4/bipm`, 2016. [Online; accessed 15 July 2018].

[88] BBCNews, "Proton beam cancer treatment to start in Manchester in 2018." `https://www.bbc.co.uk/news/health-42446686`, 6 January 2018 2018.

[89] PTGOC, "Particle therapy facilities under construction (update january 2017)." `https://www.ptcog.ch/index.php/facilities-under-construction`.

[90] S. Mattsson and C. Hoeschen, *Radiation Protection in Nuclear Medicine*. Springer Berlin Heidelberg, 2012.

[91] ICRU-Report78, "4dosimetry," *Journal of the International Commission on Radiation Units and Measurements*, vol. 7, no. 2, pp. 49–81, 2007.

[92] C. K. Ross and N. V. Klassen, "Water calorimetry for radiation dosimetry," *Physics in Medicine & Biology*, vol. 41, no. 1, p. 1, 1996.

[93] M. R. McEwen and A. R. DuSautoy, "Primary standards of absorbed dose for electron beams," *Metrologia*, 2009.

[94] H. Palmans, R. Thomas, M. Simon, S. Duane, A. Kacperek, A. DuSautoy, and F. Verhaegen, "A small-body portable graphite calorimeter for dosimetry in low-energy clinical proton beams," *Physics in Medicine & Biology*, vol. 49, no. 16, p. 3737, 2004.

[95] A. K. Rath and N. Sahoo, *Particle Radiotherapy: Emerging Technology for Treatment of Cancer*. Springer, 2016.

[96] N. Sahoo, G. O. Sawakuchi, M. T. Gillin, and X. R. Zhu, *Radiation Dosimetry of Proton Beams*, pp. 77–94. New Delhi: Springer India, 2016.

[97] M. McEwen and S. Duane, "A portable calorimeter for measuring absorbed dose in the radiotherapy clinic," *Physics in Medicine & Biology*, vol. 45, no. 12, p. 3675, 2000.

[98] A. R. DuSautoy, "The uk primary standard calorimeter for photon-beam absorbed dose measurement," *Physics in Medicine & Biology*, vol. 41, no. 1, p. 137, 1996.

[99] M. B. T. S. Simon Duane, Hugo Palmans, "Calorimetry," 2007.

[100] D. A. Low, W. B. Harms, S. Mutic, and J. A. Purdy, "A technique for the quantitative evaluation of dose distributions," *Medical physics*, vol. 25, no. 5, pp. 656–661, 1998.

[101] M. Hussein, P. Rowshanfarzad, M. A. Ebert, A. Nisbet, and C. H. Clark, "A comparison of the gamma index analysis in various commercial imrt/vmat qa systems," *Radiotherapy and Oncology*, vol. 109, no. 3, pp. 370–376, 2013.

[102] FLUKATeam, *FLUKA Online manual*. FLUKA Team, 2000-2018.

[103] ICRU-Report78, "Treatment planning," *Journal of the International Commission on Radiation Units and Measurements*, vol. 7, no. 2, pp. 95–122, 2007.

[104] R. Prabhakar, "Dose volume uniformity index: a simple tool for treatment plan evaluation in brachytherapy," *Journal of contemporary brachytherapy*, vol. 2, no. 2, p. 71, 2010.

[105] M. Mrozowska and P. Kukołowicz, "Relationships between various indices of doses distribution homogeneity," *Reports of Practical Oncology & Radiotherapy*, vol. 20, no. 4, pp. 278–283, 2015.

[106] M. Hossain and J. Rhoades, "On beam quality and flatness of radiotherapy megavoltage photon beams," *Australasian physical & engineering sciences in medicine*, vol. 39, no. 1, pp. 135–145, 2016.

[107] D. A. Low and J. F. Dempsey, "Evaluation of the gamma dose distribution comparison method," *Medical physics*, vol. 30, no. 9, pp. 2455–2464, 2003.

Appendix A

MATLAB Codes for Image Processing

Listing A.1: MATLAB code for post-processing raw image data.

```
fid=fopen('C:\Users\Admin\Desktop\richard first ...
    data\150924_microCT_sawbones_blue\Acuitas Polymer ...
    Phantom1_01\Acuitas Polymer Phantom1.raw','r');
A=fread(fid,1063566648,'uint8');
body=reshape(A,1577,969,696);
% imshow(body(:,:,300),[]);
for i=1:1:696
slice=body(:,:,i);
filename=sprintf('uct%010i.dcm',i);
slice_norm=slice/max(max(slice));
dicomwrite(slice_norm,filename);
end
for i = 1:1:696
X = dicomread(sprintf('uct%010i.dcm',i));
metadata = dicominfo('400.dcm');
J = imresize(X,[512 512]);
%dicomwrite(X, ['mct' num2str(i) '.dcm'], metadata, 'CreateMode','Copy')
dicomwrite(J,(sprintf('mct%010i.dcm',i)), metadata, 'CreateMode','Copy');
% dicomwrite(X, ['m1ct' num2str(i) '.dcm'], metadata);
end
%% to make changes in metadata
```

```
B = dicominfo('mct0000000001.dcm');
B.SliceThickness = 0.032616;
B.SpacingBetweenSlices = 0.032616;
B.PixelSpacing = [0.032616;0.032616];
for i = 1:1:696
X = dicomread(sprintf('mct%010i.dcm',i));
B.SliceLocation = 0.032616*i;
J = imresize(X,[1577 969]);
dicomwrite(J,(sprintf('ssct%010i.dcm',i)), B, 'CreateMode','Copy');
end
%%
for i =1:1:696
X = dicomread(sprintf('ssct%010i.dcm',i));
J = imresize(X,[1577 969]);
dicomwrite(J,sprintf('fsct%010i.dcm',i));
end
```

Listing A.2: MATLAB code for editting DICOM image header information

```
% to change the slice thickness of oneslice
A = dicomread('mct1.dcm');
B = dicominfo('mct1.dcm');
B.SliceThickness = 0.032616;
B.SpacingBetweenSlices = 0.032616;
dicomwrite(A,('hct1.dcm'),B,'CreateMode','Copy')
%X = dicomread(sprintf('uct%010i.dcm',i));
%%
image_names = dir('mct*.dcm');
for i = 1:1:10
X = dicomread(image_names(i).name);
B = dicominfo('mct1.dcm');
B.SliceThickness = 0.032616;
B.SpacingBetweenSlices = 0.032616;
B.PixelSpacing = [0.032616;0.032616];
B.SliceLocation = 0.032616*i;
```

```
61 dicomwrite(X,sprintf('ssct%010i.dcm',i),B,'CreateMode','Copy');
62 end
63 %%
64 B = dicominfo('mct0000000001.dcm');
65 B.SliceThickness = 0.032616;
66 B.SpacingBetweenSlices = 0.032616;
67 B.PixelSpacing = [0.032616;0.032616];
68 %here windowwidth and centre values are changed for better image contrast
69 %&brightness
70 B.WindowCenter = [24494;24494];
71 B.WindowWidth = [46090;46090];
72 for i = 1:1:696
73 X = dicomread(sprintf('mct%010i.dcm',i));
74 B.SliceLocation = 0.032616*i;
75 J = imresize(X,[1577 969]);
76 dicomwrite(J,(sprintf('ssct%010i.dcm',i)), B, 'CreateMode','Copy');
77 end
```

Appendix B

MATLAB Code for Plotting the SOBP from FLUKA Output Files

Listing B.1: MATLAB code for plotting the SOBP and checking the non-uniformity

```
numfiles =19;
vals = cell(1,numfiles);
A = dicomread('RN.1.2.246.352.71.5.507863515322.12449.20170322125043.dcm');
RI=dicominfo('RN.1.2.246.352.71.5.507863515322.12449.20170322125043.dcm');
SPw=xlsread('stoppingpowers.xlsx',1,'B5:B23');
for K = 1:19
myfilename = sprintf('file%03d.asc', K);
vals{K} = load(myfilename);
end
dim=size(reshape(vals{1,2}',2022480,1));
RSPw=zeros(dim(1,1),19);
for i=1:1:19
AA= reshape(vals{1,i}',2022480,1);
RSPw(:,i) = RSPw(:,i)+AA/SPw(i);
end
outw = num2cell(RSPw,1);
Dspw = zeros(size(outw{1,1}));
for i = 19:-1:1
```

```
Dspw = Dspw+RI.IonBeamSequence.Item_1.IonControlPointSequence.(['Item_' ...
    num2str( i *2-1)]).ScanSpotMetersetWeights(2).*outw{20-i};
Dspw = Dspw+RI.IonBeamSequence.Item_1.IonControlPointSequence.(['Item_' ...
    num2str( i *2-1)]).ScanSpotMetersetWeights(2).*outw{20-i};
end
S3Dw = reshape(Dspw,159,159,1,80);
figure; imshow(reshape(S3Dw(:,:,1,40),159,159),[])
figure;plot((0:158)*0.586,S3Dw(:,80,1,40))
S = (0:158)*0.586;
T = S3Dw(:,80,1,40);
figure;plot(S,T)
index = (S ≥ 22.85) & (S ≤ 67.98);
p = polyfit(S(index).',T(index),1);
zfit=p(2)+S.*p(1);
figure; plot(S,T,'.');
hold on;
plot(S,zfit,'r');
xlabel('Depth water');
ylabel('Relative Dose');
legend('SOBP with sp',(sprintf('y=%f*x+%f',p(1),p(2))));
index = (S2 ≥ -7.547) & (S2 ≤ -2.767); % -2.484&2.296 are the values ...
    from SOBP for which i have to check the uniformity.
p = polyfit(S2(index),T3(index),1);
zfit=p(2)+S2.*p(1);
figure; plot(S2,T3,'.');
hold on;
plot(S2,zfit,'r');
xlabel('Depth in graphite(cm)');
ylabel('Relative Dose');
legend('SOBP',(sprintf('y=%f*x+%f',p(1),p(2))));
```

Listing B.2: MATLAB code for plotting the proton stopping powers vs energy

```
% to do a plot for stopping powers vs energy for protons (70 MeV to 200MeV)
% values taken from PSTAR and then log is taken for all those values
```

```
3  X = [1.84509804001426 1.8750612633917 1.90308998699194 1.92941892571429 ...
       1.95424250943932 1.97772360528885 2 2.09691001300806 ...
       2.17609125905568 2.24303804868629 2.30102999566398];
4  Y = [0.980412461606891 0.957271979992943 0.935759103745312 ...
       0.915716337945994 0.896966901933155 0.879267956824613 ...
       0.862667950228588 0.791830947674836 0.735997884091794 ...
       0.690461893246178 0.65243974758942];
5  plot(X,Y,'.')
6  xlabel('log (Energy) (MeV)')
7  ylabel ('log (Stopping Power) (MeV cm^2/g)')
8  title('Stopping Power Vs Energy (PSTAR)')
9  % X are energy values
10 % Y are stopping powers
```

Appendix C

MATLAB Codes for Cropping Foam Samples

Listing C.1: MATLAB code for cropping sample 1522-505

```
78 % Slice thickness = 0.0434mm
79 % cropping values
80 % #of pixels required to crop a 2cm by 2cm matrix = (20mm/0.0434mm) 461 ...
       pixels
81 % 461*0.0434 = 20.0074mm or 2.0074cm
82 % dimensions = [1920,1919]
83 lx = ceil(1919/2)-ceil(461/2)+1;
84 ux = ceil(1919/2)+ceil(461/2);
85 ly = ceil(1920/2)-ceil(461/2)+1;
86 uy = ceil(1920/2)+ceil(461/2);
87 % foam 4.44cm thick,44.4mm for 1522-505
88 imagelist = dir('JORDAN*.dcm');
89 [slices,nn] = size(imagelist);
90 for i = 1:slices
91 Jimages = dicomread(imagelist(i).name);
92 Jinfo = dicominfo(imagelist(i).name);
93 copyinf = dicominfo('c1_0001.dcm');
94 copyinf.BitDepth = Jinfo.BitDepth;
```

```
95  copyinf.FileMetaInformationGroupLength = ...
        Jinfo.FileMetaInformationGroupLength;
96  copyinf.MediaStorageSOPClassUID = Jinfo.MediaStorageSOPClassUID;
97  copyinf.MediaStorageSOPInstanceUID = Jinfo.MediaStorageSOPInstanceUID;
98  copyinf.SpacingBetweenSlices = 0.0434;
99  copyinf.SliceThickness = 0.0434;
100 copyinf.SeriesNumber = i+1;
101 copyinf.AcquisitionNumber = i+1;
102 copyinf.SliceLocation = 0.0434*i;
103 copyinf.ImagePositionPatient(3) = copyinf.SliceLocation;
104 copyinf.PixelSpacing = [0.0434;0.0434];
105 copyinf.RescaleSlope = 1;
106 new_img = Jimages(ly:uy,lx:ux);
107 dicomwrite(new_img,(sprintf('505-cropped%04i.dcm',i)),copyinf,'CreateMode'
108 ,'Copy');
109 end
110 image_list=dir('505-cropped*.dcm');
111 [no_slice,nn]=size(image_list);
112 for i=1:no_slice
113 image_dcm=dicomread(image_list(i).name);
114 hdr_dcm = dicominfo(image_list(i).name);
115 % hdr_dcm.PixelSpacing = [0.0434;0.0434];
116 image_dcmm = double(image_dcm);
117 img_hu = (image_dcmm-47)/(256-47)*1024;
118 % img_hu = img_hu.*(img_hu>0)-1024;
119 img_hu = img_hu.*(img_hu>0);
120 dicomwrite(uint16(img_hu), (sprintf('505-scaled%05i.dcm',i)), ...
        hdr_dcm,'CreateMode','Copy')
121 end
122 N = 1066;
123 img_dir = dir('505-scaled*.dcm');
124 img = dicomread(img_dir(1).name);
125 siz_img = size(img);
126 ct3d = NaN([siz_img N]);
127 ct3d(:,:,1) = img;
128 for ii=2:N
```

```
ct3d(:,:,ii)= dicomread(img_dir(ii).name);
end
img_hutest = mean(ct3d,3);
mean(reshape(img_hutest,1,213444))/1024
```

Listing C.2: MATLAB code for cropping sample 1522-524

```
lx = ceil(1919/2)-ceil(461/2)+1;
ux = ceil(1919/2)+ceil(461/2);
ly = ceil(1920/2)-ceil(461/2)+1;
uy = ceil(1920/2)+ceil(461/2);
imagelist = dir('JORDAN*.dcm');
[slices,nn] = size(imagelist);
for i = 1:slices
Jimages = dicomread(imagelist(i).name);
Jinfo = dicominfo(imagelist(i).name);
copyinf = dicominfo('c1_0001.dcm');
copyinf.BitDepth = Jinfo.BitDepth;
copyinf.FileMetaInformationGroupLength = ...
    Jinfo.FileMetaInformationGroupLength;
copyinf.MediaStorageSOPClassUID = Jinfo.MediaStorageSOPClassUID;
copyinf.MediaStorageSOPInstanceUID = Jinfo.MediaStorageSOPInstanceUID;
copyinf.SpacingBetweenSlices = 0.0434;
copyinf.SliceThickness = 0.0434;
copyinf.SeriesNumber = i+1;
copyinf.AcquisitionNumber = i+1;
copyinf.SliceLocation = 0.0434*i+1;
copyinf.ImagePositionPatient(3) = copyinf.SliceLocation;
copyinf.PixelSpacing = [0.0434;0.0434];
copyinf.ImagePositionPatient(3) = copyinf.SliceLocation;
copyinf.PixelSpacing = [0.0434;0.0434];
copyinf.RescaleSlope = 1;
new_img = Jimages(ly:uy,lx:ux);
dicomwrite(new_img,(sprintf('524-cropped%04i.dcm',i)),copyinf,'CreateMode',
'Copy');
```

```
160 end
161 % to make the density of dicom images equivalent to the density of foam
162 % sample rescaling is performed
163 image_list=dir('524-cropped*.dcm');
164 [no_slice,nn]=size(image_list);
165 for i=1:no_slice
166 image_dcm=dicomread(image_list(i).name);
167 hdr_dcm = dicominfo(image_list(i).name);
168 %hdr_dcm.PixelSpacing = [0.0434;0.0434];
169 image_dcmm = double(image_dcm);
170 img_hu = (image_dcmm+35)/(256+35)*1024;
171 % img_hu = img_hu.*(img_hu>0)-1024;
172 img_hu = img_hu.*(img_hu>0);
173 dicomwrite(uint16(img_hu), (sprintf('524-scaled%05i.dcm',i)), ...
       hdr_dcm,'CreateMode','Copy')
174 end
175 img_hutest = mean(ct3d,3);
176 mean(reshape(img_hutest,1,213444))/1024
```

Listing C.3: MATLAB code for cropping sample 1522-526-1

```
177 lx = ceil(1919/2)-ceil(461/2)+1;
178 ux = ceil(1919/2)+ceil(461/2);
179 ly = ceil(1920/2)-ceil(461/2)+1;
180 uy = ceil(1920/2)+ceil(461/2);
181 imagelist = dir('1522-526-1*.dcm');
182 [slices,nn] = size(imagelist);
183 for i = 1:slices
184 Jimages = dicomread(imagelist(i).name);
185 Jinfo = dicominfo(imagelist(i).name);
186 copyinf = dicominfo('c1_0001.dcm');
187 copyinf.BitDepth = Jinfo.BitDepth;
188 copyinf.FileMetaInformationGroupLength = ...
       Jinfo.FileMetaInformationGroupLength;
189 copyinf.MediaStorageSOPClassUID = Jinfo.MediaStorageSOPClassUID;
```

```
copyinf.MediaStorageSOPInstanceUID = Jinfo.MediaStorageSOPInstanceUID;
copyinf.SpacingBetweenSlices = 0.0434;
copyinf.SliceThickness = 0.0434;
copyinf.SeriesNumber = i+1;
copyinf.AcquisitionNumber = i+1;
copyinf.SliceLocation = 0.0434*i+1;
copyinf.ImagePositionPatient(3) = copyinf.SliceLocation;
copyinf.PixelSpacing = [0.0434;0.0434];
copyinf.ImagePositionPatient(3) = copyinf.SliceLocation;
copyinf.PixelSpacing = [0.0434;0.0434];
copyinf.RescaleSlope = 1;
new_img = Jimages(ly:uy,lx:ux);
dicomwrite(new_img,(sprintf('526-cropped%04i.dcm',i)),copyinf,'CreateMode'
,'Copy');
end
% to make the density of dicom images equivalent to the density of foam
% sample rescaling is performed
image_list=dir('526-cropped*.dcm');
[no_slice,nn]=size(image_list);
for i=1:no_slice
image_dcm=dicomread(image_list(i).name);
hdr_dcm = dicominfo(image_list(i).name);
% hdr_dcm.PixelSpacing = [0.0434;0.0434];
image_dcmm = double(image_dcm);
img_hu = (image_dcmm+54)/(256+54)*1024;
% img_hu = img_hu.*(img_hu>0)-1024;
img_hu = img_hu.*(img_hu>0);
dicomwrite(uint16(img_hu), (sprintf('526-scaled%05i.dcm',i)), ...
    hdr_dcm,'CreateMode','Copy')
end
N = 911;
img_dir = dir('526-scaled*.dcm');
%img_dir = dir('526-cropped*.dcm');
img = dicomread(img_dir(1).name);
siz_img = size(img);
ct3d = NaN([siz_img N]);
```

```
225 ct3d(:,:,1) = img;
226 for ii=2:N
227 ct3d(:,:,ii)= dicomread(img_dir(ii).name);
228 end
229 img_hutest = mean(ct3d,3);
230 mean(reshape(img_hutest,1,213444))/1024
```

Appendix D

Monte Carlo Input and Supplementary Files

A large number of FLUKA input filles were used throughout this work and few of them are included here.

Listing D.1: The modifications to the default comscw routines present in the FLUKA usermvax subdirectory.

```
*$ CREATE COMSCW.FOR
*COPY COMSCW
*
*=== comscw ===========================================================*
*
DOUBLE PRECISION FUNCTION COMSCW ( IJ    , XA    , YA    , ZA    ,
&                                  MREG  , RULL  , LLO   , ICALL )

INCLUDE '(DBLPRC)'
INCLUDE '(DIMPAR)'
INCLUDE '(IOUNIT)'
*
*----------------------------------------------------------------------*
*                                                                      *
*     Copyright (C) 1989-2010      by    Alfredo Ferrari & Paola Sala  *
```

```
16 *     All Rights Reserved.                                           *
17 *                                                                    *
18 *                                                                    *
19 *     New comscw for FLUKA9x-20xy                                    *
20 *                                                                    *
21 *     !!!!!!!!!!!!!!!!!!!!!!!!!!!!!!!!!!!!!!!!!!!!!!!!!!!!!!!!!     *
22 *     !!! This is a completely dummy routine for Fluka9x/200x. !!!   *
23 *     !!! The  name has been kept the same as for older  Fluka !!!   *
24 *     !!! versions for back-compatibility, even though  Comscw !!!   *
25 *     !!! is applied only to estimators which didn't exist be- !!!   *
26 *     !!! fore Fluka89.                                        !!!   *
27 *     !!! User  developed versions  can be used for  weighting !!!   *
28 *     !!! density-like quantities at runtime                   !!!   *
29 *     !!!!!!!!!!!!!!!!!!!!!!!!!!!!!!!!!!!!!!!!!!!!!!!!!!!!!!!!!     *
30 *                                                                    *
31 *     Input variables:                                               *
32 *                                                                    *
33 *           Ij = (generalized) particle code                         *
34 *     Xa,Ya,Za = position                                            *
35 *         Mreg = region number                                       *
36 *         Rull = amount to be deposited                              *
37 *          Llo = particle generation                                 *
38 *        Icall = call id                                             *
39 *                                                                    *
40 *     Output variables:                                              *
41 *                                                                    *
42 *       Comscw = factor the scored amount will be multiplied by      *
43 *       Lsczer = logical flag, if true no amount will be scored      *
44 *                regardless of Comscw                                *
45 *                                                                    *
46 *     Useful variables (common SCOHLP):                              *
47 *                                                                    *
48 *     Energy/Star binnings/scorings (Comscw):                        *
49 *          ISCRNG = 1 --> Energy    density  binning                 *
50 *          ISCRNG = 2 --> Star      density  binning                 *
51 *          ISCRNG = 3 --> Residual nuclei scoring                    *
```

```
52 *          ISCRNG = 4 --> Momentum transfer density binning            *
53 *          ISCRNG = 5 --> Activity   density binning                   *
54 *          ISCRNG = 6 --> Net charge density binning                   *
55 *          JSCRNG = # of the binning                                   *
56 *                                                                      *
57 *     Useful variables (common SOUEVT):                                *
58 *                                                                      *
59 *          X,Y,Zsoevt(i) = position    of the i_th source particle     *
60 *          TX,Y,Zsoev(i) = direction   of the i_th source particle     *
61 *              Wtsoev(i) = weight      of the i_th source particle     *
62 *              Pmsoev(i) = momentum    of the i_th source particle     *
63 *              Tksoev(i) = kin. energy of the i_th source particle     *
64 *              Agsoev(i) = age         of the i_th source particle     *
65 *              Aksoev(i) = Kaon ampl.  of the i_th source particle     *
66 *              Ussoev(i) = user var.   of the i_th source particle     *
67 *              Ijsoev(i) = identity    of the i_th source particle     *
68 *              Nrsoev(i) = region      of the i_th source particle     *
69 *              Nlsoev(i) = lattice     of the i_th source particle     *
70 *                Npsoev  = number of the source particles              *
71 *                                                                      *
72 *                                                                      *
73 *----------------------------------------------------------------------*
74 *
75 INCLUDE '(FLKMAT)'
76 INCLUDE '(SCOHLP)'
77 INCLUDE '(SOUEVT)'
78 INCLUDE '(TRACKR)'
79 INCLUDE '(FHEAVY)'
80 *
81 LSCZER = .FALSE.
82 COMSCW = ONEONE
83 * ======== In order to compute doses ========= *
84 *     (Medflk(n,iprodc) is the material number of region n
85 *      Rho(m) is the density of material m)
86 *    energy is multiplied by a 1000 to convert it from GeV to MeV
87 IF ( JTRACK .EQ. 1 ) THEN
```

```
88 COMSCW = 0.490+0.51/(1+EXP(-3.3*(LOG((ETRACK-0.93827)*1000)-0.23)))
89 END IF
90 RETURN
91 *=== End of function Comscw ===========================================*
92 END
```

Listing D.2: FLUKA input file for 1522-505 foam sample.

```
1  TITLE
2  505-scaled-444
3  * Set the defaults for precision simulations
4  DEFAULTS                                                              ...
       HADROTHE
5  * Define the beam characteristics
6  BEAM          -0.036  -0.00667                  1.        1.          ...
       PROTON
7  * Define the beam position
8  BEAMPOS           1.       0.0       0.0
9  GEOBEGIN                                                              ...
       COMBNAME
10 VOXELS           0.0      -0.5       0.0                              v526
11 0    0
12 * Black body
13 SPH blkbody    0.0 0.0 0.0 1000000.
14 * Void sphere
15 SPH void       0.0 0.0 0.0 100000.
16 RPP PET1       -1. 1. -1. 1. 4.43982 6.43982
17 RPP FILMTOP    1. 1.013 -1. 1. 4.43982 6.43982
18 RPP ACTLAYER   1.013 1.0157 -1. 1. 4.43982 6.43982
19 RPP FILM       1.013 1.0287 -1. 1. 4.43982 6.43982
20 RPP PET2       1.0287 3.0287 -1. 1. 4.43982 6.43982
21 END
22 * Black hole
23 BLKBODY      5 +blkbody -void
24 * Void around
```

```
VOID          5 +void-PET1-FILMTOP-ACTLAYER-FILM-PET2-VOXEL
* Target
pet1          5 +PET1-FILMTOP-ACTLAYER-FILM-PET2
filmtop       5 +FILMTOP-ACTLAYER-FILM-PET2
actlayer      5 +ACTLAYER-FILM-PET2
film          5 +FILM -PET2
pet2          5 +PET2
END
GEOEND
* Polyethylene terephtalate mylar C10_H8_O4)n
*
MATERIAL                              1.4                                MYLAR
COMPOUND   -0.041959  HYDROGEN -0.625017    CARBON -0.333025    OXYGENMYLAR
* Kapton polyimide film (C22_H10_N2_O5)n
*
MATERIAL                             1.42                                ...
    KAPTON
COMPOUND   -0.026362  HYDROGEN -0.691133    CARBON  -0.07327  ...
    NITROGENKAPTON
COMPOUND   -0.209235    OXYGEN                                            ...
    KAPTON
* ..+....1....+....2....+....3....+....4....+....5....+....6....+....7..
ASSIGNMA    BLCKHOLE   BLKBODY
ASSIGNMA      VACUUM      VOID
ASSIGNMA       MYLAR      pet1
ASSIGNMA      KAPTON   filmtop
ASSIGNMA      KAPTON  actlayer
ASSIGNMA      KAPTON      film
ASSIGNMA       MYLAR      pet2
USERWEIG                                                              1.
USRBIN           10.    ENERGY      -21.    1.0287        1.   6.43982
USRBIN            1.       -1.   4.43982        1.      200.      200. &
* Set the random number seed
RANDOMIZ          1.
* Set the number of primary histories to be simulated in the run
START       2000000.
```

```
58 STOP
```

,

Listing D.3: FLUKA input file for 1522-526 foam sample.

```
1  TITLE
2  1522-526-scaled
3  * Set the defaults for precision simulations
4  DEFAULTS                                                              ...
       HADROTHE
5  * Define the beam characteristics
6  BEAM          -0.036  -0.00667                  1.        1.           ...
       PROTON
7  * Define the beam position
8  BEAMPOS           1.       0.0       0.0
9  GEOBEGIN                                                              ...
       COMBNAME
10 VOXELS           0.0      -0.5       0.0                              v526
11 0    0
12 * Black body
13 SPH blkbody    0.0 0.0 0.0 1000000.
14 * Void sphere
15 SPH void       0.0 0.0 0.0 100000.
16 RPP PET1       -1. 1. -1. 1. 1.24992 3.24992
17 RPP FILMTOP    1. 1.013 -1. 1. 1.24992 3.24992
18 RPP ACTLAYER   1.013 1.0157 -1. 1. 1.24992 3.24992
19 RPP FILM       1.013 1.0287 -1. 1. 1.24992 3.24992
20 RPP PET2       1.0287 3.0287 -1. 1. 1.24992 3.24992
21 END
22 * Black hole
23 BLKBODY      5 +blkbody -void
24 * Void around
25 VOID         5 +void-PET1-FILMTOP-ACTLAYER-FILM-PET2-VOXEL
26 * Target
27 pet1         5 +PET1-FILMTOP-ACTLAYER-FILM-PET2
```

```
filmtop      5 +FILMTOP-ACTLAYER-FILM-PET2
actlayer     5 +ACTLAYER-FILM-PET2
film         5 +FILM -PET2
pet2         5 +PET2
END
GEOEND
* Polyethylene terephtalate mylar C10_H8_O4)n
*
MATERIAL                              1.4                                MYLAR
COMPOUND   -0.041959  HYDROGEN -0.625017    CARBON -0.333025    OXYGENMYLAR
* Kapton polyimide film (C22_H10_N2_O5)n
*
MATERIAL                             1.42                                ...
    KAPTON
COMPOUND   -0.026362  HYDROGEN -0.691133    CARBON  -0.07327  ...
    NITROGENKAPTON
COMPOUND   -0.209235    OXYGEN                                           ...
    KAPTON
* ..+....1....+....2....+....3....+....4....+....5....+....6....+....7..
ASSIGNMA    BLCKHOLE   BLKBODY
ASSIGNMA      VACUUM      VOID
ASSIGNMA       MYLAR      pet1
ASSIGNMA      KAPTON   filmtop
ASSIGNMA      KAPTON  actlayer
ASSIGNMA      KAPTON      film
ASSIGNMA       MYLAR      pet2
USERWEIG                                                              1.
USRBIN           10.    ENERGY      -21.    1.0287        1.   3.24992
USRBIN            1.       -1.   1.24992        1.      200.      200. &
* Set the random number seed
RANDOMIZ          1.
* Set the number of primary histories to be simulated in the run
START       2000000.
STOP
```

Appendix E

MATLAB codes and figures for chapter 4

Listing E.1: MATLAB code for determining the locations of the Bragg peak

```
\begin{figure}[ht!]
\begin{center}
\fbox{\includegraphics[width = 15cm,height ...
    =15cm,keepaspectratio]{Richardcode.png}}
\caption{MATLAB code for determining the locations of the Bragg peak, ...
    zero point and the d20
based on a fitted polynomial.}
\label{fig:Rcode}
\end{center}
\end{figure}
\begin{figure}[ht!]
\begin{center}
\fbox{\includegraphics[width = 15cm,height ...
    =15cm,keepaspectratio]{std-nathan.png}}
\caption{MATLAB code for determining the mean and standard deviation.}
\label{fig:STD}
\end{center}
\end{figure}
```

Listing E.2: MATLAB script used to obtain the calibration curve of EBT3 intensities vs absorbed dose measured with Markus Chamber.

```
CC = imread('calibration-Dec18013.tif');
CC2 = CC(125:770,123:5174,:);
figure; imshow(CC2,[])
CCr = reshape(mean(CC2(340:349,:,:),1),5052,3);%gives image of the part ...
    of the film we are interested in
figure;imshow(CCr,[])
%figure; plot (CFr)% will plot all three channels
%figure; plot (-CFr) %-ve sign here is used to bring the peaks on the top
figure; plot(sum(-CCr,2)) % sum up dose in all three channels
% d are the dose values at entrance calculted from tony's data for ...
    refernce check the spread sheet multiplied by 100 to convert dose in ...
    gy to dose in cgy
D = [3.94637164230841 3.20846537448008 2.644232073555 1.94464800969123 ...
    1.28420151583383 0.741983098037325 0]*100;
F=[7.085e4 7.459e4 7.857e4 8.451e4 9.183e4 1.01e5 1.125e5]; % f are the ...
    dose values (y) at the entrance point of the calibrated film taken ...
    from the figure; plot(sum(-CFr,2))
figure; plot(F,D','o')              %f is the sum of intensity from all ...
    three channels
fpf = polyfit(F,D,3);
hold on
plot(70000:120000,fpf(1)*(70000:120000).^3+fpf(2)*(70000:120000)
.^2+fpf(3)*(70000:120000)+fpf(4))
title('c curve3rd order')
xlabel('Intensity (sum of RGB)')
ylabel('Delivered dose (cGy)')
title('Calibration Curve for 36 MeV Proton Beam')
```

Listing E.3: MATLAB code for irrdiated film's analysis.

```
X = imread('calibration-Dec18_014.tif'); % image that contains all ...
    exposed films
figure; imshow(X,[])
```

```
XX19 = sum(X(1397:2057,5622:6422,:),3); %film19 %each film is Excised ...
    from the main TIFF image
figure; imshow(XX19,[])
XX20 = sum(X(1405:2061,4798:5530,:),3); % film20
figure; imshow(XX20,[])
XX21 = sum(X(1401:2077,4046:4710,:),3); % film21
figure; imshow(XX21,[])
X21 = imrotate(XX21, -3);
figure; imshow(X21,[])
f=[7.085e4 7.459e4 7.857e4 8.451e4 9.183e4 1.036e5 1.125e5]; %values ...
    for film intensity obtained from calibration films
d=[3.94637164230841 3.20846537448008 2.644232073555 1.94464800969123 ...
    1.28420151583383 0.741983098037325 0]*100; %dose from Markus chamber cGy
fpf = polyfit(f,d,3);
C19r = XX19(178:491,143:448);
figure; imshow(C19r,[])
C19 = C19r(1:314,9:306);
figure; imshow(C19,[])
C19n = C19.^3*fpf(1)+C19.^2*fpf(2)+C19*fpf(3)+fpf(4);
figure; imshow(C19n,[])
PB19 = C19n';
figure; imagesc(PB19)
pf19 = zeros(length(PB19),2);
[m,i] = max(PB19);
[mz,iz] = min(max(PB19-m*0.1,0));
for K = 1:length(PB19)
pf19(K,:) = polyfit(1:(iz(K)-i(K)+1-5),PB19((i(K)+5):iz(K),K)',1);
end
hold on
plot(i,'r')
%plot(iz,'g')
plot((i'-m'./pf19(:,1)*0.8),'b')
plot((i'-m'./pf19(:,1)*0.2),'m')
title('Foam sample 1522-507(film19)')
xlabel('Y bin numbers (1bin = 0.0353mm)')
ylabel('Z bin numbers (1bin = 0.0353mm)')
```

```
36 legend('Bragg Peak','d20','d80', 'Location','Northwest')
37 d20 = (i'-m'./pf19(:,1)*0.8);
38 d80 = (i'-m'./pf19(:,1)*0.2);
39 d80_20=d20-d80;
40 d20t=[];
41 d20t=[d20t; d20(34:272)];
42 mean([d20t; d20(34:272)])
43 std([d20t; d20(34:272)])
44 mean([d80_20(34:272)])
45 std([d80_20(34:272)])
```

Listing E.4: MATLAB 'dir' function and temporary variables to determine the image dimensions.

```
1 imagelist = dir('*.dcm');
2 tagimage = dicomread(imagelist(1).name);
3 imginfo = dicominfo(imagelist(1).name);
```

Listing E.5: MATLAB code for structure creation.

```
246 % cropping values
247 % # of pixels = ceil(20/0.0434) 461 pixels = 20.074mm, 2.0074cm
248 % dimensions = [1267,1376]
249 lx = ceil(1376/2)-ceil(461/2)+1;
250 ux = ceil(1376/2)+ceil(461/2);
251 ly = ceil(1267/2)-ceil(461/2)+1;
252 uy = ceil(1267/2)+ceil(461/2);
```

Listing E.6: MATLAB code for substituting working DICOM information to the images.

```
1 % for substituting working DICOM information and writing new DICOM images
2 imagelist = dir('1522-507*.dcm');
3 [slices,nn] = size(imagelist);
4 for i = 1:slices
5 Jimages = dicomread(imagelist(i).name);
```

```
Jinfo = dicominfo(imagelist(i).name);
copyinf = dicominfo('c1_0001.dcm');
copyinf.BitDepth = Jinfo.BitDepth;
copyinf.FileMetaInformationGroupLength = ...
    Jinfo.FileMetaInformationGroupLength;
copyinf.MediaStorageSOPClassUID = Jinfo.MediaStorageSOPClassUID;
copyinf.MediaStorageSOPInstanceUID = Jinfo.MediaStorageSOPInstanceUID;
copyinf.SpacingBetweenSlices = 0.0434;
copyinf.SliceThickness = 0.0434;
copyinf.SeriesNumber = i+1;
copyinf.AcquisitionNumber = i+1;
copyinf.SliceLocation = 0.0434*i+1;
copyinf.ImagePositionPatient(3) = copyinf.SliceLocation;
copyinf.PixelSpacing = [0.0434;0.0434];
copyinf.RescaleSlope = 1;
new_img = Jimages(ly:uy,lx:ux);
dicomwrite(new_img,(sprintf('507-cropped%04i.dcm',i)),copyinf,'CreateMode
','Copy');
end
```

Listing E.7: MATLAB code for scaling and assigning the image density equivalent to the real foam density and checking the overall image density.

```
%to check the over all image density
%for 507 images overall density would be 0.12g/cm3
image_list=dir('507-cropped*.dcm');
[no_slice,nn]=size(image_list);
for i=1:no_slice
image_dcm=dicomread(image_list(i).name);
hdr_dcm = dicominfo(image_list(i).name);
image_dcmm = double(image_dcm);
img_hu = (image_dcmm+11)/(256+11)*1024;
img_hu = img_hu.*(img_hu>0);
dicomwrite(uint16(img_hu), (sprintf('507-scaled%04i.dcm',i)), ...
    hdr_dcm,'CreateMode','Copy')
```

```
N = 921;
img_dir = dir('507-scaled*.dcm');
img = dicomread(img_dir(1).name);
siz_img = size(img);
ct3d = NaN([siz_img N]);
ct3d(:,:,1) = img;
for ii=2:N
ct3d(:,:,ii)= dicomread(img_dir(ii).name);
end
img_hutest = mean(ct3d,3);
mean(reshape(img_hutest,1,213444))/1024
```

Listing E.8: Method used for calculating the full width half maximum.

```
% by using the relationship between energy and momentum, E^2 - m^2 = P^2
% A 26 MeV beam will have a momentum of
sqrt((0.036+0.938)^2-0.938^2) = 0.2624 GeV/c
% with 0.5% more energy
sqrt((0.03618+0.938)^2-0.938^2) = 0.2630 GeV/c
% so, the momentum difference is = 0.00067 GeV/c
```

Appendix F

Matlab codes for chapter 5

Listing F.1: MATLAB code for plotting the 3D dose distributions from FLUKA output.

```
numfiles =19;
valsw = cell(1,numfiles);
A = dicomread('RN.1.2.246.352.71.5.507863515322.12449.20180417151511.dcm');
RI=dicominfo('RN.1.2.246.352.71.5.507863515322.12449.20180417151511.dcm');
for K = 1:19
myfilename = sprintf('file%03d.asc', 20-K);
valsw{K} = load(myfilename);
end
RSPw=zeros(size(reshape(valsw{1,2}',2022480,1)));
for i=1:1:19
AA= reshape(valsw{1,i}',2022480,1);
RSPw = RSPw+ ...
    RI.IonBeamSequence.Item_1.IonControlPointSequence.(['Item_' num2str( ...
    i *2-1)]).ScanSpotMetersetWeights(mean(2:356)).*AA;
end
S3Dw = reshape(RSPw,159,159,1,80);
figure; imshow(reshape(S3Dw(:,:,1,40),159,159),[])
figure;plot((0:158)*0.25,S3Dw(:,80,1,40))
S = ((0:158)*0.25);
T = S3Dw(:,80,1,40); Tnorm = T /max(T(10,1));% here 10 is the point ...
    where  to normalize the dose choosed this point from Sobp graph by ...
```

```
      using the index pointer
figure;plot(S,Tnorm)
```

Appendix G

Presentations

During these studies frame, I have also guided and provided support to two MSc students in the completion of their research projects. The first thesis is entitled **"Modelling the range uncertainty of protons in lung tissue with FLUKA " by Charles Nathan Kimball-Smith (January 2018)**. He successfully run FLUKA Monte Carlo simulations to replicate the experiment performed at Birmingham University (proton beam line) for finding changes in spread of the Bragg peak as a function of foam density. The second thesis is entitled **" The use of fine-structure spectroscopy techniques in determining proton range uncertainties" by Owen Thomas Williams (December 2018)**. The main focus of Owen's project was on determination of shifts in Bragg peak width and position for a range of pore sizes, bone lengths and densities. I have presented my work at various conferences and meetings such as **Proton Physics Research and Implementation Group (PPRIG) workshop 2016 (London) Monte Carlo User Group Meeting (MCNEG) 2016, (Manchester) and Medical Physics and Engineering Conference (MPEC) 2018,(Yorkshire)**.